DISSERTATION

Titel der Dissertation

Reconstruction Methods for

Quantitative Coupled Physics Imaging

Verfasser

Mag. Wolf Naetar

angestrebter akademischer Grad

Doktor der Naturwissenschaften (Dr. rer. nat.)

Wien, Oktober 2015

Studienkennzahl lt. Studienblatt :	A 796 605 405
Dissertationsgebiet lt. Studienblatt :	Mathematik, IK: Computational Sciences
Betreut von / Supervisor:	Univ.-Prof. Dr. Otmar Scherzer

Abstract

The unifying property of *coupled physics imaging methods* is that they use a *combination of different physical modalities* (e.g., electromagnetic waves, ultrasound, electric current) to obtain tomographic data.

The goal of *quantitative* coupled physics imaging is to utilize these methods to image (spatially varying) physical properties of the sample (such as *electrical conductivity* or *optical absorption* and *scattering coefficients*), which can serve as valuable diagnostic information. Generally, one has to solve a *two-step inverse problem* to obtain such images. First, internal data (such as *current density*, *power density* or *initial pressure maps*) are calculated from the measurements. Then the actual material properties are recovered from the internal data.

This cumulative dissertation contains three research articles on specific problems in quantitative coupled physics imaging, all of them pertaining to the second step of the two-step inverse problem.

The first two articles focus on *quantitative photoacoustic tomography*, an imaging method that uses laser excitations to generate ultrasound waves (which can be measured) and seeks to image optical properties of the sample. In the first article, we propose a restriction to piecewise constant parameters in order to solve an otherwise ill-posed problem, the determination of *absorption, diffusion* and *Grüneisen coefficients* from multiple photoacoustic measurements (corresponding to different illumination patterns). The reconstruction is based on an analytical procedure, which we tested on simulated data.

In the second article, again assuming that the coefficients are piecewise constant, we show that if the Grüneisen coefficient is known, absorption and diffusion coefficients can be recovered from a *single* photoacoustic measurement. We also present a variational method (based on the *Ambrosio-Tortorelli approximation* of a *Mumford-Shah-like* functional) to recover these parameters.

In the third article we consider another quantitative coupled physics imaging problem, the reconstruction of *electric conductivity* from *power density measurements*, an important problem in *Acousto-Electrical* and *Impedance-Acoustic* tomography. We propose an iterative regularization approach, analyse its convergence and test the method on simulated data.

Preface

This cumulative dissertation is a collection of scientific articles the author worked on during the last three years.

The first part serves as an introduction to the topic of quantitative coupled physics imaging, with a focus on methods coupling electromagnetic excitations with ultrasound measurements. In every Section, a coupled physics imaging method is introduced and its mathematical model derived. Furthermore, a significant part of the knowledge that has been accumulated so far within the respective field is summarized.

The introduction is followed by three Chapters, each containing an article that has been published (or accepted for publication) in an academic journal. Therefore, a reader familiar with the topic may also read each Chapter of the second part independently.

The document ends with an Appendix containing references and a German translation of the abstract.

At this point, I express my gratitude to my supervisor Otmar Scherzer for supporting me with his expertise and valuable suggestions.

Furthermore, I would like to thank my colleagues at the Computational Science Center Vienna for their friendship, support and help. I really had a great time working here and will miss our espresso sessions.

In addition to Otmar, I collaborated with several fantastic mathematicians during the last three years. My thanks go out to Guillaume Bal, Elena Beretta, Monika Muszkieta and John Schotland.

I also would like to thank the University of Vienna and the FWF for their prolonged financial support.

More love goes out to my family and friends for their care and support. Finally, thank you, Milena for being amazing and sharing your life with me.

Wolf Naetar
University of Vienna
October 5, 2015

Contents

1. Introduction

1.1. Quantitative Coupled Physics Imaging

The goal of *tomography* is to image the internal structure of an object from outside measurements. Historically, this happened in the form of two-dimensional images, which is where the word "tomography" originated from (the greek word "tomos" means "slice"). Modern tomographic techniques, however, are often able to generate 3-dimensional (volumetric) data. Well-known commercial examples of tomography include *X-Ray Tomography*, *Magnetic Resonance Imaging* and *Positron Emission Tomography*. Tomographic techniques are used to image animals and humans (e.g., in *medical imaging*) as well as inanimate objects (e.g., in *non-destructive testing* or *geophysical prospecting*).

Coupled physics imaging (also called *hybrid imaging*) is a novel field of research in the area of tomography that aims to combine two or more physical modalities (e.g., electromagnetic waves, ultrasound, electric current) to obtain images which cannot be generated using a single modality alone [14, 114, 120].

The imaging community commonly distinguishes between *qualitative* and *quantitative* imaging methods [46, 47]. In qualitative imaging, one is content with images that resemble the structure of the underlying object, i.e., changes of tissue type (in medical imaging) or impurities (in non-destructive testing) are visible in the image (as edges).

In quantitative imaging, in contrast, the image data maps a local physical property of the material like *electric conductivity*, *permittivity*, *optical absorption* or *mechanical rigidity*. This information can be used to identify the nature of the defect or inhomogeneity, which is of particular interest in medical imaging, where contrast in certain physical quantities can be used to obtain diagnostically valuable information such as tissue type, blood oxygenation levels or marker concentration [35, 46, 47, 53, 60] or be linked to pathologies [64, 78, 74, 111].

In many cases (in particular, all the coupled physics imaging methods listed in this work), to obtain quantitative image data, one has to solve a *two-step inverse problem*

$$\text{Measurements} \longrightarrow \text{Internal data} \longrightarrow \text{Parameter of interest.}$$

The internal data obtained from the measurements (which are made *outside* the object) in the first step gives a *qualitative* image of the object (i.e., the geometric structure of the material is already discernible), but it may contain non-local effects (e.g., shadows) or depend on parameters of the tomographic set-up (see, e.g., [47, 89]). In the second step, actual material properties are recovered from the internal data.

In the rest of this Chapter, we discuss three examples of (quantitative) coupled physics imaging methods, concentrating on methods that couple electromagnetic excitations (in various frequency regimes) with ultrasound measurements. We look at their mathematical models, properties as inverse problems and numerical approaches for their solution that can be found in the literature.

1.2. Photoacoustic Tomography

Photoacoustic Tomography (PAT), also called *Photoacoustic Imaging* (PAI), combines electromagnetic excitation (in the visible spectrum) with ultrasound measurements. The coupling is given by the *photoacoustic effect*. First, a laser pulse (with wavelength λ) is delivered into a translucent body Ω. The absorbed optical energy leads to thermal expansion, which in turn generates an ultrasound pressure wave $p(x,t)$ (where $x \in \mathbb{R}^3$ is the space and $t \in \mathbb{R}$ is the time variable) that can be measured outside the sample.

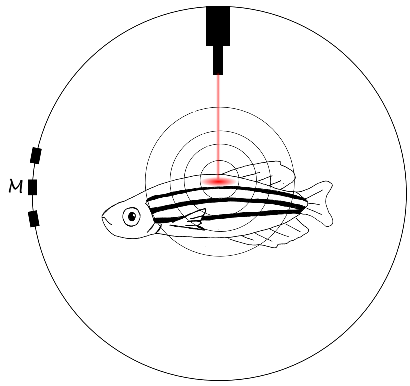

Figure 1.1.: Schematic representation of a Photoacoustic Tomography setup. A sample is illuminated by a laser pulse, which generates a pressure wave that can be detected outside the fish using ultrasound transducers.

By solving an *inverse problem for the wave equation*, these ultrasound measurements can be used to calculate the *initial pressure* $\mathcal{H}(x)$ which generated the wave p. Since $\mathcal{H}(x)$ is proportional to the absorbed electromagnetic energy $\mathcal{E}(x)$, the calculated initial pressure data visualizes inhomogeneities in the object of interest (with the contrast generated by differences in the *optical absorption coefficient* $\mu_a(x,\lambda)$ at the *laser wavelength* λ). That is, slices of $\mathcal{H}$ are *qualitative* tomographic images.

To obtain *quantitative* images an additional *inverse problem for light transport* has to be solved. Here, the initial pressure data $\mathcal{H}$ (the *internal data*) is utilized to calculate *optical material coefficients* (that is, absorption and scattering coefficients $\mu_a(x,\lambda), \mu_s(x,\lambda)$) of the object, which can in turn be linked to diagnostically relevant information (e.g., blood oxygenation level or chromophore concentration, see [46, 47]). This is the goal of *quantitative Photoacoustic Tomography* (qPAT).

1.2.1. The acoustic problem

Mathematically, the problem can be modelled as follows. By linearizing the *Euler and continuity equations of fluid dynamics* around an equilibrium state and using the *linearized expansion equation* (which can be derived from thermodynamic principles), one can show (see, e.g., [47, 66, 105]) that the pressure p satisfies the wave equation

$$\frac{1}{c^2(x)}\partial_{tt}p(x,t) - \Delta p(x,t) = \frac{\beta(x)}{C_p(x)}\partial_t H(x,t), \tag{1.2.1}$$

where $c(x)$ is the speed of sound, $H(x,t)$ the rate of heat supplied by absorption, $C_p(x)$ the specific heat capacity and $\beta(x)$ the volume thermal expansion coefficient. Note that in order to obtain this equation, thermal diffusion, viscosity and other forms of acoustic attenuation have to be disregarded. Further assuming instantaneous deposition of the laser energy (which approximately holds since the light passes through the medium much faster than the generated wave packets move), that is, taking $H(x,t) = \mathcal{E}(x)\delta(t)$, one can rewrite (1.2.1) as the initial value problem [47, 66, 105]

$$\begin{aligned} \partial_{tt}p(x,t) - c^2(x)\Delta p(x,t) &= 0 \\ \partial_t p(x,0) &= 0 \\ p(x,0) &= \frac{\beta(x)c^2}{C_p(x)}\,\mathcal{E}(x) = \mathcal{H}(x). \end{aligned} \tag{1.2.2}$$

The dimensionless quantity $\Gamma(x) = \frac{\beta(x)c(x)^2}{C_p(x)}$ is called the *Grüneisen coefficient* or *photoacoustic efficiency*, it corresponds to the fraction of absorbed electromagnetic energy converted into acoustic signal, i.e., we have $\mathcal{H}(x) = \Gamma(x)\,\mathcal{E}(x)$.

In these terms, the inverse problem of interest in Photoacoustic Imaging is the determination of $\mathcal{H}(x)$ from the knowledge of $p(x,t)$, $x \in \mathcal{M}, t > 0$, where $\mathcal{M}$ denotes a measurement surface (in practice, p can only be measured on discrete points, however, for mathematical analysis it is commonly assumed that p is known everywhere on $\mathcal{M}$). That is, we want to invert the mapping

$$\mathcal{H} \mapsto p|_{\mathcal{M}} =: g(\mathcal{H}) \tag{1.2.3}$$

defined by (1.2.2). This inverse problem has received a lot of interest by the mathematical community and a host of results have been accumulated. An overview can be found in [83].

In particular, it has been shown that if c is a smooth function and $\mathcal{M}$ a closed surface fully surrounding the sample (i.e., there are no ultrasound sources outside the measurement surface), $\mathcal{H}$ can be uniquely reconstructed from the measurement data. If the second assumption is violated, unique reconstruction is still possible if the speed of sound c satisfies a *non-trapping condition* [2].

The two most commonly used reconstruction methods are *analytic inversion* methods and *time reversal*. Analytical methods rely on a specific *acquisition geometry*, i.e., a certain shape of $\mathcal{M}$, and in general only work in the constant sound speed case. By the observation that, using the Poisson-Kirchhoff formula, the solution p of (1.2.2) with $c \equiv 1$ can explicitly be written as

$$\begin{aligned} p(x,t) &= \frac{\partial}{\partial t} t(R\mathcal{H})(x,t) \\ (R\mathcal{H})(x,r) &= \frac{1}{4\pi} \int_{|\zeta|=1} \mathcal{H}(x + r\zeta)\, dS(\zeta), \end{aligned}$$

it suffices to invert the *spherical mean operator* R from boundary measurements. This problem has been investigated for a multitude of detector geometries, including spherical, cylindrical and planar detectors [83]. A popular class of methods are those based on *filtered backprojection*, e.g., [58, 59, 87, 121], a principle that is also used for the inversion of the *Radon transform*.

A different approach is based on the assumption that for large enough $T > 0$, all wave packets have left the volume Ω enclosed by the (closed) measurement surface and one can thus assume $p(x,T) = 0$, reverse time and solve the initial-boundary value problem

$$\begin{aligned} \partial_{tt} p(x,t) - c^2(x)\Delta p(x,t) &= 0 \quad \text{for all } x \in \Omega, t > 0 \\ \partial_t p(x,T) &= 0 \quad \text{for all } x \in \Omega \\ p(x,T) &= 0 \quad \text{for all } x \in \Omega \\ p(x,t) &= g(x,t) \quad \text{for all } x \in \partial\Omega, t > 0. \end{aligned}$$

The initial pressure is then given by $\mathcal{H}(x) = p(x,0)$. This approach (commonly referred to as *time reversal* or *back propagation*) is valid if the speed sound speed c (which has to be known) is non-trapping and T is large enough. In particular, it shows that the inverse problem is stable.

1.2.2. The optical problem (using the radiative transfer equation)

In the quantitative part of the problem, the goal is to calculate maps of the optical material properties (in particular *absorption and scattering coefficients* μ_a, μ_s) of the object of interest Ω from the reconstructed internal data $\mathcal{H}$. First, we need a model for light transfer.

Since the dominant mode of light-matter interaction in biological tissue is *scattering* from objects roughly as large as the optical wavelength λ [116] (and thus much smaller than the possible image resolution), it is customary in biomedical optics to assume that the object of interest behaves like a *random medium* [116, 119], i.e., scattering and absorption events occur randomly.

The *radiative transfer equation* (RTE)

$$\begin{aligned}\left(\frac{1}{c}\partial_t + v\cdot\nabla + (\mu_a(x)+\mu_s(x))\right)\psi(x,v,t)\\ - \mu_s\int\limits_{S^{n-1}} P(v',v)\psi(x,v',t)dS(v') = S(x,v,t),\end{aligned} \tag{1.2.4}$$

which can be derived (phenomenologically) from conservation of energy, can be used to describe light transfer in such a medium. Here, $\psi(x,v,t)$ denotes *radiance* (the measure of light flow at a point x and time t in the direction r), c the medium's speed of light, $\mu_a(x)$ and $\mu_s(x)$ the *absorption and scattering coefficients* (the probability that a photon is scattered or absorbed when travelling a unit length), $P(v',v)$ the *scattering phase function* (the probability density of a light ray with propagation direction v' being scattered in direction v) and $S(x)$ a source term which describes the incident light. Note that all quantities in (1.2.4) also depend on the light wavelength λ.

For the purpose of quantitative Photoacoustic Imaging (since the energy deposition happens almost instantaneously compared to the acoustic wave travel time) one can integrate all quantities over time and reduce (1.2.4) to the steady-state form

$$(v\cdot\nabla + (\mu_a(x)+\mu_s(x)))\,\psi(x,v) - \mu_s\int\limits_{S^{n-1}} P(v',v)\psi(x,v')\,dS(v') = S(x,v). \tag{1.2.5}$$

If we further denote by

$$u(x) = \int_{S^{n-1}} \psi(x,v)dS(v) \tag{1.2.6}$$

the *fluence* (the total light energy received in x), the absorbed optical energy is given by $\mathcal{E}(x) = \mu_a(x)u(x)$. The initial pressure $\mathcal{H}$ reconstructed in the first step (the acoustic problem) is proportional to the absorbed energy by (where Γ is the Grüneisen coefficient introduced earlier, which also tends to be inhomogeneous in biological tissue)

$$\mathcal{H}(x) = \Gamma(x)\,\mathcal{E}(x) = \Gamma(x)\mu_a(x)u(x).$$

In this setting, the inverse problem of quantitative Photoacoustic Tomography [44, 46, 47, 106] is the inversion of the mapping

$$(\mu_a,\mu_s,\Gamma) \mapsto \Gamma\mu_a u =: \mathcal{H}(\mu_a,\mu_s,\Gamma) \tag{1.2.7}$$

where u satisfies (1.2.5),(1.2.6), given one or multiple measurements of $\mathcal{H}$ (with different sources and/or wavelengths) and possibly (partial) knowledge of some of the unknown parameters μ_a, μ_s, Γ and the boundary values of the radiance $\psi|_{\partial\Omega}$. Note that the scattering phase function P is usually assumed to be given, e.g., by the *Henyey-Greenstein phase function* [104, 115].

Due to the mathematical complexity of the radiative transfer model, this problem has not yet been analyzed in-depth and most results on this problem are of numerical nature (based on, possibly regularized, Gauss-Newton or Newton schemes, see, for instance [98, 104, 115, 123]).

Analytical properties of the forward operator (necessary for the use of Tikhonov regularization) were analysed in [50]. They also suggested a level set approach to recover piecewise constant μ_a, μ_s. In a slightly modified setting (where the source term S in (1.2.5) is described by a known boundary condition ψ), Bal et al. [23] showed that if Γ is known, (μ_a, μ_s) can be uniquely reconstructed (in a stable manner) from knowledge of the *full albedo operator* (that is, the operator $\psi \mapsto \mathcal{H}(\psi)$, which maps source to measurement). Mamonov and Ren [92] analyzed the problem for non-scattering media (with $\mu_s = 0$) and showed that in this case, (μ_a, Γ) can be reconstructed from measurements of $\mathcal{H}$ with two illuminations (sources) uniquely and stably. They also showed that all three unknowns (Γ, μ_a, μ_s) can be reconstructed uniquely from the albedo operator at multiple wavelengths (assuming a particular wavelength dependence of the optical coefficients).

1.2.3. The optical problem (using the diffusion approximation)

For highly scattering media with $\mu_s \gg \mu_a$ the fluence u is well-approximated by the *diffusion approximation* (DA)

$$\frac{1}{c}\partial_t u(x,t) - \nabla \cdot (D(x)\nabla u(x,t)) + \mu_a(x)u(x,t) = S(x,t) \tag{1.2.8}$$

of the radiative transfer equation [15, 116, 119]. Here, S describes the light source and

$$D(x) = \frac{1}{3(\mu_a + (1-g)\mu_s)}, \quad g = \int_{S^{n-1}} (v' \cdot v)\, P(v', v) dS(v')$$

D is called the *diffusion coefficient* (which, like μ_a and μ_s, depends on the utilized wavelength λ), g the *scattering anisotropy* (the expected scattering angle).

This approximation is based on the assumption that after a sufficient number of scattering events, the radiance becomes sufficiently isotropic that it depends linearly on the direction v,

$$\psi(x,v,t) = \frac{1}{4\pi}u(x,t) + \frac{3}{4\pi}J(x,t) \cdot v, \tag{1.2.9}$$

where $J(x,t) = \int_{S^{n-1}} v\psi(x,v,t)\, dS(v)$ is the *current density* (net energy flow) [15, 116]. The diffusion approximation can also be derived by a first-order expansion of the radiance ψ into spherical harmonics, it is therefore also referred to as the P_1-approximation (similarly, the P_N approximation expands the radiance into spherical harmonics of N-th order). Note that the approximation does not depend on the specific choice of scattering phase function P.

The isotropy assumption (1.2.9) is only valid after the incident light ray has passed a certain minimal depth (and the photos have thus experienced enough scattering to become nearly isotropic). This area is often referred to as the *diffusive regime*, in contrast to the *ballistic regime*, where the light transfer remains strongly directional [116].

For the purpose of Photoacoustic Imaging, we can again reduce (1.2.8) to the steady-state case (by integrating over time) and remove the source S from the observed region Ω to obtain (using $\mu_a =: \mu$ for brevity)

$$-\nabla \cdot (D(x)\nabla u(x)) + \mu(x)u = 0. \tag{1.2.10}$$

In this formulation, the goal of qPAT is to invert the initial pressure map

$$(\mu, D, \Gamma) \mapsto \Gamma\mu u =: \mathcal{H}(\mu, D, \Gamma), \tag{1.2.11}$$

where u satisfies (1.2.10). Again, sometimes some of the unknown parameters μ, D, Γ or the boundary values $u|_{\partial\Omega}$ are assumed to be known and multiple measurements of $\mathcal{H}$ (with varying source position or wavelength λ) may be utilized.

It is well-known [29, 44, 94, 106] that, given a single measurement of $\mathcal{H}$ (at a single wavelength), this inverse problem has infinitely many solutions even if one of the parameters are and $u|_{\partial\Omega}$ are known. In the case where D is known, this is obvious since, for arbitrary $\mu > 0$, the pairs $\left(\tilde{\Gamma}, \tilde{\mu}\right) = \left(\frac{\mathcal{H}}{\tilde{\mu}u(\tilde{\mu})}, \tilde{\mu}\right)$ all generate the same data $\mathcal{H}$. The same reasoning applies of μ is known. If Γ is known, one can show (by inserting $\mathcal{E} = \frac{\mathcal{H}}{\Gamma} = \mu u$ into (1.2.10), see [94]) that for infinitely many $\tilde{D} > 0$, the pair $(\tilde{\mu}, \tilde{D}) = \left(\mathcal{H}/\Gamma\tilde{u}, \tilde{D}\right)$, where $\tilde{u}$ solves $\nabla \cdot (\tilde{D}\nabla\tilde{u}) = \frac{H}{\Gamma}$ generates the same data $\mathcal{H}$.

Bal and Ren showed in [29] that by varying the source (i.e., the boundary values $u|_{\partial\Omega}$), this non-uniqueness can be overcome. In particular, they showed that, for coefficients $\mu, D, \Gamma \in W^{1,\infty}(\Omega)$, and well-chosen boundary conditions f_1, f_2, the corresponding data $\mathcal{H}_1, \mathcal{H}_2$ uniquely determine the functions

$$\chi(x) = \left(\frac{\sqrt{D}}{\Gamma\mu}\right)(x), \quad q(x) = -\left(\frac{\Delta\sqrt{D}}{\sqrt{D}} + \frac{\mu}{D}\right)(x)$$

which can in turn be used to find two of the parameters μ, D, Γ if the third one (and the unknown coefficients boundary value) is given. They also showed that the functions χ, q can also be used to determine the measurement $\mathcal{H}(f)$ corresponding to an arbitrary boundary condition f, which means more than two measurements don't add any new information. Furthermore, coefficient triples (μ, D, Γ) that generate the same χ and q also generate the same data, which shows that is impossible to uniquely determine three unknown coefficients by varying the source (since there exist transformations of μ, D, Γ that leave χ and q invariant). In a similar vein, in [33], the problem was analyzed in a more general framework of coefficient identification problems for second order elliptic equations given measurements proportional to the solution.

On the other hand, in [30], Bal and Ren showed that, given some additional information about the spectral dependence of the coefficients μ, D, Γ, by measuring at two specific wavelengths λ_1, λ_2 and additionally varying the source (using the same boundary conditions as in [29]), the three unknown coefficients (at both wavelenghts) can be determined uniquely.

In [86], Kuchment and Steinhauer investigated the stability of the linearized qPAT problem (i.e., the Fréchet derivative of the operator $(\mu, D) \mapsto H(\mu, D)$, with Γ assumed to be known). By rewriting the linearized measurement operator as a pseudo-differential operator and establishing its ellipticity, they were able to show that if $2n$ (where n is the space dimension) well-chosen measurements of $\mathcal{H}$ are given, the linearized inverse problem is stably invertible modulo a possible a finite-dimensional kernel.

An overview of numerical work on diffusive qPAT can be found in the review article [46] by Cox et al. In particular, the determination of a single unknown parameter μ (with D, Γ known) was treated, for instance, in [34, 43, 45] (using simulated data). For this (simpler) problem, practical viability (for experimental data) has been established both for phantoms [124] and biological samples [109, 110].

The multi-source case, which in theory allows for the determination of two of the unknown coefficients μ, D, Γ, has been verified numerically (using simulated data) in [61, 101, 106, 115, 127] using a host of different numerical techniques. In [37] (using the DA) and [65] (using the RTE) it was suggested to solve the acoustic problem and multi-source quantitative problems in a single step. To the authors knowledge, the determination of two or more unknown inhomogeneous coefficients from experimental photoacoustic data has not yet been achieved (except for special cases, e.g., with known geometry [88]).

1.3. Thermoacoustic Tomography

Thermoacoustic Tomography (TAT) is a common variation of Photoacoustic Tomography that utilizes *microwave radiation* to excite the sample (rather than visible light). As in PAT (see Section 1.2), a short pulse of electromagnet radiation generates an ultrasound wave $p(x,t)$ (by thermo-elastic expansion) that can be measured outside the sample. The governing equations are the same as in PAT [83], that is, p satisfies

$$\begin{aligned} \partial_{tt}p(x,t) - c^2(x)\Delta p(x,t) &= 0 \\ \partial_t p(x,0) &= 0 \\ p(x,0) &= \mathcal{H}(x), \end{aligned} \tag{1.3.1}$$

where $\mathcal{H}(x)$ denotes the *initial pressure* generated by the microwave pulse and $c(x)$ denotes the medium's (possibly spatially varying) speed of sound. Consequently, the same reconstruction techniques as in PAT can be applied to obtain $\mathcal{H}$, which again serve as internal data for the *quantitative* problem.

At microwave frequencies, scattering is much less pronounced in biological tissue than for visible light. Furthermore, the relevant scattering structures are much larger (of the same order as the EM wavelength). Thus, a model for microwave transmission, which is necessary for *quantitative* Thermoacoustic Tomography, can be derived directly from *Maxwell's equations* (where scattering is described deterministically by differences in refractive index).

Following [120], we start by assuming that the medium is linear and responds instantaneously to an applied electric field with frequency ω, that is, that the equations

$$D(x,t) = \epsilon(x,\omega)E(x,t), \quad B(x,t) = \mu_0 H(x,t), \quad J(x,t) = \sigma(x,\omega)E(x,t) \tag{1.3.2}$$

where $D(x,t)$ and $E(x,t)$ are the electric displacement and electric fields, $B(x,t)$ and $H(x,t)$ the magnetic flux and magnetic fields, $J(x,t)$ the current density, $\epsilon(x,\omega)$ the medium's permittivity, $\sigma(x,\omega)$ the electric conductivity, and μ_0 the permeability of free space (in non-magnetic media, the permeability is almost equal to that in vacuum), hold. Note that ϵ, σ and μ_0 can also depend on the excitation frequency ω [120].

From the *Ampère-Maxwell* and *Faraday* laws from Maxwell's equations

$$\nabla \times H(x,t) = J(x,t) + \partial_t D(x,t), \quad \nabla \times E(x,t) = -\partial_t B(x,t)$$

and the linear relations (1.3.2), one can obtain the *radiation equation* (in time or frequency domain, using $f(t) = \int_{-\infty}^{\infty} \hat{f}(\omega)e^{i\omega t}d\omega$)

$$\begin{aligned} &\frac{1}{v(x,\omega)^2}\partial_{tt}E(x,t) + \sigma(x,\omega)\mu_0\partial_t E(x,t) + \nabla\times\nabla\times E(x,t) = S(x,t) \\ &-\frac{\omega^2}{v(x,\omega)^2}\hat{E}(x,\omega) + \sigma(x,\omega)\mu_0 i\omega\hat{E}(x,\omega) + \nabla\times\nabla\times\hat{E}(x,\omega) = \hat{S}(x,\omega), \end{aligned} \tag{1.3.3}$$

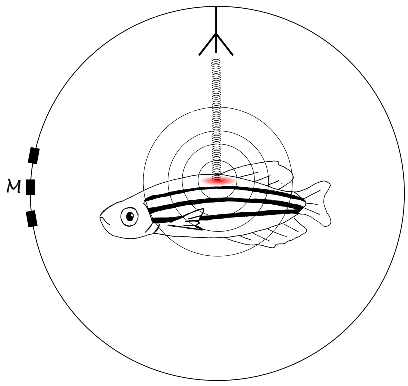

Figure 1.2.: Schematic representation of a Thermoacoustic Imaging setup. A sample is illuminated by a microwave pulse, which generates a pressure wave that can be detected outside the fish using ultrasound transducers.

where $S(x,t)$ is an electromagnetic source and $v(x,\omega) = \frac{1}{\sqrt{\mu_0 \epsilon(x,\omega)}}$ the speed of light in the medium. Following [31], we continue assuming that the source is a plane wave of the form

$$S(x,t) = e^{i\omega_0 t}\phi(t)s(x),$$

where ω_0 is the utilized frequency and $\phi(t)$ a time-envelope which describes the pulsing. Since we can reasonably assume $\phi \approx 1$ within a microwave period (which is of order 10^{-9} compared to the pulse length of approximately 10^{-6} seconds), we can assume $\hat{\phi}(\omega) \approx \delta(\omega)$ and thus

$$\sigma(x,\omega) \equiv \sigma(x,\omega_0) =: \sigma(x), \quad \epsilon(x,\omega) \equiv \epsilon(x,\omega_0) =: \epsilon(x)$$

in the applied frequency range. From (1.3.3), we find that

$$\begin{aligned}\hat{S}(x,\omega) &= \hat{\phi}(\omega - \omega_0)s(x)\\ \hat{E}(x,\omega) &= \hat{\phi}(\omega - \omega_0)e(x)\end{aligned}$$

where, using the vector analysis identity $\nabla \times \nabla \times F = \nabla(\nabla \cdot F) - \Delta F$,

$$\omega_0^2 \mu_0 \epsilon(x)e(x) + i\omega_0\mu_0\sigma(x)e(x) + \nabla(\nabla \cdot e(x)) - \Delta e(x) = s(x). \tag{1.3.4}$$

Accordingly, we get $E(x,t) = e^{i\omega_0 t}\phi(t)e(x)$. Up to rescaling of ϕ and s, the total absorbed radiation is given (using Joule's law) by

$$\begin{aligned}\mathcal{E}(x) &= \int_{-\infty}^{\infty} \mathrm{Re}[J(x,t)]\,\mathrm{Re}[E(x,t)]dt\\ &= \sigma(x)|e(x)|^2 \int_{-\infty}^{\infty} \mathrm{Re}[e^{i\omega_0 t}\phi(t)]^2 dt = \sigma(x)|e(x)|^2\end{aligned}$$

and the initial pressure (for which we, as in PAT, assume that the energy is delivered instantaneously with respect to ultrasound time scales) by

$$\mathcal{H}(x) = \Gamma(x)\,\mathcal{E}(x) = \Gamma(x)\sigma(x)|e(x)|^2,$$

where Γ is the Grüneisen coefficient. In this setting, the problem of quantitative Thermoacoustic Tomography is thus, given known ω_0 and $s(x)$ (and perhaps some of the unknown parameters and boundary values of e), to invert the mapping

$$(\sigma, \epsilon, \Gamma) \mapsto \Gamma\sigma|e|^2 =: \mathcal{H}(\sigma, \epsilon, \Gamma), \tag{1.3.5}$$

where e satisfies (1.3.4).

In [31], Bal et al. investigated the problem for known (homogeneous) permittivity ϵ (or, equivalently, v) and Γ, using a scalar approximation $u \approx |e|$ of (1.3.4) and with the source replaced by a known boundary condition g, that is,

$$\begin{aligned} k_0^2 u(x) + ik_0\xi\sigma(x)u(x) + \Delta u(x) = 0 \quad &\text{for all } x \in \Omega \\ u(x) = g(x) \quad &\text{for all } x \in \partial\Omega, \end{aligned} \tag{1.3.6}$$

where $k_0 = \frac{\omega_0}{v}$ is the wave number of the source and $\xi = -v\mu_0$ a constant assumed to be known. They were able to show that σ can be reconstructed from a single measurement $\mathcal{H}(\sigma)$ in a unique and L^2-stable manner. With a smallness requirement on σ, this result generalizes to the vectorial case (1.3.4). The approach was tested and found to work well on simulated data. Ammari et al. [12] analyzed the scalar model (1.3.6) (with known ϵ and Γ) with Robin boundary conditions and established an analytical reconstruction formula for σ from the ratios of multiple (well-chosen) measurements of $\mathcal{H}(\sigma)$.

Numerical work on this problem can be found in [95, 122] (using a fixed-point scheme which iteratively updates the estimated field e with (1.3.6) to obtain new estimates of σ). In [71, 72], Huang et al. validated this scheme experimentally (using phantom measurements and ex-vivo breast tissue).

1.4. Impedance-Acoustic Tomography

Impedance-Acoustic Tomography (IAT) (first introduced in [62]) is based on a coupling of an excitation using a short electrical pulse with ultrasound measurements. For a short time, electric current (with time envelope ϕ) is injected into an object to be probed. Via resistive heating, the absorbed electric energy leads to thermoelastic expansion of the material, and generates an ultrasound wave p. Similarly to Thermo- and Photoacoustic Tomography, under the assumption of thermal and stress confinement (which requires fast deposition of the electric energy), the wave $p(x,t)$ satisfies

$$\begin{aligned} \partial_{tt} p(x,t) - c^2(x)\Delta p(x,t) &= 0 \\ \partial_t p(x,0) &= 0 \\ p(x,0) &= \mathcal{H}(x), \end{aligned} \tag{1.4.1}$$

where $\mathcal{H}(x)$ denotes the *initial pressure* generated by the electric pulse and $c(x)$ the speed of sound. The same reconstruction techniques as in described in Section 1.2.1 for photoacoustic tomography can be utilized to obtain the initial pressure $\mathcal{H}$ from exterior ultrasound measurements on a measurement surface $\mathcal{M}$.

Quantitative Impedance-Acoustic Tomography, aims at a reconstruction of material coefficients of the sample (the electric conductivity σ and the Grüneisen coefficient Γ) from the initial pressure distribution $\mathcal{H}(x) = \Gamma(x)\,\mathcal{E}(x)$ (where, as before, $\mathcal{E}$ is the total absorbed energy) estimated by solving the acoustic inverse problem (1.4.1).

Following [62, 120], a model for the inverse problem can again be derived from *Maxwell's equations*. In frequency domain, using $f(t) = \int_{-\infty}^{\infty} \hat{f}(\omega) e^{i\omega t} d\omega$, the *Ampère-Maxwell* and *Faraday* laws in linear media (where (1.3.2) holds) read

$$\nabla \times \frac{1}{\mu_0}\hat{B}(x,\omega) = \sigma(\omega)\hat{E}(x,\omega) + i\omega\epsilon(\omega)\hat{E}(x,\omega), \quad \nabla \times \hat{E}(x,\omega) = -i\omega\hat{B}(x,\omega).$$

In the *electrostatic approximation*, it is assumed that the magnetic field B is time-independent, and that hence is electric field E is a gradient field, that is,

$$\nabla \times \hat{E}(x,\omega) = 0, \quad \hat{E}(x,\omega) = -\nabla\hat{U}(x,\omega), \tag{1.4.2}$$

where U is a (time-dependent) electric potential. According to Cheney et al. [42] this approximation is valid if $\sqrt{\omega\mu_0\sigma} \ll R$, where R is a reference size of the imaging system. Assuming further that $\omega \ll \frac{\sigma}{\epsilon}$, the time-dependent term (displacement current) in the *Ampère-Maxwell* law is negligible and we can apply the *quasi-static approximation*

$$\nabla \times \frac{1}{\mu_0}\hat{B}(x,\omega) = \sigma(\omega)\hat{E}(x,\omega). \tag{1.4.3}$$

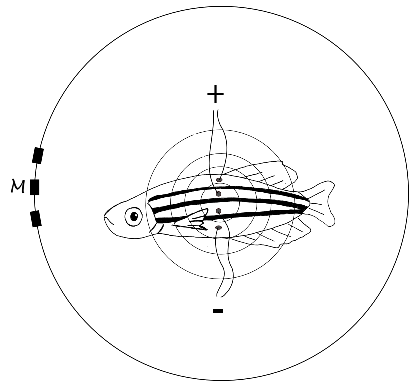

Figure 1.3.: Schematic representation of an Impedance-Acoustic Tomography setup. A fish is excited by a short electric pulse, which generates a pressure wave that can be detected outside the fish using ultrasound transducers.

Experiments show that in biological tissue, the electrostatic and quasi-static approximations are valid for frequencies less than 1 MHz [62, 108, 120]. If the electrical excitation is a rectangular pulse with a duration of 1 μs (which is sufficiently short to obtain a resolution of 1.5 mm, see [62]), that is, it has an envelope $\phi(t) = \mathrm{rect}(at)$ with $a = 10^6$, approximately 90% of the signal power $\hat{\phi}(\omega)^2 = (\frac{1}{|a|}\,\mathrm{sinc}(\frac{\omega}{a}))^2$ is below 1 MHz, so the approximations should be reasonably accurate.

By taking the divergence of (1.4.3) and using (1.4.2), we get

$$-\nabla \cdot (\sigma(x,\omega)\nabla \hat{U}(x,\omega)) = 0.$$

Assuming further that $\sigma(x,\omega) \equiv \sigma(x)$, i.e., that the conductivity is frequency independent in the applied range, since U responds linearly with $U(x,t) = \phi(t)u(x)$ to the applied voltage, we obtain

$$-\nabla \cdot (\sigma(x)\nabla u(x)) = 0 \tag{1.4.4}$$

and the total absorbed energy $\mathcal{E}$ is given (using Joule's law) by

$$\begin{aligned}\mathcal{E}(x) &= \int_{-\infty}^{\infty} J(x,t)E(x,t)dt \\ &= \sigma(x)|e(x)|^2 = \sigma(x)|\nabla u(x)|^2 \int_{-\infty}^{\infty} \phi(t)^2 dt = \sigma(x)|\nabla u(x)|^2,\end{aligned}$$

if we presuppose that the L^2-norm of ϕ is scaled to 1 (which implies that the energy density is equal to the *power density*).

Concluding, the problem of quantitative Impedance-Acoustic Tomography (in the quasi- and electrostatic regime) is the inversion of the mapping

$$(\sigma,\Gamma) \mapsto \Gamma\sigma|\nabla u|^2 =: \mathcal{H}(\sigma,\Gamma), \tag{1.4.5}$$

where u satisfies (1.4.4). As in qPAT or qTAT, sometimes boundary values of u (the applied voltage) or the unknown parameters are utilized for the inversion (and thus have to be measured).

To the authors knowledge, so far, all work on this inverse problem to date assumed that Γ is known and that hence the power density $\mathcal{E}$ can be estimated. This is partly due to the fact that problem of the determining of σ from measurements of $\mathcal{E} = \sigma|\nabla u|^2$ also appears in *Acousto-Electric Tomography (AET)* [9, 84, 128], also called *Ultrasound-Modulated Electrical Impedance Tomography (UMEIT)*, a coupled physics imaging method which couples *ultrasound perturbations* of the tissue with an *electrical impedance tomography (EIT)* setup which can measure boundary currents generated by applied voltage.

By substituting $\sigma = \frac{\mathcal{E}}{|\nabla u|^2}$ in (1.4), this inverse problem can be recast as a (heterogeneous) p-Laplace equation (an equation of independent interest with a wide range of applications)

$$-\nabla \cdot \left(\gamma(x)|\nabla u(x)|^{p-2}\,\nabla u(x)\right) = 0,$$

with $p = 0$, $\gamma = \mathcal{E}$. This problem was investigated in [19], showing that in general, unique and stable reconstructions from one measurement of $\mathcal{E}$ are only possible on a subset of the domain.

Under the assumption that multiple measurements of the power density $\mathcal{E}_k$ (as well as their generating boundary excitations $g_k = u_k|_{\partial\Omega}$) are given, the problem was analyzed by Capdeboscq et al. in [40] for two spatial dimensions. Using an analytical procedure, they showed that unique reconstruction of σ from three functions $S_{i,k} = \sigma\nabla u_i \cdot \nabla u_k$, where $i, k = 1, 2$ (which can be calculated from two measurements of the power density $\mathcal{E}_1 = \sigma|\nabla u_1|, \mathcal{E}_2 = \sigma|\nabla u_2|$ using the polarization formula), is possible. The reconstruction relies on the condition

$$\det(\nabla u_1(x), \nabla u_2(x)) > 0 \quad \text{for all } x \in \Omega, \tag{1.4.6}$$

which can be forced by a specific choice of boundary voltages g_1, g_2.

Bal et al. generalized this approach to three spatial dimensions in [21]. Using four measurements of the power density $\mathcal{E}$ they showed that σ can be reconstructed unique and stably (albeit taking the $W^{1,\infty}$-norm in the data space, i.e., assuming differentiable perturbations). A similar condition to (1.4.6) has to be satisfied, which can be guaranteed if the generating boundary voltages g_k satisfy certain assumptions (in the paper, they are constructed using *complex geometric optics* solutions, which, however, depend on the unknown conductivity σ). For more details on enforcing local conditions such as (1.4.6) by choice of boundary conditions, see also [3, 22].

In [85], the linearized inverse problem (which approximates the non-linear problem well for small perturbations from a constant conductivity) is analyzed and shown to uniquely and stably solvable using two measurements (in 2D) and three measurements (in 3D) of $\mathcal{E}$. See also [11] for a detailed stability analysis. In the same vein, in [86], the linearized inverse problem was found to be elliptic (which guarantees stable reconstructions once uniqueness is established) if (1.4.6) holds, for a similar approach see also [18].

Some of the uniqueness results were generalized to the case of anisotropic conductivities σ, see [24, 26].

Numerical work (using simulated data) on the the quantitative reconstruction problem can be found in [9, 40, 62, 69, 85]. To the authors knowledge, no physical experiments to verify IAT or AET have been performed to date.

2. Quantitative photoacoustic tomography with piecewise constant material parameters

Authors and Contributions. The authors are Wolf Naetar and Otmar Scherzer. The development of this article was a gradual, cooperative process. The author list is alphabetical, every author made significant contributions to the paper.

Publication Status. Published in [94]. Publication available for download at http://dx.doi.org/10.1137/140959705. The version contained in this Chapter is a preprint available at http://arxiv.org/abs/1403.2620.

Quantitative photoacoustic tomography with piecewise constant material parameters

W. Naetar (wolf.naetar@univie.ac.at)[1]
O. Scherzer (otmar.scherzer@univie.ac.at)[1,2]

[1]Computational Science Center, University of Vienna
Oskar Morgenstern-Platz 1, A-1090 Vienna, Austria

[2]Radon Institute of Computational and Applied Mathematics, Austrian Academy of Sciences
Altenbergerstr. 69, A-4040 Linz, Austria

September 21, 2015

The goal of *quantitative* photoacoustic tomography is to determine optical and acoustical material properties from initial pressure maps as obtained, for instance, from photoacoustic imaging. The most relevant parameters are absorption, diffusion and Grüneisen coefficients, all of which can be heterogeneous. Recent work by Bal and Ren shows that in general, unique reconstruction of all three parameters is impossible, even if multiple measurements of the initial pressure (corresponding to different laser excitation directions at a single wavelength) are available.

Here, we propose a restriction to piecewise constant material parameters. We show that in the diffusion approximation of light transfer, piecewise constant absorption, diffusion *and* Grüneisen coefficients can be recovered uniquely from photoacoustic measurements at a single wavelength. In addition, we implemented our ideas numerically and tested them on simulated three-dimensional data.

Keywords. Quantitative photoacoustic tomography, mathematical imaging, inverse problems

AMS subject classifications. 35R25, 35R30, 65J22, 92C55

2.1. Introduction

Photoacoustic tomography (PAT) is a hybrid imaging technique utilizing the coupling of laser excitations with ultrasound measurements. Tissue irradiated by a short monochromatic laser pulse generates an ultrasound signal (due to thermal expansion) which can be measured by ultrasound transducers outside the medium. From these measurements, the ultrasound wave's initial pressure (whose spatial variation depends on material properties of the tissue) can be reconstructed uniquely by solving a well-studied inverse problem for the wave equation. For further information on this inverse problem, see, e.g., Kuchment and Kunyansky [83].

The obtained ultrasound initial pressure *qualitatively* resembles the structure of the tissue (i.e., its inhomogeneities are visible). It is, however, desirable to image material parameters (whose values can serve as diagnostic information) instead. That is the goal of *quantitative* photoacoustic tomography (qPAT).

Mathematically, the problem can be posed as follows. In biological tissue, where photon scattering is a dominant effect compared to absorption, light transfer can be described by the *diffusion approximation* of the *radiative transfer equation*. It is valid in regions $\Omega \subset \mathbb{R}^3$ with sufficient distance to the light source and is given by

$$-\operatorname{div}(D(x)\nabla u(x)) + \mu(x)u(x) = 0. \tag{2.1.1}$$

$u(x)$ denotes the *fluence* (that is, the laser energy per unit area at a point x), $\mu(x)$ the *absorption coefficient* (the photon absorption probability per unit length) and $D(x) = \frac{1}{3(\mu+\mu_s')}$ (where $\mu_s'(x)$ denotes the *reduced scattering coefficient*) the *diffusion coefficient*. Both μ and D vary spatially and depend on the wavelength of the laser excitation. For details and a derivation of the diffusion approximation, we refer to [15, 117].

In the literature, (2.1.1) is commonly augmented with Dirichlet boundary conditions (which, in practice, might not be known) or, at interfaces with non-scattering media, Robin-type boundary conditions (see, for instance, [117]).

In this model, the absorbed laser energy $\mathcal{E}(x)$ is given by

$$\mathcal{E}(x) = \mu(x)u(x). \tag{2.1.2}$$

The ultrasound initial pressure Γ obtained by photoacoustic imaging is proportional to the absorbed energy $\mathcal{E}$, so we have

$$\mathcal{H}(x) = \Gamma(x)\,\mathcal{E}(x) = \Gamma(x)\mu(x)u(x). \tag{2.1.3}$$

The (spatially varying) dimensionless constant Γ is called the Grüneisen parameter, its value corresponds to the conversion efficiency from change in thermal energy to pressure.

Hence, the goal in qPAT is to find the parameters μ, D, Γ in a domain Ω given

$$\mathcal{H}^k = \Gamma \mu u^k, \quad k = 1, \ldots, K$$

where u^k solves (2.1.1) in Ω (here and in the following, the index k corresponds to varying laser excitation directions).

Previous work on this problem (and variations of it) can be found, e.g., in [10, 28, 30, 32, 34, 44, 45, 61, 88, 101, 104, 106, 115, 125, 127]. For a more comprehensive list, we refer to the review article [46] by Cox et al.

In particular, Bal and Ren showed (see [28]) that unique reconstruction of all three parameters μ, D, Γ is impossible, independent of the number of measurements $\mathcal{H}^k$. They suggested to overcome this problem by the use of *multi-spectral data* (i.e., multiple photoacoustic measurements generated by laser excitations at different wavelengths). Using these data, unique reconstruction of all three material parameters (at the respective wavelengths used), becomes possible [30].

In our paper, we take a different approach and propose a restriction to piecewise constant μ, D, Γ. Similar restrictions (due to the large number of publications which use this approach we only provide a small selection of references) have been proposed for *Diffusion Optical Tomography* (e.g., [16, 68, 81, 126]) and *Conductivity Imaging* (e.g., [36, 52, 79, 103]).

For our problem, it turns out that the reconstruction problem becomes a lot simpler and admits a unique solution for all three parameters μ, D, Γ.

The result is based on an analytical, explicit reconstruction procedure consisting of two steps. First, we recover the regions where μ, D, Γ are constant by finding the discontinuities of photoacoustic data $\mathcal{H}$ and its derivatives up to second order (see Proposition 1). In the second step, we determine the actual values of μ, D, Γ from the jumps of $\mathcal{H}$ and $\nabla \mathcal{H} \cdot \nu$ (the normal derivatives) across the obtained region boundaries (cf. Proposition 2). Our result holds under certain conditions on the parameters μ, D, Γ and the direction of ∇u. We emphasize that we don't necessarily require that $u|_{\partial\Omega}$ is known (which may not be the case in practice) or that specific boundary conditions hold on $\partial\Omega$. Instead, we use reference values of the parameters for reconstruction, i.e., values of one of the pairs $(\mu(x), \Gamma(x))$ or $(D(x), \Gamma(x))$ at a single point $x \in \Omega$.

Numerically, the reconstruction method we present heavily relies on an efficient *jump detection* algorithm (using a computational edge detection method) and subsequent *3D-image segmentation*, which provides a connection with image analysis.

The paper is organized as follows. In section 2.2, we recap some of the non-uniqueness results for the qPAT problem in literature. In section 2.3, we prove unique solvability for piecewise constant μ, D, Γ. In section 2.4, we give an example of how our ideas can be applied numerically. The last section contains two concrete numerical examples where the reconstruction method is applied to simulated data (with one data set FEM-generated and one data set generated by Monte Carlo simulations). The paper ends with a conclusion.

2.2. Ill-posedness of qPAT with smooth parameters

In this section, we review some of the non-uniqueness results for quantitative photoacoustic tomography. For simplicity of presentation, we augment (in this section only) equation (2.1.1) with Dirichlet boundary conditions, so we have

$$\begin{aligned} -\operatorname{div}(D(x)\nabla u(x)) + \mu(x)u(x) &= 0 \quad \text{in } \Omega \subset \mathbb{R}^3 \\ u(x)|_{\partial\Omega} &= f(x). \end{aligned} \tag{2.2.1}$$

The boundary values represent the laser illumination of one particular experiment. In this section, we assume f is known, satisfies $f > 0$ and is sufficiently smooth.

It is well-known and has been shown numerically (see [44, 106]) that even when the Grüneisen coefficient Γ is known (so the absorbed energy $\mathcal{E} = \mu u$ can be calculated from $\mathcal{H}$), different pairs of diffusion and absorption coefficients may lead to the same absorbed energy map $\mathcal{E}$. To see this analytically, for given smooth coefficients $D, \mu > 0$ let $u(D, \mu)$ be the corresponding smooth solution of (2.2.1) and $\mathcal{E}(\mu, D) = \mu u(D, \mu)$ the absorbed energy. By the strong maximum principle (see [63, Theorem 3.5]), $u(D, \mu) > 0$ in Ω (since $f > 0$).

Moreover, for fixed $\mathcal{E} = \mathcal{E}(\mu, D)$, let us denote by $v(\tilde{D})$ the solution of

$$\begin{aligned} \operatorname{div}(\tilde{D}(x)\nabla v(x)) &= \mathcal{E}(x) \quad \text{in } \Omega \\ v(x)|_{\partial\Omega} &= f(x). \end{aligned} \tag{2.2.2}$$

Note that $v(D) = u(D, \mu) > 0$. Then, for every $\tilde{D}$ with

$$\left\| D - \tilde{D} \right\|_{1,\infty} < \epsilon$$

(with ϵ small enough), we also have $v(\tilde{D}) > 0$. To see this, note that

$$\begin{aligned} \operatorname{div}(\tilde{D}\nabla(v(\tilde{D}) - v(D))) &= -\operatorname{div}((\tilde{D} - D)\nabla v(D)) \quad \text{in } \Omega \\ (v(\tilde{D}) - v(D))|_{\partial\Omega} &= 0 \end{aligned}$$

Using a priori bounds [63, Theorem 3.5],

$$\left\| v(\tilde{D}) - v(D) \right\|_{\infty} \leq C_1 \left\| \operatorname{div}((\tilde{D} - D)\nabla v(D)) \right\|_{\infty} \leq C_2 \left\| \tilde{D} - D \right\|_{1,\infty},$$

which implies $v(\tilde{D}) > 0$ if ϵ is sufficiently small.

Now, taking $\tilde{\mu} = \frac{\mathcal{E}(\mu,D)}{v(\tilde{D})}$, we get

$$\operatorname{div}(\tilde{D}\nabla v(\tilde{D})) - \tilde{\mu} v(\tilde{D}) = 0.$$

Hence, $v(\tilde{D}) = u(\tilde{D}, \tilde{\mu})$ and $\mathcal{E}(\tilde{\mu}, \tilde{D}) = \tilde{\mu} u(\tilde{D}, \tilde{\mu}) = \mathcal{E}(\mu, D)$, which shows that infinitely many pairs of coefficients may create the same absorbed energy map.

This nonuniqueness can be overcome by varying f (i.e., changing the illumination pattern), obtaining multiple absorbed energy maps. This approach is called *multi-source* quantitative photoacoustic tomography. Bal and Ren [28] showed that while this additional information leads to unique reconstruction of μ, D from $\mathcal{E}$, finding three unknown parameters μ, D, Γ given $\mathcal{H} = \Gamma\mu u$ is still impossible, independent of the number of illuminations (any more than two do not add any information). In fact, they showed that for *any* given Lipschitz continuous μ, D or Γ the other two parameters can be chosen such that given initial pressures $\mathcal{H}^k = \Gamma\mu u^k$ (for multiple illumination patterns f^k) are generated.

Example 1. Given any set of parameters (μ, D, Γ), for every $\lambda > 0$, $(\lambda\mu, \lambda D, \frac{1}{\lambda}\Gamma)$ generate the same measurements, since (2.2.1) is invariant under simultaneous scaling of μ and D.

This simple example shows that even for constant parameters knowledge of f and $\mathcal{H}$ is insufficient to determine μ, D, Γ. Hence, more prior information about the unknown parameters will be necessary in order to get a unique solution.

2.3. Reconstruction of piecewise constant parameters

To overcome this essential non-uniqueness, we assume that μ, D, Γ are piecewise constants. That is, for some partition $(\Omega_m)_{m=1}^M$ of $\Omega \subset \mathbb{R}^3$,

$$\overline{\Omega} = \bigcup_{m=1}^{M} \overline{\Omega}_m, \quad \mu = \sum_{m=1}^{M} \mu_m 1_{\Omega_m}, \quad D = \sum_{m=1}^{M} D_m 1_{\Omega_m}, \quad \Gamma = \sum_{m=1}^{M} \Gamma_m 1_{\Omega_m}. \tag{2.3.1}$$

Since the parameters are discontinuous, we need a generalized solution concept. Under certain additional conditions (which we explain in detail in Appendix 2.8.1) a weak solution u of (2.2.1) with piecewise constant parameters μ, D can be characterized by

$$u \in C^{\alpha}(\overline{\Omega}) \tag{2.3.2}$$

for some $\alpha > 0$ and, for $m = 1, \ldots, M$,

$$\begin{aligned} u_m &:= u|_{\Omega_m} \in C^\infty(\Omega_m) \\ D_m \Delta u_m - \mu_m u_m &= 0 \quad \text{in } \Omega_m \end{aligned} \tag{2.3.3}$$

and, almost everywhere on interfaces $I_{mn} := \partial\Omega_m \cap \partial\Omega_n$,

$$D_m \nabla u_m \cdot \nu = D_n \nabla u_n \cdot \nu \quad \text{(for any normal vector } \nu). \tag{2.3.4}$$

The transmission condition (2.3.4) is ill-defined on corners and intersections of multiple subregions, therefore we can only expect it to hold almost everywhere. For details and a derivation, see Appendix 2.8.1. The transmission condition (2.3.4) can also be derived physically (rather than starting from a weak solution), it is accurate within the scope of the diffusion approximation [13, 102].

From now on, we consider u_m and $\mathcal{H}_m := \mathcal{H}|_{\Omega_m} = \Gamma_m \mu_m u_m$ (and their derivatives up to second order) continuously extended (from the inside) to $\partial\Omega_m$. We emphasize that for ∇u_m and $\nabla \mathcal{H}_m$, this may only be possible for almost all points (with respect to the surface measure), see Appendix 2.8.1.

We also assume that u is strictly positive and bounded from above in $\overline{\Omega}$.

In the following Proposition 1, we show that the jump set $\bigcup_m \partial\Omega_m$ of piecewise constant parameters μ, D, Γ can be determined from photoacoustic initial pressure data $\mathcal{H} = \Gamma\mu u$. For $k \geq 0$, denote by

$$J_k(f) = \Omega \setminus \bigcup \{B \subset \Omega | B \text{ is open and } f \in C^k(B)\}$$

the set of discontinuities of a function $f \in L^\infty(\Omega)$ and its derivatives up to k-th order.

We require an assumption on ∇u and the unknown parameters μ, D, Γ. For all $x \in J_0(D) \setminus (J_0(\Gamma\mu) \cup J_0(\frac{\mu}{D})) \subset \partial\Omega_m \cap \partial\Omega_n$ (i.e., interfaces of D which are not interfaces of $\Gamma\mu$ and $\frac{\mu}{D}$) we require that the fluence u satisfies almost everywhere (where ν denotes a normal vector on $\partial\Omega_m \cap \partial\Omega_n$),

$$|\nabla u_n(x) \cdot \nu(x)| > 0 \quad (\overset{(2.3.4)}{\iff} |\nabla u_m(x) \cdot \nu(x)| > 0). \tag{2.3.5}$$

Proposition 1. *Let μ, D, Γ be of the form (2.3.1) and $u = \sum_m u_m 1_{\Omega_m}$ and $\mathcal{H} = \sum_m \mathcal{H}_m 1_{\Omega_m}$ the corresponding fluence and initial pressure distributions satisfying condition (2.3.5) in Ω. Then,*

$$\overline{J_0(\mu)} \cup \overline{J_0(D)} \cup \overline{J_0(\Gamma)} = \overline{J_2(\mathcal{H})}.$$

Proof. Let $B \subset \Omega$ be an open ball with $B \cap (J_0(\mu) \cup J_0(D) \cup J_0(\Gamma)) = \emptyset$. Since u solves an elliptic PDE with constant coefficients in B, we have $u \in C^\infty(B)$ by interior regularity. Hence $\mathcal{H} \in C^\infty(B)$ (since $\Gamma\mu$ is constant in B), which implies $J_2(\mathcal{H}) \subset J_0(\mu) \cup J_0(D) \cup J_0(\Gamma)$.

To show the converse, take $x \in \Omega$ such that $x \in J_0(\mu) \cup J_0(D) \cup J_0(\Gamma)$ (that is, one of the parameters jumps at x). We have to show that $x \in \overline{J_2(\mathcal{H})}$.

Let m, n be such that $x \in I_{mn} = \partial\Omega_m \cap \partial\Omega_n$. We distinguish three cases:

(1) $\Gamma_m\mu_m \neq \Gamma_n\mu_n$: Since u is continuous across I_{mn} (cf. Appendix 2.8.1), $\mathcal{H} = \Gamma\mu u$ is discontinuous at x, so we get $x \in J_0(\mathcal{H}) \subset J_2(\mathcal{H})$.

(2) $\Gamma_m\mu_m = \Gamma_n\mu_n$, $\frac{\mu_m}{D_m} \neq \frac{\mu_n}{D_n}$: From (2.3.3) and $u \in C(\overline{\Omega})$ we get

$$\Delta u_m(x) = \frac{\mu_m}{D_m} u_m(x) \neq \frac{\mu_n}{D_n} u_n(x) = \Delta u_n(x).$$

Hence $x \in J_2(u)$, which implies $x \in J_2(\mathcal{H})$ since $\Gamma\mu$ is constant in $\Omega_m \cup \Omega_n$.

(3) $\Gamma_m\mu_m = \Gamma_n\mu_n, D_n \neq D_m$: First, let $x \in I_{mn}$ be a point where the transmission condition (2.3.4) and (2.3.5) hold (by assumption, this is the case for almost all points with respect to the surface measure). We have

$$\begin{aligned} |\nabla u_m(x) - \nabla u_n(x)| &\geq |(\nabla u_m(x) - \nabla u_n(x)) \cdot \nu(x)| \\ &\geq \left|1 - \frac{D_m}{D_n}\right| |\nabla u_m(x) \cdot \nu(x)| > 0. \end{aligned}$$

This shows that $x \in J_1(u)$, which implies $x \in J_1(\mathcal{H})$ and thus $x \in J_2(\mathcal{H})$. By taking the closure, we get $x \in \overline{J_2(\mathcal{H})}$ for all $x \in I_{mn}$.

The cases (1)-(3) cover all possibilities, since otherwise all three parameters μ, D, Γ would be constant in $\Omega_m \cup \Omega_n$. □

Proposition 1 shows that we can obtain the parameter discontinuities (in regions where (2.3.5) holds) via the set $J_2(\mathcal{H})$. In fact, the proof tells us that $\mathcal{H}$, $\nabla\mathcal{H}$ or $\Delta\mathcal{H}$ have jumps at discontinuities of μ, D or Γ. That is, images of the gradient and Laplacian of the data $\mathcal{H}$ show material inhomogeneities not visible in $\mathcal{H}$.

In the next Proposition, we show how to recover piecewise constant parameters μ, D, Γ once their jump set $\bigcup_m \partial\Omega_m$ is known (e.g., from Proposition 1). Knowledge of boundary values of u alone is insufficient to fully determine the parameters (see Example 1). We also have to require knowledge of the parameters in some $\Omega_n \subset \Omega$, $n \in \{1, \dots, M\}$. Using the continuity of u, (2.3.3) and (2.3.4), we will show that these reference values combined with photoacoustic measurements $\mathcal{H} = \Gamma\mu u$ suffice to determine μ, D, Γ everywhere.

For this result, we again need an assumption on ∇u. For every interface $I_{mn} =$

$\partial\Omega_m \cap \partial\Omega_n$ with normal vector $\nu(x)$, we require the existence of some $x \in I_{mn}$ with

$$\nabla u_n(x) \cdot \nu(x) \neq 0 \quad \big(\overset{(2.3.4)}{\Longleftrightarrow} \nabla u_m(x) \cdot \nu(x) \neq 0 \big), \tag{2.3.6}$$

that is, on every interface I_{mn} there must exist a point where ∇u is not tangential.

Proposition 2. *Let μ, D, Γ be of the form (2.3.1) (with the decomposition (Ω_m) of Ω known). Furthermore, let u and $\mathcal{H} = \Gamma\mu u$ be corresponding fluence and initial pressure distribution which satisfy condition (2.3.6) on every interface $I_{mn} \subset \Omega$. Furthermore, let (μ_n, D_n, Γ_n) be known for some n. Then the parameters μ, D, Γ can be determined uniquely from $\mathcal{H}$.*

Proof. Let Ω_m be a neighbouring subregion to Ω_n and denote by $I_{mn} = \partial\Omega_m \cap \partial\Omega_n$ the interface. By continuity of u and (2.1.3), we have for all $y \in I_{mn}$

$$\Gamma_m \mu_m = \frac{\mathcal{H}_m(y)}{\mathcal{H}_n(y)} \, \Gamma_n \mu_n \tag{2.3.7}$$

so from the reference values and $\mathcal{H}$ we can calculate $\Gamma\mu$ on neighbouring Ω_m.

Next, let $x \in \partial\Omega_m \cap \partial\Omega_n$ such that $\nabla u_n(x) \cdot \nu(x) \neq 0$. Using (2.3.4) and $\nabla\mathcal{H}_k = \Gamma_k \mu_k \nabla u_k$ for all k (since the parameters are constant in Ω_k) we get

$$\frac{D_m}{\Gamma_m \mu_m} = \frac{(\nabla\mathcal{H}_n \cdot \nu)(x)}{(\nabla\mathcal{H}_m \cdot \nu)(x)} \frac{D_n}{\Gamma_n \mu_n}. \tag{2.3.8}$$

Finally we get for all in $z \in \Omega_m$, from (2.3.3) and $\Delta H_m = \Gamma_m \mu_m \Delta u_m$ in Ω_m,

$$\frac{\mu_m}{D_m} = \frac{\Delta\mathcal{H}_m(z)}{\mathcal{H}_m(z)}. \tag{2.3.9}$$

The equations (2.3.7)-(2.3.9) suffice to obtain μ_m, D_m and Γ_m, since we have

$$(\mu, D, \Gamma) = \left(ABC, AB, \frac{1}{BC} \right), \tag{2.3.10}$$

for $A = \Gamma\mu$, $B = \frac{D}{\Gamma\mu}$, $C = \frac{\mu}{D}$.

By iterating over all interfaces, we can find μ, D, Γ everywhere in Ω. □

Note that in Proposition 2, no knowledge of boundary values of u is required, values of the parameters μ_n, D_n, Γ_n in some Ω_n are enough. In fact, knowledge of two of the three parameters already suffices, as we will show in the following Proposition.

Proposition 3. *For a given n, the constants (μ_n, D_n, Γ_n) can be determined uniquely from photoacoustic data $\mathcal{H}_n = \Gamma_n\mu_n u_n$ and knowledge of one of the pairs (μ_n, Γ_n) or (D_n, Γ_n). If $u(x)$ is known for some $x \in \Omega_n$, knowing one of the three constants is enough. If only one of the parameters μ_n, D_n, Γ_n, only u_n, or the only pair (μ_n, D_n) is known, (μ_n, D_n, Γ_n) cannot be determined uniquely.*

Proof. From (2.3.3) and $\mathcal{H} = \Gamma\mu u$, we know that in Ω_n

$$\begin{aligned} D_n\Delta u_n - \mu_n u_n &= 0 \\ \Gamma_n\mu_n u_n &= \mathcal{H}_n, \end{aligned}$$

which is equivalent to

$$\begin{aligned} \Gamma_n D_n\Delta u_n &= \mathcal{H}_n \\ \Gamma_n\mu_n u_n &= \mathcal{H}_n \\ \Gamma_n\mu_n\Delta u_n &= \Delta\mathcal{H}_n. \end{aligned} \tag{2.3.11}$$

Here, one can immediately see that if $u(x)$ is known for some $x \in \Omega_n$, we can calculate $u_n(y) = \frac{1}{\Gamma_n\mu_n}\mathcal{H}_n(y) = \frac{u(x)}{\mathcal{H}(x)}\mathcal{H}_n(y)$ for all $y \in \Omega_n$ and thus also Δu_n . Clearly, (μ_n, D_n, Γ_n) can now be determined from (2.3.11) if one of the parameters is known.

Likewise, given one of the pairs (μ_n, Γ_n) or (D_n, Γ_n) we can to calculate all three constants (μ_n, D_n, Γ_n).

Knowledge of (μ_n, D_n), on the other hand, is insufficient because λu_n, $\frac{1}{\lambda}\Gamma_n$ satisfy (2.3.11) for given (μ_n, D_n) for all $\lambda > 0$. Similarly, the system is underdetermined if only u_n or Γ_n is known.

$\square$

Conditions (2.3.5) and (2.3.6) are vital for unique reconstruction. For instance, using Lemma 2 one can see that, $u(x, y, z) = e^x$ is a weak solution of (2.1.1) in $\mathbb{R}^3$ for both

$$\mu \equiv 1, \quad D \equiv 1, \quad \Gamma \equiv 1$$

and

$$\tilde{\mu} = \begin{cases} 1 & \text{if } y \geq 0 \\ \lambda & \text{if } y < 0 \end{cases}, \quad \tilde{D} = \begin{cases} 1 & \text{if } y \geq 0 \\ \lambda & \text{if } y < 0 \end{cases}, \quad \tilde{\Gamma} = \begin{cases} 1 & \text{if } y \geq 0 \\ \frac{1}{\lambda} & \text{if } y < 0 \end{cases}, \quad \lambda > 0$$

since u is a classical solution on both sides of the interface $\{y = 0\}$ and it satisfies $\nabla u \cdot \nu = 0$. Furthermore, both parameter sets generate the same data $\mathcal{H}(x, y, z) = e^x$.

More generally, parts of interfaces where condition (2.3.5) fails to hold don't necessarily lie in $J_2(\mathcal{H})$ and may thus be invisible to our reconstruction procedure (depending on the geometry, this may also lead to follow-up errors). If condition (2.3.6) fails to hold, it might not be possible to determine μ, D, Γ everywhere.

To overcome this problem, we can use additional measurements (with different illumination directions) and hope that the location of critical points and gradient directions change. In particular, if photoacoustic data $(\mathcal{H}^k)_{k=1}^K$ corresponding to solutions $(u^k)_{k=1}^K$ of (2.1.1) that satisfy for almost all $x \in \Omega$

$$\max_{i,j,k} \left|\det(\nabla u^i(x), \nabla u^j(x), \nabla u^k(x))\right| > 0 \tag{2.3.12}$$

are available, on every $x \in I_{mn}$, one of the measurements satisfies (2.3.5), since the gradients form a basis.

With a similar argument as in Proposition 1 one can show that in this case

$$J_0(\mu) \cup J_0(D) \cup J_0(\Gamma) = \bigcup_{k=1}^K J_2(\mathcal{H}^k),$$

so unique reconstruction of μ, D, Γ in Ω can be guaranteed. To our knowledge, no method to force condition (2.3.12) by boundary conditions or choice of source is known, however, its validity can be checked by looking at the data $(\mathcal{H}^k)_{k=1}^K$.

2.4. Numerical reconstruction

In this section, we show how the results in the last section can be utilized numerically. Our goal is to estimate unknown piecewise constant parameters μ, D, Γ from noisy three-dimensional photoacoustic data $(\mathcal{H}^k)_{k=1}^K$ (with varying boundary excitations) sampled on a regular grid.

We propose a two-step reconstruction:

(1) Detect jumps in $(\mathcal{H}^k)_{k=1}^K$, $(\nabla\mathcal{H}^k)_{k=1}^K$, $(\Delta\mathcal{H}^k)_{k=1}^K$ and use the obtained surfaces to segment the image domain Ω to estimate subregions $(\hat{\Omega}_m)_{m=1}^M$ where the parameters are constant (and thus $\mathcal{H}$ is smooth).

(2) Given $(\hat{\Omega}_m)_{m=1}^M$ and reference values (μ_1, D_1, Γ_1), use the jump values of $(\mathcal{H}^k)_{k=1}^K$ and $(\nabla\mathcal{H}^k \cdot \nu)_{k=1}^K$ across the estimated interfaces and values of $(\frac{\Delta\mathcal{H}^k}{\mathcal{H}^k})_{k=1}^K$ to find μ, D, Γ everywhere in Ω (using equations (2.3.7)-(2.3.10)).

2.4.1. Finding regions where the parameters are constant

In the proof of Proposition 1, one can see that in regions Ω where (2.3.5) holds, discontinuities of the (piecewise constant) parameters μ, D, Γ correspond to jumps of $\mathcal{H}$, $\nabla\mathcal{H}, \Delta\mathcal{H}$. We want to use *computational edge detection* to find these jumps.

We start by finding jumps in $\mathcal{H}$. Since they are multiplicative (i.e., $\frac{H_m}{H_n}$ is constant on I_{mn}), we apply a logarithm transformation to get constant jumps along the interfaces. In fact, let $I_{mn} = \partial\Omega_m \cap \partial\Omega_n$ be an interface of the parameters μ, D, Γ. Since $u_m = u_n$ on I_{mn}, we have

$$|\log(\mathcal{H}_n) - \log(\mathcal{H}_m)| = |\log(\Gamma_n\mu_n) - \log(\Gamma_m\mu_m)| \text{ on } I_{mn},$$

so jumps in $\Gamma\mu$ lead to jumps of equal magnitude in $\log\mathcal{H}$.

Next, we show that jumps in D (that are large enough compared to those in $\Gamma\mu$) lead to jumps in $\log|\nabla\mathcal{H}|$. We restrict our search domain to $\Omega' \subset \Omega$ such that $|\nabla\mathcal{H}| \geq d > 0$ holds in Ω'. Due to continuity of u we have $\nabla u_m \cdot \tau = \nabla u_n \cdot \tau$ (for tangential vectors τ) on parts of I_{mn} that are C^1. Thus, we obtain on parts of $I_{mn} \cap \Omega'$ where (2.3.4) holds,

$$\begin{aligned}
\frac{|\nabla u_n|^2}{|\nabla u_m|^2} &= \frac{(\nabla u_n \cdot \nu)^2 + (\nabla u_n \cdot \tau)^2}{|\nabla u_m|^2} \overset{(2.3.4)}{=} \left(\frac{D_m}{D_n}\right)^2 \frac{(\nabla u_m \cdot \nu)^2}{|\nabla u_m|^2} + \frac{(\nabla u_m \cdot \tau)^2}{|\nabla u_m|^2} \\
&= 1 + \left(\left(\frac{D_m}{D_n}\right)^2 - 1\right)\cos(\alpha_m)^2,
\end{aligned}$$

where α_m denotes the angle between the unit normal ν and ∇u_m. Using $D_m \geq D_n$ (without loss of generality, otherwise we swap indices), we get

$$\begin{aligned}
|\log|\nabla u_n| - \log|\nabla u_m|| &\geq \frac{1}{2}\log\left(1 + \left(e^{2|\log D_m - \log D_n|} - 1\right)\min_{\Omega,k}\cos(\alpha_k)^2\right) \\
&:= \gamma\left(|\log D_m - \log D_n|\right).
\end{aligned}$$

If $\min_{\Omega,k}\cos(\alpha_k)^2 > 0$ holds in Ω', the function γ is positive, strictly increasing and unbounded. Hence, using the reverse triangle inequality,

$$\begin{aligned}
|\log(|\nabla\mathcal{H}_n|) - \log(|\nabla\mathcal{H}_m|)| &= |\log(\Gamma_n\mu_n) - \log(\Gamma_m\mu_m) + \log|\nabla u_n| - \log|\nabla u_m|| \\
&\geq |\log|\nabla u_n| - \log|\nabla u_m|| - |\log(\Gamma_n\mu_n) - \log(\Gamma_m\mu_m)| \\
&\geq \gamma\left(|\log D_m - \log D_n|\right) - |\log(\Gamma_n\mu_n) - \log(\Gamma_m\mu_m)|.
\end{aligned}$$

Finally, since $\frac{\Delta\mathcal{H}_m}{\mathcal{H}_m} = \frac{\mu_m}{D_m}$ for all m, we get on I_{mn}

$$\left|\log\left(\frac{\Delta\mathcal{H}_m}{\mathcal{H}_m}\right) - \log\left(\frac{\Delta\mathcal{H}_n}{\mathcal{H}_n}\right)\right| = \left|\log\left(\frac{\mu_m}{D_m}\right) - \log\left(\frac{\mu_n}{D_n}\right)\right|$$

which shows that jumps in $\log\left(\frac{\mu}{D}\right)$ lead to jumps of equal magnitude in $\log\left(\frac{\Delta\mathcal{H}}{\mathcal{H}}\right)$.

To ensure that $|\nabla\mathcal{H}| \geq d > 0$ holds, we enforce a minimum for $|\nabla\mathcal{H}|$ (to avoid creating singularities). We counter failure of $\min_{\Omega,k}\cos(\alpha_k)^2 > 0$ by using additional measurements.

To estimate $(\Omega_m)_{m=1}^M$ given noisy data $\mathcal{H}^k$, we first look for jumps in $\log(\mathcal{H}^k)$, then $\log|\nabla\mathcal{H}^k|$ and last in $|\log(\Delta\mathcal{H}^k) - \log(\mathcal{H}^k)|$. More precisely, we proceed as follows:

(1) Find $\hat{J}_0 \subset \Omega$, a surface across which $\log\mathcal{H}^k$ jumps more than some threshold τ_0. Segment the domain Ω using $\hat{J}_0$ (i.e., find the connected components of $\Omega \setminus \hat{J}_0$), giving subsets $(\hat{\Omega}_i^0)_{i=1}^I$, an estimate of the regions where $\Gamma\mu$ is constant.

(2) In all $\hat{\Omega}_i^0$, search for jumps in $\log|\nabla\mathcal{H}^k|$ that are bigger than threshold τ_1, obtaining sets $\hat{J}_1^i \subset \hat{\Omega}_i^0$. Take $\hat{J}_1 = \bigcup_i \hat{J}_1^i \cup \hat{J}_0$ and segment Ω using $\hat{J}_1$ to get $(\hat{\Omega}_i^1)_{i=1}^I$, an estimate for the regions where $\Gamma\mu$ and D are constant.

(3) In all $\hat{\Omega}_i^1$, search for jump sets $\hat{J}_2^n \subset \hat{\Omega}_n^1$ of $|\log\Delta\mathcal{H}^k - \log\mathcal{H}^k|$, with values above lower threshold τ_2. We get $\hat{J}_2 = \bigcup_n \hat{J}_2^i \cup \hat{J}_1$, our estimate for $J(\Gamma\mu)$ Finally, by segmenting Ω using $\hat{J}_2$ we get $(\hat{\Omega}_m)_{m=1}^M$, an estimate for the regions where $\Gamma\mu, D, \frac{\mu}{D}$ (and thus also parameters μ, D, Γ) are constant.

We can take advantage of multiple measurements $(\mathcal{H}^k)_{k=1}^K$ (with different illuminations) by detecting edges separately for all $\mathcal{H}^k$ (and their derivatives) and joining the edge sets prior to segmentation in each step (1)-(3), or simpler, by averaging the input data for edge detection in each steps (1)-(3) (we implemented the second strategy). Using multiple measurements can be vital to counter locally missing contrast due to failure of condition (2.3.5) or close to extremal points of $\mathcal{H}$.

For the actual jump detection, we use *Canny edge detection* in differential form as proposed by Lindeberg (cf. [39] and [91]). See Appendix 2.8.2 for a short description of the method.

2.4.2. Estimating optical parameters

In the second stage of the reconstruction process, we want to estimate μ, D, Γ from photoacoustic data $(\mathcal{H}^k)_{k=1}^K$ (sampled on a regular grid) given an estimate of the sets $(\Omega_m)_{m=1}^M$ (from the previous section) and reference values, for which we choose (μ_1, D_1, Γ_1) (without loss of generality). For simplicity, we first explain the procedure for a single measurement $\mathcal{H}$.

In the proof of Proposition 2, evaluations of $\mathcal{H}_m$,$\nabla\mathcal{H}_m \cdot \nu$ and $\Delta\mathcal{H}_m$ at isolated points were sufficient to obtain all parameters. In the presence of noise and discretization error it is, however, better to use all the jump information available. Rather than calculating μ_m, D_m, Γ_m in an arbitrary order using equations (2.3.7)-(2.3.10) we use a least-squares fitting method to calculate $\Gamma\mu$, $\frac{D}{\Gamma\mu}$, $\frac{\mu}{D}$ in all Ω_m simultaneously.

Since the data $\mathcal{H}$ contains noise and is only known on a grid, we can only calculate the values of $\mathcal{H}_m$ (whose values may not be known precisely on interfaces), $\nabla\mathcal{H}_m \cdot \nu$ and $\Delta\mathcal{H}_m$ up to some error. For $m = 1, \dots, M$, $y \in \partial\Omega_m$, $z \in \Omega_m$ and $x \in \partial\Omega_m$ with $|\nabla\mathcal{H}_m(x) \cdot \nu(x)| > 0$ let h_m, g_m, l_m be the approximations

$$\begin{aligned} h_m(y) &\approx \log \mathcal{H}_m(y) \\ g_m(x) &\approx \log |\nabla\mathcal{H}_m(x) \cdot \nu(x)| \\ l_m(z) &\approx \log\left(\frac{\Delta\mathcal{H}_m(z)}{\mathcal{H}_m(z)}\right). \end{aligned} \tag{2.4.1}$$

From (2.3.7) and (2.3.8), we get on I_{mn}

$$\log(\Gamma_m\mu_m) - \log(\Gamma_n\mu_n) = \log(\mathcal{H}_m) - \log(\mathcal{H}_n) = h_m - h_n + \epsilon_1 \tag{2.4.2}$$

and

$$\begin{aligned} \log\left(\frac{D_m}{\Gamma_m\mu_m}\right) - \log\left(\frac{D_n}{\Gamma_n\mu_n}\right) &= \log|\nabla\mathcal{H}_n \cdot \nu| - \log|\nabla\mathcal{H}_m \cdot \nu| \\ &= g_n - g_m + \epsilon_2, \end{aligned} \tag{2.4.3}$$

with ϵ_1, ϵ_2 denoting error terms. Now, we can estimate

$$\hat{a}_m \approx \log(\Gamma_m\mu_m), \quad \hat{b}_m \approx \log\left(\frac{D_m}{\Gamma_m\mu_m}\right)$$

for $m > 2$ (a_1, b_1 can be calculated from the reference values) by choosing values which minimize the L^2-norm of the error terms ϵ_1 and ϵ_2 over all interfaces, that is, by solving the least squares problems

$$\begin{aligned} (\hat{a}_2, \dots, \hat{a}_M) &= \arg\min_{a_2,\dots,a_M} \sum_{\substack{n,k=1 \\ k>n}}^{M} \|a_k - a_n + h_n - h_k\|^2_{L^2(I_{nk})} \\ (\hat{b}_2, \dots, \hat{b}_M) &= \arg\min_{a_2,\dots,a_M} \sum_{\substack{n,k=1 \\ k>n}}^{M} \|b_k - b_n - g_n + g_k\|^2_{L^2(\tilde{I}_{nk})}, \end{aligned} \tag{2.4.4}$$

In the second least squares problem, we restrict the calculation to $\tilde{I}_{nk}$, a subset of I_{nk} where g_n, g_k are below some bound (i.e., where $|\mathcal{H}_n \cdot \nu|$ and $|\mathcal{H}_k \cdot \nu|$ are not zero).

A simple calculation shows that the optimizers $\hat{a}, \hat{b}$ satisfy for $2 \le m \le M$

$$\begin{aligned} \sum_{k\neq m} (\hat{a}_m - \hat{a}_k)\mathcal{A}(I_{mk}) &= \sum_{k\neq n} \int_{I_{mk}} h_m - h_k \, dS \\ \sum_{k\neq m} (\hat{b}_m - \hat{b}_k)\mathcal{A}(\tilde{I}_{mk}) &= \sum_{k\neq n} \int_{\tilde{I}_{mk}} g_k - g_m \, dS, \end{aligned} \tag{2.4.5}$$

where $\mathcal{A}(I_{nk})$ denotes the area of the interface $\partial\Omega_m \cap \partial\Omega_n$. Since the corresponding system matrices are irreducibly diagonally dominant, the optimizers $\hat{a}, \hat{b}$ are unique (see, e.g., [70, Theorem 6.2.27]).

In (2.4.5), one can see that in the special case where Ω_1 is the background and $\Omega_2, \ldots, \Omega_M$ are inclusions with no shared boundaries, our approach is equivalent to adding to $\log(\Gamma_1\mu_1)$ (respectively $\log(\frac{D_1}{\Gamma_1\mu_1})$) the estimated jump values $h_k - h_1$ (respectively $g_1 - g_k$) averaged over $\partial\Omega_k$.

Now, using (2.3.8) and (2.4.1), we have in $\Omega_m,\ m = 1, \ldots, M$

$$\log\left(\frac{\mu_m}{D_m}\right) = \log\left(\frac{\Delta\mathcal{H}_m}{\mathcal{H}_m}\right) = l_m + \epsilon_3 \tag{2.4.6}$$

for some error term ϵ. As before, we can estimate

$$\hat{c} = \log\left(\frac{\mu}{D}\right)$$

by minimizing the error term ϵ_3. We obtain for $m = 1, \ldots, M$

$$\hat{c}_m = \arg\min_c \|c - l_m\|^2_{L^2(\Omega_m)} = \frac{1}{\mathcal{V}(\Omega_m)} \int_{\Omega_m} l_m \, dx, \tag{2.4.7}$$

where $\mathcal{V}(\Omega_m)$ denotes the volume of Ω_m, i.e., we take the mean of l_m in Ω_m. Finally, from $\hat{a}, \hat{b}, \hat{c}$, we can calculate $\hat{\mu}, \hat{D}, \hat{\Gamma}$ with (2.3.10).

The use of multiple measurements simply amounts to an additional summation in (2.4.5) and (2.4.7), which corresponds to minimizing over the sum of all measurements.

2.4.3. Implementation

We implemented the ideas presented in the last sections in *MATLAB*. The, possibly noisy, photoacoustic pressure data $(\mathcal{H}^k)_{k=1}^K$ is given sampled on a regular 3D-grid with sufficiently high resolution.

Following the scheme presented in 2.4.1, we first estimate subregions $(\hat{\Omega}_m)_{m=1}^M$ where μ, D, Γ are constant by using computational edge detection and then segmenting Ω using the obtained jump sets.

To detect jumps we use differential *Canny edge detection* (see Appendix 2.8.2 for details). The derivatives are estimated via finite differences (after low-pass filtering with a Gaussian kernel). We obtain jump surfaces with sub-voxel resolution in the form of a triangular mesh. For segmentation, we applied the *MATLAB* image processing toolbox function *bwconncomp*, which works on a voxel level (small holes in the jump sets, for instance at corners, can be closed up by increasing the thickness of the voxelized surfaces).

Given the jump surfaces and estimated regions $(\hat{\Omega}_m)_{m=1}^M$, in order to approximate $h_m \approx \log \mathcal{H}_m$ and $g_m \approx |\nabla \mathcal{H}_m \cdot \nu|$ (cf. (2.4.1)), we fit for every triangular element e (with incenter y) of the surface a log-linear function f_m^e to the data $\mathcal{H}_m$ at nearby grid points (using a Gaussian weight function that gives grid points closer to y a larger weight). By taking $h_m^e = \log f_m^e(y)$ and $g_m^e = \log |\nabla f_m^e(y) \cdot \nu(y)|$ at y, we get approximations h_m and g_m that are piecewise constant on the surface elements e. We obtain $\hat{a} \approx \log(\Gamma\mu)$ and $\hat{b} \approx \log\left(\frac{D}{\Gamma\mu}\right)$ by solving (2.4.5).

Similarly, we use (2.4.7) to estimate $\hat{c} \approx \log\left(\frac{\mu}{D}\right)$. Here, we locally (at grid points z inside the estimated regions $\hat{\Omega}_m$) fit quadratic functions q_m^z to the data H_m, calculate $l_m = \log\left|\frac{\Delta q_m^z}{\mathcal{H}_m(z)}\right| \approx \log\left(\frac{\Delta \mathcal{H}_m}{\mathcal{H}_m}\right)$ and average over z to obtain $\hat{c}$ (since the fitting procedure is computationally intensive, this calculation is only performed on a random sample of the grid points, replacing the total average with the sample average).

2.5. Numerical examples

In this section, we apply the numerical method described in the last section to simulated data. We start with a simple example using FEM-generated data with no added noise.

In the second example, we work with Monte Carlo generated data with added noise. The Monte Carlo method for photon transfer in random media (which is physically more accurate than the diffusion approximation) converges to solutions of the *radiative transfer equation* and thus satisfies our model (2.1.1) only approximately (see, e.g., [117] for details).

2.5.1. Example using FEM-generated data

In the first example, we simulated a single photoacoustic measurement (using one illumination pattern only) directly in the diffusion approximation, with no added noise.

We placed, centered at $z = 5$, four spherical inhomogeneities (cf. Figure 2.1) into a cubical grid $(x, y, z) \in [0, 20] \times [0, 10] \times [0, 10]$ with resolution $320 \times 160 \times 160$. The fluence u is calculated by numerically solving the PDE (2.1.1) with homogeneous Dirichlet boundary conditions (simulating a uniform illumination). For this purpose, we take a self-written *MATLAB* finite element solver (that splits the grid into a tetrahedral mesh and then uses linear basis elements). To get simulated initial pressure data $\mathcal{H}$, we re-sampled u at the grid centerpoints and built $\mathcal{H} = \Gamma\mu u$ by multiplication with $\Gamma\mu$ (see Figure 2.2).

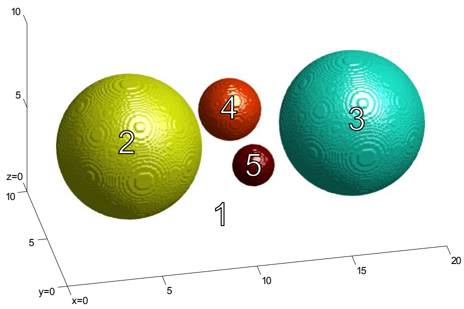

(a) Inhomogenities

	μ	D	Γ
Region 1	0.1	1	1
Region 2	0.2	1	1
Region 3	0.1	0.25	1
Region 4	0.01	1	10
Region 5	1	10	0.01

(b) Material properties

Figure 2.1.: Simulation setup. Spherical inhomogeneities viewed from top left (a) and their material properties (b).

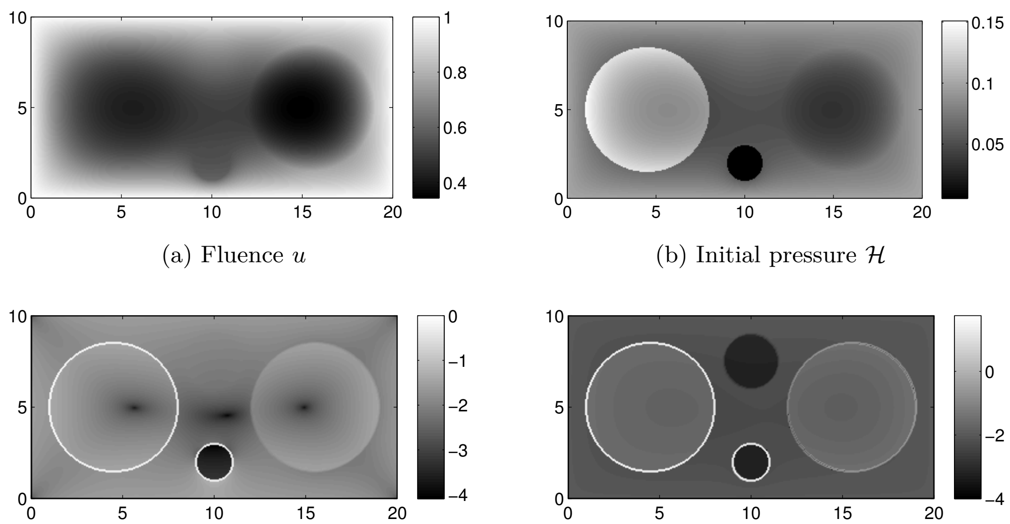

(a) Fluence u

(b) Initial pressure $\mathcal{H}$

(c) $\log_{10}|\nabla\mathcal{H}|$

(d) $\log_{10}|\Delta\mathcal{H}|$

Figure 2.2.: FEM-simulated fluence, photoacoustic initial pressure and derivatives. The fluence is chosen to be uniform at the boundary. Derivatives are calculated by finite differences. All images are plane cuts at $z = 5$.

In Figure 2.2, one can see how the inhomogeneities affect the data $\mathcal{H}$ (cf. Proposition 1). Spheres 1 and 4 have contrast in $\Gamma\mu$ with respect to the background, so their boundaries are are visible in $\mathcal{H}$. Sphere 2 displays contrast in D, but not in $\Gamma\mu$, its interface with the background hence can be seen in $|\nabla\mathcal{H}|$. Since in this particular example, the field ∇u is never parallel to the sphere's boundary, the whole boundary is visible. Sphere 3 has the same $\Gamma\mu$ and D as the background, so it's only visible in $|\Delta\mathcal{H}|$.

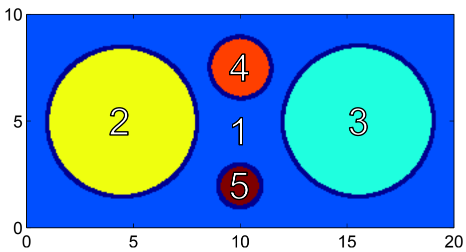

(a) Estimated segmentation and jumps

	$\hat{\mu}$	$\hat{D}$	$\hat{\Gamma}$
Region 1	0.0995 (0.5%)	1.0000 (0%)	1.0000 (0%)
Region 2	0.1977 (1.1%)	0.9880 (1.2%)	1.0043 (0.4%)
Region 3	0.1105 (10.5%)	0.2759 (10.4%)	0.9072 (9.3%)
Region 4	0.0097 (2.8%)	0.9723 (2.8%)	10.2429 (2.4%)
Region 5	0.6238 (37.6%)	6.2361 (37.6%)	0.0158 (58.4%)

(b) Parameter estimates and relative errors

Figure 2.3.: Estimated jumps and regions in a plane cut at $z = 5$ (a), estimated parameters and their relative errors (b).

Figure 2.3 shows the reconstruction results. As reference values, we used the values of D and Γ in the background (Region 1). All parameter discontinuities were recovered. Without noise, by far the biggest accuracy bottleneck is the estimation of jumps in D from the normal components of $\nabla\mathcal{H}$, in particular for smaller structures (with respect to the resolution). The estimation of $\mu\Gamma$ and $\frac{\mu}{D}$ works almost perfectly for this type of data.

2.5.2. Example using Monte-Carlo-generated data

For the second numerical example, we used *MMC*, an open source 3D Monte-Carlo photon transfer simulator by Qianqian Fang (see [57] for details), to simulate photoacoustic measurements.

We again placed four inhomogeneities, centered at $z = 5$, into a homogeneous background cubic grid $(x, y, z) \in [0, 10] \times [0, 10] \times [0, 10]$ with resolution $150 \times 150 \times 150$ (cf. Figure 2.4). Note that two of the structures touch (Regions 2 and 3). We deliberately chose the material parameters such that there is always enough contrast in $\Gamma\mu$ and D so that edge detection in $\frac{\Delta\mathcal{H}}{\mathcal{H}}$ is not necessary (this proved to be very tricky in the presence of noise since it uses second order differences). Using *MMC*, we calculated fluences u^k, $k = 1, \dots, 6$ for 6, for multiple sources (placed in the center of each of the cube's faces). We again re-sampled u at the grid centerpoints, built initial pressure data $\mathcal{H}^k = \Gamma\mu u^k$ (by multiplication with $\Gamma\mu$) and added 5% multiplicative Gaussian noise (which corresponds to a constant signal-to-noise ratio of about 26 dB).

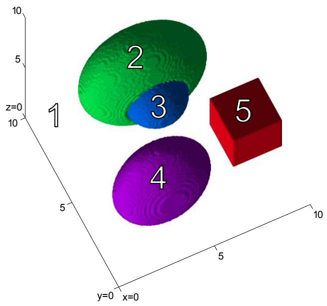

(a) Inhomogenities

	μ	D	Γ
Region 1	0.01	0.166	1
Region 2	0.01	0.056	1
Region 3	0.01	0.166	1.2
Region 4	0.02	0.538	0.5
Region 5	0.006	0.111	0.8

(b) Material properties

Figure 2.4.: Simulation setup. Inhomogeneities viewed from the top right (a) and their material properties (b).

Figure 2.5 shows a Monte-Carlo-simulated fluence u^1 and initial pressure H^1 (for which the light source at the top of the $z = 5$ plane cut). Regions 3 and 5 are are visible in $\log \mathcal{H}^1$ due to contrast in $\Gamma\mu$. Regions 2 and 4 appear in $\log |\nabla\mathcal{H}^1|$. At some parts of the regions boundaries, the ∇u is parallel to the boundary, which leads to vanishing contrast. Taking the mean of $\log |\nabla\mathcal{H}^k|$ (over the 6 sources), the whole boundary is becomes visible.

Figure 2.6 shows the reconstruction results. As reference values, we again used the values of D and Γ in the background. All parameter discontinuities were recovered. As before, errors in the estimation of jumps in D from the normal components of $\nabla\mathcal{H}$ were the most significant.

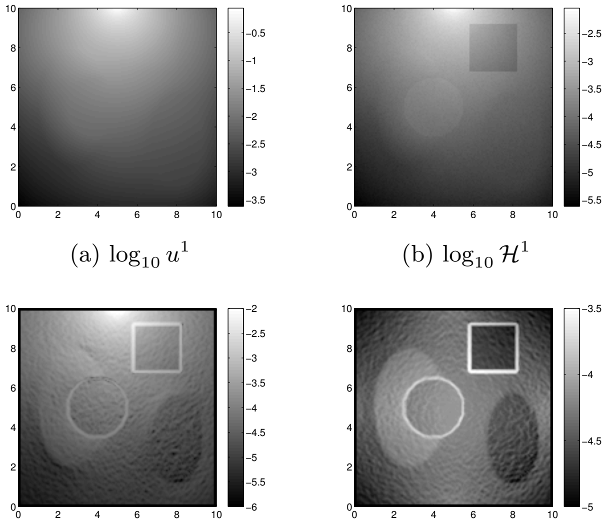

(a) $\log_{10} u^1$

(b) $\log_{10} \mathcal{H}^1$

(c) $\log_{10} |\nabla \mathcal{H}^1|$

(d) $\frac{1}{6} \sum_k \log_{10} |\nabla \mathcal{H}^k|$

Figure 2.5.: MMC-simulated fluence, photoacoustic initial pressure (with noise) and its derivatives. The light source which generated u_1 is placed at the top of the image. Derivatives are calculated by convolution with a Gaussian (with standard deviation of 1 pixel) followed by finite differences. All images are plane cuts at $z = 5$.

	$\hat{\boldsymbol{\mu}}$	$\hat{\boldsymbol{D}}$	$\hat{\boldsymbol{\Gamma}}$
Region 1	0.012 (19.8%)	0.166 (0%)	1.0000 (0%)
Region 2	0.014 (41.2%)	0.077 (39.2%)	0.839 (16.1%)
Region 3	0.011 (11.5%)	0.190 (14.7%)	1.284 (7%)
Region 4	0.023 (16.2%)	0.447 (16.9%)	0.511 (2.1%)
Region 5	0.007 (19.2%)	0.128 (15.5%)	0.806 (0.8%)

Figure 2.6.: Parameter estimates and relative errors.

2.6. Conclusion

Our theoretical analysis shows that in many cases (e.g., if enough measurements such that (2.3.12) holds in the region of interest are available), unique reconstruction of piecewise constant μ, D, Γ from photoacoustic measurements at a single wavelength is possible. Our numerical implementation of the analytical reconstruction procedure works with reasonable accuracy, even with Monte Carlo generated data (which satisfies the diffusion approximation, which we use for reconstruction, only approximately). Our numerical method, however, requires data with very high resolution and large parameter contrast. In addition, due to the fact that we use second derivatives of the data, our method is very sensitive to noise, so use with real data might turn out to be challenging.

2.7. Acknowledgements

This work has been supported by the Austrian Science Fund (FWF) within the national research network Photoacoustic Imaging in Biology and Medicine (project S10505-N20) and by the IK I059-N funded by the University of Vienna.

2.8. Appendix

2.8.1. Derivation of transmission formulation

In this section (following the proof in [17]), we prove that under some regularity assumptions, a function u is a weak solution of

$$-\operatorname{div}(D\nabla u) + \mu u = 0 \quad \text{in } \Omega \tag{2.8.1}$$

with piecewise smooth parameters μ, D if and only if

(1) u a classical solution in regions where the parameters are smooth,

(2) u is continuous,

(3) the transmission condition (2.8.4) holds at the jumps.

Let $\Omega \subset \mathbb{R}^n$ and $(\Omega_m)_{m=1}^M$ be piecewise-C^1 domains such that $\overline{\Omega} = \bigcup_{m=1}^M \overline{\Omega}_m$.

Denote by T the part of the subregion boundaries that is C^1 and in the closure of at most two subregions. We require that the partition is chosen such $\mathcal{H}^{n-1}(\bigcup_{m=1}^M \partial\Omega_m \setminus T) = 0$, i.e., the set junctions where more than three subregions meet or the boundary is not C^1 has zero surface measure.

Furthermore, let the parameters $\mu, D > 0$ be bounded and piecewise smooth, i.e., of the form

$$\mu = \sum_{m=1}^{M} \mu_m 1_{\Omega_m}, \quad D = \sum_{m=1}^{M} D_m 1_{\Omega_m}$$

with $\mu_m, D_m \in C^\infty(\overline{\Omega}_m)$. For a corresponding solution u of (2.8.1), let

$$u_m := u|_{\Omega_m}, \; m = 1, \ldots, M.$$

Lemma 1.
Let u be a weak solution of (2.8.1). Furthermore, let u_m, $m = 1, \ldots, M$ satisfy

$$u_m \in C^1(\overline{\Omega}_m \cap B) \quad \text{for all } B \text{ with } B \cap T = \emptyset. \tag{2.8.2}$$

Then $u \in C^\alpha(\Omega)$ for some $\alpha > 0$ and $u_m \in C^\infty(\Omega_m)$. Additionally, the restrictions u_m satisfy

$$-\operatorname{div}(D_m \nabla u_m) + \mu_m u_m = 0 \quad \text{in } \Omega_m \tag{2.8.3}$$

and, almost everywhere on interfaces $I_{mn} = \partial\Omega_m \cap \partial\Omega_n$,

$$D_m \nabla u_m \cdot \nu = D_n \nabla u_n \cdot \nu \quad \text{(for any interface normal } \nu\text{)}. \tag{2.8.4}$$

Proof. A weak solution u of (2.8.1) satisfies $u \in H^1(\Omega)$ and

$$\int_\Omega D\nabla u \cdot \nabla\phi + \mu u \phi \, dx = 0 \text{ for all } \phi \in C_c^\infty(\Omega).$$

Since the equation is elliptic, we have $u_m \in C^\infty(\Omega_m)$ by interior regularity [63, Corollary 8.11] and hence, from integration by parts, $\int_\Omega -\operatorname{div}(D_m \nabla u_m)\phi + \mu_m u_m \phi \, dx = 0$ for all $\phi \in C_c^\infty(\Omega_m)$, which shows that (2.8.3) holds classically in Ω_m, $m = 1, \ldots, M$.

From De Giorgi-Nash-Moser theorem [63, Theorem 8.22] we get $u \in C^\alpha(\overline{\Omega})$ for some $\alpha > 0$.

Next, let $I_{mn} = \partial\Omega_m \cap \partial\Omega_n$ be the interface between some Ω_m and Ω_n. For almost all $x \in I_{mn}$ (those in T), there exists an open ball $B \Subset \Omega$ such that $x \in B = B_m \cup B_n = (\Omega_m \cap B) \cup (\Omega_n \cap B)$ (by the restriction on the partition).

Using integration by parts and (2.8.3) we get for all $\phi \in C_c^\infty(B) \subset C_c^\infty(\Omega)$

$$\begin{aligned}
0 &= \int_\Omega D\nabla u \cdot \nabla\phi + \mu u \phi \, dx \\
&= \int_{\Omega_m} D_m \nabla u_m \cdot \nabla\phi + \mu_m u_m \phi \, dx + \int_{\Omega_n} D_n \nabla u_n \cdot \nabla\phi + \mu_n u_n \phi \, dx \\
&= \int_{\partial B_m} (D_m \nabla u_m \cdot \nu)\phi + \int_{\partial B_n} (D_n \nabla u_n \cdot \nu)\phi \, dS \\
&= \int_{I_{mn} \cap B} (D_m \nabla u_m \cdot \nu - D_n \nabla u_n \cdot \nu)\phi \, dS.
\end{aligned}$$

The transmission condition (2.8.4) follows since $\nabla u_m, \nabla u_n \in C(I_{mn} \cap B)$ (by assumption (2.8.2)).

□

For certain partition geometries, weak solutions of (2.8.1) always satisfy condition (2.8.2). For instance, Li and Nirenberg [90, Proposition 1.4] showed that if $(\Omega_m)_{m=2}^M$ are inclusions with smooth boundaries (which may also touch in some points) and background Ω_1, one gets $u_m \in C^\infty(\overline{\Omega}_m)$.

For sufficiently regular u_m (e.g., in the setting just described) we can also derive the converse of Lemma 1:

Lemma 2. *Let $u_m := u|_{\Omega_m} \in C^2(\overline{\Omega}_m)$, $m = 1, \dots, M$, satisfy*

$$-\operatorname{div}(D_m \nabla u_m) + \mu_m u_m = 0 \quad \text{in } \Omega_m \tag{2.8.5}$$

and, on interfaces $I_{mn} = \partial\Omega_m \cap \partial\Omega_n$ with normal ν,

$$\begin{aligned} u_m &= u_n \\ D_m \nabla u_m \cdot \nu &= D_n \nabla u_n \cdot \nu. \end{aligned} \tag{2.8.6}$$

Then u is a weak solution of (2.8.1).

Proof. To get $u \in H^1(\Omega)$, we first show that the weak gradient of u is given by

$$\nabla u = \sum_{m=1}^{M} \nabla u_m 1_{\Omega_m}. \tag{2.8.7}$$

To see that, note that for all $\phi \in C_c^\infty(\Omega)$

$$-\int_\Omega u \nabla \phi \, dx = -\sum_{m=1}^{M} \int_{\Omega_m} u_m \nabla \phi \, dx = \sum_{m=1}^{M} \left(\int_{\Omega_m} \nabla u_m \phi \, dx - \int_{\partial\Omega_m} u_m \phi \nu \, dS \right).$$

The interior boundary terms cancel out due to $u_m = u_n$, the exterior boundary terms vanish since $\operatorname{supp} \phi \Subset \Omega$), so the weak gradient of u is given by (2.8.7). Hence $u \in H^1(\Omega)$ since

$$\begin{aligned} \|u\|_{H^1(\Omega)}^2 &= \int_\Omega |u|^2 + |\nabla u|^2 \, dx = \sum_{m=1}^{M} \left(\int_{\Omega_m} |u_m|^2 + |\nabla u_m|^2 \, dx \right) \\ &= \sum_{m=1}^{M} \|u_m\|_{H^1(\Omega_m)}^2 \leq C \sum_{m=1}^{M} \|u_m\|_{W^{1,\infty}(\overline{\Omega}_m)}^2 < \infty \end{aligned}$$

Furthermore, using integration by parts, (2.8.5) and (2.8.6) imply

$$\begin{aligned}\int_\Omega D\nabla u\cdot\nabla\phi+\mu u\phi\,dx &= \sum_{m=1}^{M}\int_{\Omega_m} D_m\nabla u_m\cdot\nabla\phi+\mu_m u_m\phi\,dx\\ &= \sum_{m=1}^{M}\int_{\partial\Omega_m} D_m(\nabla u_m\cdot\nu)\phi\,dS=0\end{aligned}$$

for $\phi\in C_c^\infty(\Omega)$ since the boundary terms cancel out due to (2.8.6) and $\operatorname{supp}\phi\Subset\Omega$, so u is a weak solution of (2.8.1). □

2.8.2. Differential Canny edge detection

In differential *Canny edge detection* as proposed by Lindeberg (cf. [91]), one starts from a *scale space* representation $f_\sigma = f * g_\sigma$ of a two-dimensional image $f\colon\mathbb{R}^2\to\mathbb{R}$, where g_σ is a Gaussian kernel with standard deviation σ. Edges at scale σ are then *defined* (with finite resolution, no natural notion of discontinuity exists) as local maxima of the gradient magnitude $|\nabla f_\sigma|$ in gradient direction ∇f_σ. Additionally, it is proposed to additionally maximize a certain functional measuring edge strength in scale space (which allows for automatic scale selection).

We want to use a similar algorithm to find the discontinuities of a three-dimensional function $f\colon\mathbb{R}^3\to\mathbb{R}$ (which will be $\log\mathcal{H}^k$, $\log|\nabla\mathcal{H}^k|$ or $\log|\frac{\Delta\mathcal{H}^k}{\mathcal{H}^k}|$). Jumps of f that are sufficiently big compared its continuous variation (within a grid step) lead to sudden changes of intensity (above some threshold) in the corresponding finite-resolution image. Heuristically, we have a similar situation as in Canny edge detection. That is, jump surfaces approximately correspond to thresholded maxima of $|\nabla f_\sigma|$ in gradient direction, where $f_\sigma = f*g_\sigma$ is the scale-space representation of f for a properly chosen scale σ (for simplicity, we will work at a single, manually chosen scale in this paper).

To estimate the jump set, we thus have to solve for *fixed* σ and $v=\nabla f_\sigma$

$$\begin{aligned}\partial_v|\nabla f_\sigma|^2 &= \sum_{i,j=1}^{3} v_i v_j\,\partial_{x_i x_j} f_\sigma = 0\\ \partial_{vv}|\nabla f_\sigma|^2 &= \sum_{i,j,k=1}^{3} v_i v_j v_k\,\partial_{x_i x_j x_k} f_\sigma > 0.\end{aligned}\tag{2.8.8}$$

For discrete (voxelized) f, the solution manifold can be calculated with sub-voxel resolution. To restrict E, the solution surface of (2.8.8), to parts where the gradient magnitude (and thus also the jump across the surface) is large enough, we perform *hysteresis thresholding*. That is, we first apply a lower threshold ρ_1 to the jump strength $|\nabla f_\sigma|$ to get

$$E_1 = \{x \in E \mid |\nabla f_\sigma(x)| \geq \rho_1\}.$$

Then, we remove all connected components $C \subset E_1$ for which the jump strength is never above a higher threshold ρ_2, so we get our final jump set E_2 with

$$E_2 = \bigcup \{C \subset E_1 \mid C \text{ is connected } \wedge \ \exists x \in C\colon \ |\nabla f_\sigma(x)| \geq \rho_2\}.$$

As a final step, we remove all isolated structures smaller than a certain size (which are usually due to misdetections and too small for further processing).

3. A variational method for quantitative photoacoustic tomography with piecewise constant coefficients

Authors and Contributions. The authors are Elena Beretta, Monika Muszkieta, Wolf Naetar and Otmar Scherzer. The development of this article was a gradual, cooperative process. The author list is alphabetical, every author made significant contributions to the paper.

Publication Status. Accepted for publication in *Variational Methods in Imaging and Geometric Control*, Radon Series on Computational and Applied Mathematics, Walter de Gruyter GmbH & Co. KG, Berlin, 2016. The version contained in this Chapter is a preprint available at http://arxiv.org/abs/1509.04982.

A variational method for quantitative photoacoustic tomography with piecewise constant coefficients

E. Beretta (elena.beretta@polimi.it)[1]
M. Muszkieta (monika.muszkieta@pwr.edu.pl)[2]
W. Naetar (wolf.naetar@univie.ac.at)[3]
O. Scherzer (otmar.scherzer@univie.ac.at)[3,4]

[1]Dipartimento di Matematica
Politecnico di Milano
Via Edoardo Bonardi, 20133 Milan, Italy

[2]Faculty of Pure and Applied Mathematics
Wroclaw University of Technology
Wyb. Wyspianskiego 27, PL-50-370 Wroclaw, Poland

[3]Computational Science Center
University of Vienna
Oskar Morgenstern-Platz 1, A-1090 Vienna, Austria

[4]Radon Institute of Computational and Applied Mathematics
Austrian Academy of Sciences
Altenbergerstr. 69, A-4040 Linz, Austria

October 5, 2015

We consider the inverse problem of determining spatially heterogeneous *absorption* and *diffusion* coefficients $\mu(x), D(x)$, from *a single measurement* of the *absorbed energy* $\mathcal{E}(x) = \mu(x)u(x)$, where u satisfies the elliptic partial differential equation

$$-\nabla \cdot (D(x)\nabla u(x)) + \mu(x)u(x) = 0 \quad \text{in } \Omega \subset \mathbb{R}^N.$$

This problem, which is central in *quantitative photoacoustic tomography*, is in general ill-posed since it admits an infinite number of solution pairs. Here, we show that when the coefficients μ, D are known to be piecewise constant functions, a unique solution can be obtained. For the numerical determination of μ, D, we suggest a variational method based on an *Ambrosio-Tortorelli approximation* of a *Mumford-Shah-like functional*, which we implemented numerically and tested on simulated two-dimensional data.

Keywords. Quantitative photoacoustic tomography, mathematical imaging, inverse problems, Mumford-Shah functional

AMS subject classifications. 35R25, 35R30, 65J22, 65K10, 92C55

3.1. Quantitative photoacoustic tomography

3.1.1. Introduction

Photoacoustic tomography (PAT) is a medical imaging technique that combines electromagnetic excitation (in the visible spectrum) with ultrasound measurements. In a photoacoustic experiment, a translucent sample is illuminated by a laser pulse with wavelength λ (which we assume to be fixed in this article). The absorbed optical energy leads to thermal expansion, generating an ultrasound pressure wave $p(x,t)$ that can be measured outside the sample.

Since the pulses used in PAT are very short, the complete energy is deposited almost instantaneously compared to travel times of acoustic waves, and the pressure wave p can be assumed to have been generated by an *initial pressure* $\mathcal{H}(x)$, that is, it satisfies the wave equation

$$\begin{aligned} \partial_{tt}p(x,t) - c^2(x)\Delta p(x,t) &= 0 \\ \partial_t p(x,0) &= 0 \\ p(x,0) &= \mathcal{H}(x) \end{aligned}$$

and $p|_{\mathcal{M}}$, where $\mathcal{M}$ denotes a *measurement surface*, can be obtained from ultrasound measurements [46, 47, 83, 117].

By solving an *inverse problem for the wave equation* (see, e.g, [83] for a review of inversion techniques), these ultrasound measurements can be used to estimate the *initial pressure* $\mathcal{H}(x)$. Since

$$\mathcal{H}(x) = \Gamma(x)\,\mathcal{E}(x) = \Gamma(x)\mu(x)u(x), \tag{3.1.1}$$

that is, $\mathcal{H}(x)$ is proportional to the *absorbed energy* $\mathcal{E}(x)$, which is in turn proportional to the *optical absorption coefficient* $\mu(x)$ at the applied wavelength λ and the local fluence $u(x)$ (the time-integrated laser power received at x), the initial pressure visualizes contrast in μ. The constant of proportionality $\Gamma(x)$ is called *Grüneisen coefficient* (or *PA efficiency* since it describes the efficiency of conversion from absorbed energy to acoustic signal) [46, 47].

In *quantitative photoacoustic tomography* (qPAT), the goal is to apply PAT to determine (inhomogeneous) optical material properties of the sample (which are of diagnostic interest). To do so, an additional non-linear *inverse problem for light transport* has to be solved, since the fluence $u(x)$ is inhomogeneous and itself dependent on the optical properties of the sample [46, 47].

While it is also possible to attack the acoustic and optical inverse problems simultaneously (see, e.g., [37, 65]), here, we assume that the acoustic part of the problem has been solved successfully, i.e., that (possibly noisy) data $\mathcal{H}^\delta \approx \mathcal{H}$ (with δ signifying the noise level) is available.

In this article, we utilize the *diffusion approximation* (which is valid in highly scattering media [46, 117]) of the *radiative transfer equation* to model the fluence distribution. It is, however, also possible to use a radiative transfer model for qPAT (see [50, 98, 104, 115, 123]), albeit at the cost of increased computational and analytical complexity.

The diffusion model (in a Lipschitz domain $\Omega \subset \mathbb{R}^N$) is given by

$$\begin{aligned} -\nabla \cdot (D(x)\nabla u(x)) + \mu(x)u(x) = 0 \quad \text{in } \Omega \\ u(x)|_{\partial\Omega} = g(x). \end{aligned} \tag{3.1.2}$$

The parameter D is called *diffusion coefficient*. The Dirichlet boundary data g (which we assume to be continuous and known in this article) describes the illumination pattern. Note that this is a time-independent model, again due to the fact that energy is deposited almost instantaneously compared to time scales of the acoustic system.

The difficulty of the inverse problem varies depending on which parameters of the model are assumed to be known. We present three inverse problems often considered in the literature. The hardest one is:

$$\text{Determine } (\mu, D, \Gamma) \text{ from measurements of } \mathcal{H}^\delta. \tag{P3}$$

Bal and Ren showed in [28] that for arbitrary coefficients $\mu, D, \Gamma \in W^{1,\infty}(\Omega)$, this problem is unsolvable, even if multiple measurements of $\mathcal{H}$ (with different known boundary illumination patterns g) are available.

In [94], the authors showed that with a restriction to *piecewise constant parameters*, unique reconstruction of all three unknown parameters μ, D, Γ from multiple measurements is possible (under a condition on the directions of ∇u_k, where u_k is the fluence of the kth illumination pattern). Furthermore, an analytical reconstruction procedure was suggested and implemented numerically, which, unfortunately, is relatively sensitive to noise.

Alberti and Ammari [4] also established a unique reconstruction result, based on *morphological component analysis* (a sparsity approach), in a slightly more general setting (which assumes different degrees of smoothness of the coefficients and the fluence). They also provide numerical reconstructions, which were, however, not tested for noise sensitivity in the case of (P3).

To simplify the problem, it is often assumed that the Grüneisen coefficient Γ is known or constant, which implies that the absorbed energy can be estimated with $\mathcal{E}^\delta = \frac{\mathcal{H}^\delta}{\Gamma} \approx \mathcal{E}$ (with δ again denoting the noise level). It remains to solve

$$\text{Determine } (\mu, D) \text{ from measurements of } \mathcal{E}^\delta. \tag{P2}$$

If only a single measurement of $\mathcal{E}^\delta$ is given, this inverse problem is also ill-posed (since it has infinitely many solutions pairs, see [44, 94, 106]).

However, in [4], the authors were able to recover μ (independently of the light transfer model used) from a single measurement of $\mathcal{E}$ (again by use of a *sparsity method*, assuming different degrees of smoothness of the coefficients and the fluence).

In [28, 32] it was shown that this problem is uniquely solvable if two measurements of $\mathcal{E}$ (corresponding to well-chosen boundary illuminations g_1, g_2) are available. Numerically, this multi-illumination case was treated in [28, 61, 101, 106, 115, 127], using a multitude of different techniques, see also the review paper by Cox et al. [46].

The simplest case works under the assumption that the diffusion coefficient D is also known:

$$\text{Determine } \mu \text{ from measurements of } \mathcal{E}^\delta. \tag{P1}$$

This inverse problem has a unique solution even for a single measurement, which can be seen by substituting $\mu u = \mathcal{E}^\delta$ in (3.1.2), providing the possibility to solve for u [34]. For other (numerical) approaches, cf. [46]. To the authors knowledge, this simplified problem is the only case for which practical viability (with experimental data) has been established both for phantoms [124] and biological samples [109, 110].

3.1.2. Contributions of this article

In this article, we consider the problem (P2) using a *single measurement* for our reconstructions, a problem that is in general ill-posed. Similar to [94] (which treats (P3) with multiple measurements), a restriction to piecewise constant μ, D also proves to be useful for this problem. In fact, as shown in Section 3.2, when the parameters μ, D are piecewise constant functions (and noise-free data is given), the inverse problem (P2) can be solved uniquely, without any further assumptions.

In Section 3.3, we present a variational model for the reconstruction of piecewise constant μ, D from noisy data $\mathcal{E}^\delta$ based on the *Ambrosio-Tortorelli approximation* of a *Mumford-Shah-like functional*. Compared to the two-step reconstruction process presented in [94] (which was introduced for (P3), but is applicable for (P2)), which first detects the regions where the parameters are constant, then reconstructs the parameter values from jumps of the data and its derivatives, this variational approach is much more robust with respect to noise. This is mainly due to the fact that the numerical approach presented in [94] requires almost perfect jump detection in the second derivatives of $\mathcal{E}^\delta$ to get reasonable estimates of μ, D (since the jumps have to form a full partition of the domain Ω), which is highly challenging in the presence of significant amounts of noise. This is not the case for the variational method presented here.

Finally, a description of our implementation and numerical results can be found in Section 3.4.

3.2. Recovery of piecewise constant coefficients

In this Section we show that piecewise constant parameters μ, D can be recovered uniquely from a single measurement of the absorbed energy $\mathcal{E}(\mu, D)$.

In the following, let $(\Omega_m)_{m=1}^M$ be a partition of $\Omega \subset \mathbb{R}^N$ into open sets and μ, D piecewise constant on $(\Omega_m)_{m=1}^M$, that is, for Ω_m open and $\mu_m, D_m \in \mathbb{R}^+$

$$\overline{\Omega} = \bigcup_{m=1}^M \overline{\Omega}_m, \quad \mu = \sum_{m=1}^M \mu_m 1_{\Omega_m}, \quad D = \sum_{m=1}^M D_m 1_{\Omega_m}. \tag{3.2.1}$$

Furthermore, for $k \in \mathbb{N}$, denote by

$$J_k(f) = \Omega \setminus \bigcup \{B \subset \Omega \mid B \text{ is open and } f \in C^k(B)\}$$

the discontinuities of a function $f \in L^\infty(\Omega)$ and its derivatives up to k-th order.

First, we show that coefficient discontinuities can be recovered from the data $\mathcal{E}$.

Proposition 4. *Let μ, D be of the form (3.2.1) and $\mathcal{E} = \mathcal{E}(\mu, D)$ satisfy (3.1.1), (3.1.2) weakly. Then we have*

$$J_0(\mu) \cup J_0(D) = J_2(\mathcal{E}). \tag{3.2.2}$$

Proof. First, take an arbitrary open ball B with $B \cap (J_0(\mu) \cup J_0(D)) = \emptyset$ and notice that, by interior elliptic regularity, $u \in C^\infty(B)$ and hence also $\mathcal{E} \in C^\infty(B)$. It follows that

$$J_0(\mu) \cup J_0(D) \supset J_2(\mathcal{E}).$$

By the De Giorgi-Nash-Moser theorem [63, Theorem 8.22], we have $u \in C^0(\overline{\Omega})$, so

$$J_0(\mu) = J_0(\mathcal{E}). \tag{3.2.3}$$

Finally, as $u \in C^\infty(\Omega_m)$, $m = 1, \dots, M$, (3.1.2) holds strongly in all Ω_m, and we get

$$\begin{aligned} -D_m \Delta u + \mu_m u &= 0 \quad \text{in } \Omega_m \\ -D_m \Delta \mathcal{E} + \mu_m \mathcal{E} &= 0 \quad \text{in } \Omega_m \end{aligned} \tag{3.2.4}$$

since μ_m, D_m are scalars. Hence, $\Delta \mathcal{E} = \frac{\mu}{D} \mathcal{E} = \frac{\mu^2}{D} u$ in $\bigcup_{m=1}^M \Omega_m$, which shows that $\Delta \mathcal{E}$ cannot be continuous where $\frac{\mu^2}{D}$ jumps (since $u \in C^0(\overline{\Omega})$), hence

$$J_0\left(\frac{\mu^2}{D}\right) \subset J_2(\mathcal{E}).$$

The Proposition follows from $J_0(\mu) \cup J_0\left(\frac{\mu^2}{D}\right) = J_0(\mu) \cup J_0(D)$. □

Remark 1. The proof of Proposition 4 also shows that jumps in μ and D have different effects on the data $\mathcal{E}$. By (3.2.3), the jumps of μ can be recovered from those in $\mathcal{E}$. Jumps of D (not coinciding with jumps of μ) on the other hand, are smoothed in the data and have to be obtained from the derivatives of $\mathcal{E}$. In particular, the discontinuities of $\Delta\,\mathcal{E}$ suffice to find the jumps in D.

Furthermore, note that from discontinuities of $\nabla\,\mathcal{E}$ (or, equivalently, $|\nabla\,\mathcal{E}\,|^2$), one can, in general, only recover the part of the jumps of D where $\nabla u(x)\cdot\nu(x)\neq 0$ (where ν denotes a normal vector to the hyper-surface of discontinuity in D), as ∇u may be continuous across parts of the jump set of D where $\nabla u(x)$ is tangential.

To see this, consider for instance the case of a partition consisting of a homogeneous region Ω_1 with (non-touching) smooth inclusions $\Omega_2,\dots,\Omega_M$. In this case, we have $u\in C^\infty(\overline{\Omega}_m)$ for all $m=1,\dots,M$ (due a result of Li and Nirenberg, see [90]) and the interface conditions

$$D_m\nabla u|_{\Omega_m}\cdot\nu = D_1\nabla u|_{\Omega_1}\cdot\nu,\quad \nabla u|_{\Omega_m}\cdot\tau=\nabla u|_{\Omega_1}\cdot\tau \tag{3.2.5}$$

hold point-wise on $\partial\Omega_m$ for $m=2,\dots,M$, where ν,τ denote vectors normal and tangential to $\partial\Omega_m$ (see, e.g., [94] for a derivation). Now, let

$$\Lambda := \{x\in\bigcup_{m=2}^{M}\partial\Omega_m \mid \nabla u(x)\cdot\nu(x)\neq 0\}.$$

We have $J_0(D)\cap\Lambda\subset J_1(u)$ since, by the interface conditions (3.2.5), ∇u cannot be continuous across $J_0(D)\cap\Lambda$ (it changes length). On the other hand, if we take an open ball $B\subset\Omega_k\cup\Omega_1$ (for some $2\le k\le M$) with $B\cap J_0(D)\cap\Lambda=\emptyset$, we have, again by (3.2.5),

$$\nabla u|_{\Omega_k}=\nabla u|_{\Omega_1}\quad\text{ on }\partial\Omega_k\cap B \tag{3.2.6}$$

since either $D_k=D_1$ or $\nabla u|_{\Omega_k\cap B}\cdot\nu=\nabla u|_{\Omega_1\cap B}\cdot\nu=0$. As we have $u\in C^\infty(\overline{\Omega}_k)$, $u\in C^\infty(\overline{\Omega}_1)$, (3.2.6) implies $u\in C^1(B)$ and therefore $J_1(u)\subset\overline{J_0(D)\cap\Lambda}$, hence

$$\overline{J_1(u)}=\overline{J_0(D)\cap\Lambda}.$$

This shows that, in general, discontinuities in the second derivatives of the data $\mathcal{E}$ have to be identified in order to get the whole jump set of D.

Once the partition $(\Omega_m)_{m=1}^M$ is known, the coefficients μ, D can be recovered from the jumps in $\mathcal{E}$, $\frac{\Delta\mathcal{E}}{\mathcal{E}}$ and the boundary values of u.

Proposition 5. *Let μ, D be of the form (3.2.1) with $(\Omega_m)_{m=1}^M$ known. Furthermore, let $\mathcal{E}$ satisfy (3.1.1),(3.1.2) for a known boundary illumination g. Then, μ and D can be determined uniquely from $\mathcal{E}$.*

Proof. Let $x \in \partial\Omega_m \cap \partial\Omega_n$ for some $m, n \in \{1, \ldots, M\}$. Since $u \in C^0(\overline{\Omega})$,

$$\frac{\lim_{y\to x} \mathcal{E}(y)|_{\Omega_m}}{\lim_{z\to x} \mathcal{E}(z)|_{\Omega_n}} = \frac{\mu_m u(x)}{\mu_n u(x)} = \frac{\mu_m}{\mu_n}. \tag{3.2.7}$$

Furthermore, take $x \in \partial\Omega \cap \partial\Omega_k$ (for some $k \in \{1, \ldots, M\}$). We have

$$\lim_{y\to x} \frac{\mathcal{E}(y)|_{\Omega_k}}{g(x)} = \mu_k \lim_{y\to x} \frac{u(y)|_{\Omega_k}}{g(x)} = \mu_k.$$

Starting in Ω_k and using (3.2.7) on all interfaces, we recover all μ_m, $m = 1, \ldots, M$. Finally, to obtain D_m, $m = 1, \ldots, M$, we use (3.2.4), that is,

$$\frac{\mu_m}{D_m} = \frac{\Delta\,\mathcal{E}(y)}{\mathcal{E}(y)} \quad \text{for all } y \in \Omega_m.$$

□

Remark 2. If g is not known, Proposition 5 can be used to determine the parameters μ, D up to a constant.

3.3. A Mumford-Shah-like functional for qPAT

In Section 3.2, we showed that piecewise constant absorption and diffusion coefficients μ, D, can be recovered from noise-free data $\mathcal{E}$ by an analytical procedure which first determines the coefficient jumps, i.e., the partition $(\Omega_m)_{m=1}^M$, and then the numerical values $(\mu_m, D_m)_{m=1}^M$. In [94], such a two-step approach was implemented numerically (for the problem (P3)).

In the presence of significant amounts of noise in the data, however, such an approach is infeasible, since it requires the detection of jumps of derivatives up to second order of the data $\mathcal{E}^\delta$. In particular, jumps may remain partially undetected (e.g., if the edge detection has to be restricted to first derivatives due to noise, see Remark 1 and the numerical examples in Section 3.4), leading to an incomplete estimated partition and therefore highly erroneous parameter estimates.

To overcome this problem, we propose a variational approach favouring piecewise constant solutions that estimates the numerical values of piecewise constant μ, D and their jumps at the same time.

There are multiple different methods for piecewise constant regularization of inverse problems. For instance, a popular class of methods is based on the *level set method* [96] or variations of it, e.g., [38, 41, 49, 112, 113]). This approach has been suggested for qPAT (using the radiative transfer model) in [50], however, it was only tested using multiple measurements. In this article, we use an *Ambrosio-Tortorelli* approximation of a *Mumford-Shah-like* functional (which was first suggested for *electrical impedance tomography* in [103]). The main advantage of this approximation is that we can utilize incomplete jump information (obtained, for instance, from jumps of the data or other means) to initialize the minimization procedure (see Section 3.3.3). Numerically, leads to faster convergence (and in some cases improved minimizers). Additionally, the number of segments does not have to be known in advance (in contrast to *multiple level set methods*) and the minimization with respect to the jump indicator functions is a simple elliptic problem.

We want to minimize the Mumford-Shah-like functional

$$\begin{aligned}\mathcal{F}(\mu, D, K_\mu, K_D) = &\frac{1}{2}\left\|\mathcal{E}(\mu, D) - \mathcal{E}^\delta\right\|^2_{L^2(\Omega)}\\&+\frac{\alpha_\mu}{2}\int_{\Omega\setminus K_\mu}|\nabla\mu|^2\,dx + \frac{\alpha_D}{2}\int_{\Omega\setminus K_D}|\nabla D|^2\,dx\\&+\beta_\mu H^{N-1}(K_\mu) + \beta_D H^{N-1}(K_D),\end{aligned} \tag{3.3.1}$$

where H^{N-1} is the $(N-1)$-dimensional Hausdorff-measure and $\mathcal{E}(\mu, D)$ the operator that maps the (unknown) parameters μ, D to the measurements $\mathcal{E}$ satisfying (3.1.1),(3.1.2). The minimum is taken over all μ, D in suitable (that is, point-wise bounded from below and above) subsets of $W^{1,2}(\Omega\setminus K_\mu), W^{1,2}(\Omega\setminus K_D)$ and all closed sets $K_\mu, K_D \subset \Omega$ (the jump sets of the coefficients μ, D).

Functionals of this type, first introduced by Mumford and Shah for image denoising and segmentation in [93], have been applied for a wide range of inverse problems, see, e.g., [55, 80, 82, 99, 100, 103]). The basic idea behind the functional is as follows. The *discrepancy term*

$$\frac{1}{2}\left\|\mathcal{E}(\mu, D) - \mathcal{E}^\delta\right\|^2_{L^2(\Omega)}$$

forces minimizing coefficients $\hat{\mu}, \hat{D}$ to be close (in L^2-sense) to a solution of the inverse problem $\mathcal{E}(\mu, D) = \mathcal{E}^\delta$ (of which there are infinitely many), while the *regularization terms*

$$\frac{\alpha_\mu}{2}\int_{\Omega\setminus K_\mu}|\nabla\mu|^2\,dx + \frac{\alpha_D}{2}\int_{\Omega\setminus K_D}|\nabla D|^2\,dx + \beta_\mu H^{N-1}(K_\mu) + \beta_D H^{N-1}(K_D)$$

force both the variation of $\hat{\mu}, \hat{D}$ (outside their jump sets $\hat{K}_\mu, \hat{K}_D$) as well as the hyper-surface area of $\hat{K}_\mu, \hat{K}_D$ to be small. The regularization parameters α_μ, α_D control the amount of continuous variation the parameters may have, whereas β_μ, β_D control the complexity of the coefficient's jump sets K_μ, K_D.

Note that while in general, minimizers of this functional can have some continuous variation, they have to be close to piecewise constant for large values of α_μ, α_D. In fact, the Ambrosio-Tortorelli approximation of the functional (3.3.1), which will be introduced in Section 3.3.2, can also be used for piecewise constant regularization (in the limit $\alpha_\mu, \alpha_D \to \infty$, see Remark 5).

3.3.1. Existence of minimizers

Existence of minimizers of functionals like (3.3.1) (which are, in general, not unique) was first established in [51] for image segmentation and in [103] for regularization of non-linear operator equations.

To ensure that $\mathcal{E}(\mu, D)$ is well-defined and that $\mathcal{F}$ has a minimizer, point-wise bounds have to be enforced (see [73]), so we have to restrict the coefficients to $X_a^b(\Omega) = \{f \in L^\infty(\Omega) \colon a \leq f \leq b \text{ a.e. in } \Omega\}$ for some $0 < a, b < \infty$ a priori. We also require the following Lemma, the proof follows the ideas in [54].

Lemma 3. *The non-linear measurement operator*

$$\mathcal{E} \colon X_a^b(\Omega)^2 \subset L^2(\Omega)^2 \to L^2(\Omega), \;\; \mathcal{E}(\mu, D) = \mu\, u(\mu, D),$$

where $u(\mu, D)$ solves (3.1.2), is continuous.

Proof. Let $(\mu_n, D_n) \to (\mu, D)$ in $X_a^b(\Omega)^2 \subset L^2(\Omega)^2$. Furthermore, let $u_n := u(\mu_n, D_n)$ and $u := u(\mu, D)$ be solutions of (3.1.2) corresponding to the given coefficients.

By the usual energy estimates for (3.1.2) (cf. [56, Chapter 6, Theorem 2]) we have

$$\|u_n\|_{W^{1,2}(\Omega)} \leq C(a, b, \Omega) \, \|g\|_{L^2(\partial\Omega)} \,.$$

Hence, there exists a (re-labeled) subsequence $(u_k)_{k\in\mathbb{N}}$ with $u_k \rightharpoonup \overline{u}$ weakly in $W^{1,2}(\Omega)$ for some $\overline{u} \in W^{1,2}(\Omega)$. From the weak form of (3.1.2) we get for all $v \in W^{1,\infty}(\Omega)$ and $k \in \mathbb{N}$

$$\begin{aligned}
&\langle D\nabla(u_k - u), \nabla v\rangle_{L^2(\Omega)^2} + \langle \mu(u_k - u), v\rangle_{L^2(\Omega)} \\
&\qquad\qquad = \langle (D - D_k)\nabla u_k, \nabla v\rangle_{L^2(\Omega)^2} + \langle (\mu - \mu_k)u_k, v\rangle_{L^2(\Omega)} \\
&\qquad\qquad \leq C(\|D_k - D\|_{L^2(\Omega)} + \|\mu_k - \mu\|_{L^2(\Omega)}) \, \|g\|_{L^2(\partial\Omega)} \, \|v\|_{W^{1,\infty}(\Omega)} \,.
\end{aligned}$$

Taking $k \to \infty$ and using the fact that the left side acts as a bounded linear functional on $u_k \in W^{1,2}(\Omega)$, we obtain for all $v \in W^{1,\infty}(\Omega)$

$$\langle D\nabla(\overline{u} - u), \nabla v\rangle_{L^2(\Omega)^2} + \langle \mu(\overline{u} - u), v\rangle_{L^2(\Omega)} = 0.$$

By density of $W^{1,\infty}(\Omega) \subset W^{1,2}(\Omega)$, this implies $\overline{u} = u$. Since the same argument also holds for every subsequence of the original sequence $(u_n)_{n\in\mathbb{N}}$, we get $u_n \rightharpoonup u$ weakly in $W^{1,2}(\Omega)$ and thus $u_n \to u$ strongly in $L^2(\Omega)$.

Finally, since $u \in L^\infty(\Omega)$ by the maximum principle, continuity of $\mathcal{E}$ follows from

$$\|\mu_n u_n - \mu u\|_{L^2(\Omega)} \leq \|\mu_n - \mu\|_{L^2(\Omega)} \, \|u\|_{L^\infty(\Omega)} + \|u_n - u\|_{L^2(\Omega)} \, \|\mu_n\|_{L^\infty(\Omega)} \,.$$

□

Remark 3. Since $\|f\|_{L^2}^2 \leq \|f\|_{L^1(\Omega)} \|f\|_{L^\infty(\Omega)}$ for all $f \in X_a^b(\Omega)$, the operator $\mathcal{E}\colon X_a^b(\Omega)^2 \subset L^1(\Omega)^2 \to L^2(\Omega)$ is also continuous.

Following [7, 103], we show the existence of minimizers of a weak form of $\mathcal{F}$ defined for coefficients μ, D in the space $\mathcal{SBV}(\Omega)$, the *special functions of bounded variation*, which may have jump discontinuities. For a quick introduction, see Appendix 3.6.1.

We obtain the functional $\overline{\mathcal{F}}\colon X_a^b(\Omega)^2 \cap \mathcal{SBV}(\Omega)^2 \to \mathbb{R}$,

$$\begin{aligned}\overline{\mathcal{F}}(\mu, D) = \frac{1}{2}\left\|\mathcal{E}(\mu, D) - \mathcal{E}^\delta\right\|_{L^2(\Omega)}^2 + \frac{\alpha_\mu}{2}\int_\Omega |\nabla\mu|^2\, dx \\ + \frac{\alpha_D}{2}\int_\Omega |\nabla D|^2\, dx + \beta_\mu\, H^{N-1}[S(\mu)] + \beta_D\, H^{N-1}[S(D)],\end{aligned} \tag{3.3.2}$$

where $S(f)$ denotes the *approximate discontinuity set* of a Lebesgue-measurable function f and $\nabla\mu, \nabla D$ the density of the absolutely continuous part (with respect to the Lebesgue measure) of the respective distributional gradients (see Appendix 3.6.1).

In this setting, the existence of minimizers can be established using the direct method and the $\mathcal{SBV}$ compactness theorem.

Proposition 6. *The weak Mumford-Shah-like functional $\overline{\mathcal{F}}$ has at least one minimizer $(\hat{\mu}, \hat{D})$ in $X_a^b(\Omega)^2 \cap \mathcal{SBV}(\Omega)^2$.*

Proof. Let $(\mu_n, D_n) \in X_a^b(\Omega)^2 \cap \mathcal{SBV}(\Omega)^2$ be a minimizing sequence of the functional (3.3.2). Clearly, we have for all $n \in \mathbb{N}$

$$\begin{aligned}\|\mu_n\|_{L^\infty(\Omega)} + \int_\Omega |\nabla\mu_n|^2\, dx + H^{N-1}[S(\mu)] \leq C < \infty \\ \|\mathrm{D}_n\|_{L^\infty(\Omega)} + \int_\Omega |\nabla\mu_n|^2\, dx + H^{N-1}[S(D)] \leq C < \infty.\end{aligned}$$

By the $\mathcal{SBV}$-compactness theorem (see Section 3.6.1), and using Lemma 3, first applied to μ_n, then to the obtained subsequence of D_n, there exist $(\hat{\mu}, \hat{D}) \in \mathcal{SBV}(\Omega)^2$ and a subsequence $(\mu_k, D_k)_{k\in\mathbb{N}}$ (re-labeled) with

$$\begin{aligned}(\mu_k, D_k) \to (\hat{\mu}, \hat{D}) \text{ strongly in } L^1_{\mathrm{loc}}(\Omega)^2 \\ (\nabla\mu_k, \nabla D_k) \rightharpoonup (\nabla\hat{\mu}, \nabla\hat{D}) \text{ weakly in } L^2(\Omega; \mathbb{R}^N)^2 \\ H^{N-1}[S(\hat{\mu})] \leq \liminf_{k\to\infty} H^{N-1}[S(\mu_k)] \\ H^{N-1}[S(\hat{D})] \leq \liminf_{k\to\infty} H^{N-1}[S(D_k)].\end{aligned}$$

We also have $(\hat{\mu}, \hat{D}) \in X_a^b(\Omega)^2$ since $X_a^b(\Omega)^2$ is closed in $L^1_{\mathrm{loc}}(\Omega)^2$. Furthermore, it is a minimizer of $\overline{\mathcal{F}}$ since the $L^2(\Omega)$-norm is weakly lower semi-continuous and $\mathcal{E}\colon X_a^b(\Omega)^2 \subset L^1(\Omega)^2 \to L^2(\Omega)$ is continuous. □

Remark 4. If the minimizer $(\hat{\mu}, \hat{D})$ has *essentially closed* jump sets $S(\hat{\mu}), S(\hat{D})$ (that is, taking the closure of the jump sets does not increase their H^{N-1}-measure) the quadruple $\left(\hat{\mu}, \hat{D}, \overline{S(\hat{\mu})}, \overline{S(\hat{D})}\right)$ also minimizes the strong Mumford-Shah functional (3.3.1) among all $\mu \in X_a^b(\Omega) \cap W^{1,2}(\Omega \setminus K_\mu)$, $D \in X_a^b(\Omega) \cap W^{1,2}(\Omega \setminus K_D)$ and K_μ, K_D closed. While essential closedness of jump sets of Mumford-Shah-minimizers can be established under certain conditions on the discrepancy term [51, 73, 103], this is out of the scope of this article.

3.3.2. Approximation

Using the approach of Ambrosio and Tortorelli (cf. [8]), one can obtain functionals

$$\mathcal{F}_\epsilon \colon X_a^b(\Omega)^2 \cap W^{1,2}(\Omega)^2 \times X_0^1(\Omega)^2 \cap W^{1,2}(\Omega)^2 \to \mathbb{R}$$

that approximate the functional $\overline{\mathcal{F}}$ from (3.3.2) and are easier to minimize:

$$\begin{aligned}
\mathcal{F}_\epsilon(\mu, D, v_\mu, v_D) = {} & \frac{1}{2} \left\| \mathcal{E}(\mu, D) - \mathcal{E}^\delta \right\|_{L^2(\Omega)}^2 \\
& + \frac{\alpha_\mu}{2} \int_\Omega (v_\mu^2 + \zeta_\mu) |\nabla \mu|^2 \, dx + \frac{\alpha_D}{2} \int_\Omega (v_D^2 + \zeta_D) |\nabla D|^2 \, dx \\
& + \beta_\mu \int_\Omega \left(\epsilon |\nabla v_\mu|^2 + \frac{(v_\mu - 1)^2}{4\epsilon} \right) dx \\
& + \beta_D \int_\Omega \left(\epsilon |\nabla v_D|^2 + \frac{(v_D - 1)^2}{4\epsilon} \right) dx
\end{aligned} \tag{3.3.3}$$

It is well-known that, for all $\alpha, \beta > 0$ and $\zeta = o(\epsilon)$,

$$\alpha \int_\Omega (v^2 + \zeta) |\nabla f|^2 + \beta \left(\epsilon |\nabla v|^2 + \frac{(v-1)^2}{4\epsilon} \right) dx \xrightarrow[\epsilon \to 0]{} \alpha \int_\Omega |\nabla f|^2 \, dx + \beta \, H^{N-1}[S(f)]$$

in the sense of Γ-convergence in $L^1(\Omega)$ (formally, the latter has to be extended to an additional variable, see [8, 103]). Since the data term is continuous in $L^1(\Omega)$ and Γ-convergence is stable under continuous perturbations, we thus get $\Gamma\text{-}\lim_{\epsilon \to 0} \mathcal{F}_\epsilon = \overline{\mathcal{F}}$ and therefore $L^1(\Omega)$-convergence of (a subsequence of) $\mathcal{F}_\epsilon$-minimizers (which can be shown to lie in a compact set [8]) to $\overline{\mathcal{F}}$-minimizers.

The existence of a minimizer of (3.3.3) can be established using the direct method.

Proposition 7. *The functional $\mathcal{F}_\epsilon$ has at least one minimizer $(\hat{\mu}, \hat{D}, \hat{v}_\mu, \hat{v}_D)$ in $X_a^b(\Omega)^2 \cap W^{1,2}(\Omega)^2 \times X_0^1(\Omega)^2 \cap W^{1,2}(\Omega)^2$.*

Proof. F_ϵ is coercive with respect to the semi-norm

$$|\mu|_{W^{1,2}(\Omega)} + |D|_{W^{1,2}(\Omega)} + \|v_\mu\|_{W^{1,2}(\Omega)} + \|v_D\|_{W^{1,2}(\Omega)} \,,$$

which, combined with the restriction $(\mu, D) \in X_a^b(\Omega)^2$, shows that a minimizing sequence is bounded in $W^{1,2}(\Omega)^4$, so it contains a subsequence that converges weakly to $(\hat{\mu}, \hat{D}, \hat{v}_\mu, \hat{v}_D)$ in $W^{1,2}(\Omega)^4$ (and thus strongly in $L^2(\Omega)^4$). Moreover, note that the spaces $X_a^b(\Omega)$ and $X_0^1(\Omega)$ are closed in $L^2(\Omega)$. The Proposition follows since the discrepancy term is continuous in $L^2(\Omega)^2$ and the regularization terms are weakly lower semi-continuous in $W^{1,2}(\Omega)^4$ (cf. [48, Theorem 1.13] for the α-terms). $\square$

Remark 5. If we vary α_μ, α_D with ϵ and take

$$\alpha_\mu, \alpha_D \xrightarrow[\epsilon \to 0]{} \infty$$

the minimizers of $\mathcal{F}_\epsilon$ converge to piecewise constant (in $\mathcal{SBV}$-sense, that is, with gradient vanishing almost everywhere) functions $(\hat{\mu}, \hat{D})$ that minimize

$$\widetilde{\mathcal{F}}(\mu, D) = \frac{1}{2} \left\| \mathcal{E}(\mu, D) - \mathcal{E}^\delta \right\|_{L^2(\Omega)}^2 + \beta_\mu \, H^{N-1}[S(\mu)] + \beta_D \, H^{N-1}[S(D)]$$

among all piecewise constant μ, D. A proof (for the single variable case) can be found in [8]. This explains, in light of Section 3.2, why this type of regularization is useful for qPAT.

3.3.3. Minimization

In this subsection, we proceed formally, i.e., without proving convergence, existence of minimizers of sub-problems and that the necessary derivatives and adjoints exist. For the minimization of (3.3.3), we suggest the following alternating directions approach:

Algorithm 1.

1. Choose parameters $a, b, \epsilon, \alpha_\mu, \alpha_D, \beta_\mu, \beta_D > 0$.
2. Find an initial estimate $\hat{K}$ of the edge set $J_0(\mu) \cup J_0(D)$ using edge detection.
3. Initialize with $\mu^0 = D^0 \equiv 1$ and $v_\mu^0 = v_D^0 = 1 - 1_{\hat{K}}$.
4. Iterate until convergence:
   (i) $(\mu^{n+\frac{1}{2}}, D^{n+\frac{1}{2}}) = \arg\min_{\mu, D} \; \mathcal{F}_\epsilon(\mu, D, v_\mu^n, v_D^n)$
   (ii) $(v_\mu^{n+1}, v_D^{n+1}) = \arg\min_{v_\mu, v_D} \; \mathcal{F}_\epsilon(\mu^{n+\frac{1}{2}}, D^{n+\frac{1}{2}}, v_\mu, v_D)$

We now explain the steps in more detail.

Initialization using edge detection

In our numerical simulations, it became clear that using Proposition 4 to obtain a reasonable estimate $\hat{K}$ of $J_0(\mu) \cup J_0(D)$ leads to faster convergence and better minimizers than simply taking $\hat{K} = \emptyset$.

Given the noisy measurements $\mathcal{E}^\delta$, we have to estimate the discontinuities (or edges) of $\mathcal{E}^\delta$, $|\nabla \mathcal{E}^\delta|^2$ and $|\Delta \mathcal{E}^\delta|$. Since the jumps in these functions are of *multiplicative* nature (proportional to the local value of u or $\nabla u \cdot \nu$), it is advantageous to apply a logarithmic transformation prior to edge detection (to obtain constant contrast), see [94].

Due to noise, the data has to be smoothed prior to taking derivatives (turning discontinuities into areas with large gradients). We smooth by convolution with a Gaussian, since this approach has the advantage that differentiation and smoothing can be done in one step (by differentiating the low-pass filter instead of the function). We have

$$\begin{aligned}
\mathrm{G}_\sigma(x) &= (2\pi)^{-\frac{N}{2}}\sigma^{-N}\exp\left(\frac{-x^2}{2\sigma^2}\right)\\
(\nabla\,\mathrm{G}_\sigma)(x) &= (2\pi)^{-\frac{N}{2}}\sigma^{-(N+2)}(-x)\exp\left(\frac{-x^2}{2\sigma^2}\right)\\
(\Delta\,\mathrm{G}_\sigma)(x) &= (2\pi)^{-\frac{N}{2}}\sigma^{-N+2}\left(\frac{|x|^2}{\sigma^2}-N\right)\exp\left(\frac{-x^2}{2\sigma^2}\right).
\end{aligned}$$

Similar to [94], we proceed as follows:

1. Detect edges $\hat{K}_0$ of $f_0 := \log\left(\mathcal{E}^\delta * 1_B\, G_{\sigma_0}\right)|_{\Omega\ominus B}$
2. Detect edges $\hat{K}_1$ of $f_1 := \log\left(\left|\left(\mathcal{E}^\delta * 1_B\,\nabla G_{\sigma_1}\right)\right|^2 \vee \gamma\right))|_{(\Omega\setminus\hat{K}_0)\ominus B}$
3. Detect edges $\hat{K}_2$ of $f_2 := \log\left(\left|\left(\mathcal{E}^\delta * 1_B\,\Delta G_{\sigma_2}\right)\right|\right)|_{(\Omega\setminus(\hat{K}_0\cup\hat{K}_1))\ominus B}$
4. Take $\hat{K} = \hat{K}_0 \cup \hat{K}_1 \cup \hat{K}_2$

Here, 1_B acts as a cut-off function for the filters (e.g., using $B = B^p_\rho$, the p-norm ball of radius ρ). The operation $A \ominus B = \{z \in \Omega \mid (B + z) \subset A\}$ denotes set erosion, which is performed to avoid multiple detection of edges (by ensuring that the cut-off filter does not intersect with already detected edges or the outside of the domain). Note, however, that for large B this may lead to parts of edges (close to the domain boundary or already detected edges) not being detected. The scalar γ is a minimal value enforced for $|\nabla \mathcal{E}^\delta|^2$ (to avoid creating singularities at zeros).

The edge detection itself is performed by applying thresholds ξ_0,ξ_1,ξ_2 to the functions $|\nabla f_0|, |\nabla f_1|, |\nabla f_2|$ (taking the super-level sets as edge sets). Note that in contrast to [94], no complete segmentation is necessary and cruder edge estimates suffice, that is, the detected edges don't have to be reduced to thin curves.

Iteration

In step (i), to find, for fixed $v_\mu, v_D \in X_0^1(\Omega) \cap W^{1,2}(\Omega)$,

$$\operatorname*{arg\,min}_{\mu, D \in X_a^b(\Omega) \cap W^{1,2}(\Omega)} \mathcal{F}_\epsilon(\mu, D)$$

we use Gauss-Newton-minimization. That is, in every iteration of an inner loop, we linearly approximate $\mathcal{E}(\mu_k + s_\mu, D_k + s_D) \approx \mathcal{E}(\mu_k, D_k) + \mathcal{E}'(\mu_k, D_k)(s_\mu, s_D)$ and take update steps

$$\begin{aligned} s = \operatorname*{arg\,min}_{s_\mu, s_D \in W^{1,2}(\Omega)} & \frac{1}{2} \left\| \mathcal{E}(\mu_k, D_k) + \mathcal{E}'(\mu_k, D_k)(s_\mu, s_D) - \mathcal{E}^\delta \right\|^2_{L^2(\Omega)} \\ + \frac{\alpha_\mu}{2} \int_\Omega (v_\mu^2 + \zeta_\mu) |\nabla(\mu_k + s_\mu)|^2 \, dx &+ \frac{\alpha_D}{2} \int_\Omega (v_D^2 + \zeta_D) |\nabla(D_k + s_D)|^2 \, dx \end{aligned} \tag{3.3.4}$$

which we then project into $X_a^b(\Omega)^2$, so we update with

$$(\mu_{k+1}, D_{k+1}) = (\mu_k, D_k) + (s \wedge a) \vee b.$$

A straightforward calculation shows that a minimizer $s = (s_\mu, s_D)$ of (3.3.4) satisfies the weak form of

$$\begin{aligned} &\mathcal{E}'(\mu_k, D_k)^* \, \mathcal{E}'(\mu_k, D_k)(s_\mu, s_D) + \left(\alpha_\mu L_{(v_\mu^2 + \zeta_\mu)} \, s_\mu, \ \alpha_D L_{(v_D^2 + \zeta_D)} \, s_D \right) \\ &\quad = - \, \mathcal{E}'(\mu_k, D_k)^* [\mathcal{E}(\mu_k, D_k) - \mathcal{E}^\delta] - \left(\alpha_\mu L_{(v_\mu^2 + \zeta_\mu)} \, \mu_k, \ \alpha_D L_{(v_D^2 + \zeta_D)} \, D_k \right) \\ &\quad =: (R_{\mu_k}, R_{D_k}) \end{aligned} \tag{3.3.5}$$

with homogeneous Neumann boundary conditions for s_μ, s_D and

$$L_\sigma \colon W^{1,2}(\Omega) \to W^{-1,2}(\Omega), \ x \mapsto -\nabla \cdot (\sigma \nabla x).$$

The linear operator $\mathcal{E}'(\mu, D)$ and its (formal) adjoint $\mathcal{E}'(\mu, D)^*$ are given by

$$\begin{aligned} \mathcal{E}'(\mu, D)(s_\mu, s_D) &= s_\mu u + \mu L_{\mu,D}^{-1}(-s_\mu u) + \mu L_{\mu,D}^{-1}[\nabla \cdot (s_D \nabla u)] \\ \mathcal{E}'(\mu, D)^* \, t &= \left(tu - u L_{\mu,D}^{-1}(\mu t), -\nabla u \cdot \nabla L_{\mu,D}^{-1}(\mu t) \right) \end{aligned} \tag{3.3.6}$$

where $u = u(\mu, D)$ and

$$L_{\mu,D} \colon W_0^{1,2}(\Omega) \to W^{-1,2}(\Omega), \ x \mapsto -\nabla \cdot (D \nabla x) + \mu x.$$

By introducing auxiliary variables y_1, y_2, y_3 (and taking $\mu = \mu_k, D = D_k$), the equations (3.3.5),(3.3.6) can be re-written as the system of (weak) PDE

$$\begin{aligned} (s_\mu u + \mu y_1 + \mu y_2) u - u y_3 + \alpha_\mu L_{(v_\mu^2 + \zeta_\mu)} \, s_\mu = R_\mu, &\quad \frac{\partial s_\mu|_{\partial\Omega}}{\partial \nu} = 0 \\ -\nabla u \cdot \nabla y_3 + \alpha_D L_{(v_D^2 + \zeta_D)} \, s_D = R_D, &\quad \frac{\partial s_D|_{\partial\Omega}}{\partial \nu} = 0 \\ L_{\mu,D} \, y_3 = \mu(s_\mu u + \mu y_1 + \mu y_2), &\quad y_3|_{\partial\Omega} = 0 \\ L_{\mu,D} \, y_2 = \nabla \cdot (s_D \nabla u), &\quad y_2|_{\partial\Omega} = 0 \\ L_{\mu,D} \, y_1 = -s_\mu u, &\quad y_1|_{\partial\Omega} = 0 \end{aligned} \tag{3.3.7}$$

which is amenable to discretization as a sparse matrix using, e.g., the *finite element method (FEM)*.

In step (ii) of the outer loop we have to find, for fixed $\mu, D \in X_a^b(\Omega) \cap W^{1,2}(\Omega)$,

$$\underset{v_\mu, v_D \in X_0^1(\Omega)\cap W^{1,2}(\Omega)}{\arg\min} \quad \mathcal{F}_\epsilon(v_\mu, v_D).$$

The minimizer (v_μ, v_D) satisfies the linear equations

$$\begin{aligned} \left(-2\beta\epsilon\Delta + (\alpha_\mu|\nabla\mu|^2 + \frac{\beta_\mu}{2\epsilon})\,\mathrm{Id}\right) v_\mu &= \frac{\beta}{2\epsilon}, \quad \frac{\partial v_\mu|_{\partial\Omega}}{\partial\nu} = 0 \\ \left(-2\beta\epsilon\Delta + (\alpha_D|\nabla D|^2 + \frac{\beta_D}{2\epsilon})\,\mathrm{Id}\right) v_D &= \frac{\beta}{2\epsilon}, \quad \frac{\partial v_D|_{\partial\Omega}}{\partial\nu} = 0 \end{aligned} \tag{3.3.8}$$

which can be solved separately and implemented numerically using FEM.

3.4. Implementation and numerical results

In this section, the proposed algorithm is tested on two sets of simulated two-dimensional data (with different parameter range and level of detail). We also vary the noise on the data since the reconstruction quality strongly depends on the noise level.

The data (see Figures 3.1 and 3.2) was generated in the diffusion model (3.1.2) using self-written (linear-basis) finite element code in *MATLAB*. For both examples, we took $\Omega = [0,5]^2$ and used a uniform boundary condition $g \equiv 1$. The simulated data were generated on a (400×400)-grid and then down-sampled (by averaging) to (200×200) to avoid inverse crime. After that, Gaussian noise with different intensities (standard deviations of 0.5% and 10% of the average signal value $\frac{1}{|\Omega|}\int_\Omega \mathcal{E}(x)\,dx$) was added to the data.

The edge detector described in Section 3.3.3 was implemented by finite difference approximations of $|\nabla f_0|, |\nabla f_1|, |\nabla f_2|$ using central differences inside and one-sided differences near the boundary of the domain. The functions f_1, f_2, f_3 were calculated by convolution filtering with the *MATLAB* function *imfilter*. For all examples, we used a square cutoff function, i.e., $B = B_\rho^\infty$ with $\rho = 2\lceil\sigma_k\rceil$ (where $k = 0, 1, 2$).

The edge detector is used to detect jumps in the derivatives of the data $\mathcal{E}^\delta$ up to second order (to obtain an initial estimate of the parameter jump set $J_0(\mu) \cup J_0(D)$). Since this process is highly sensitive with respect to noise, we varied the edge detection procedure subject to the amount of noise in the data. In the noise-free examples, we estimated the jumps of all three functions f_0, f_1, f_3, that is, jumps of derivatives of $\mathcal{E}^\delta$ up to second order. We restricted the jump estimation to f_0, f_1 for

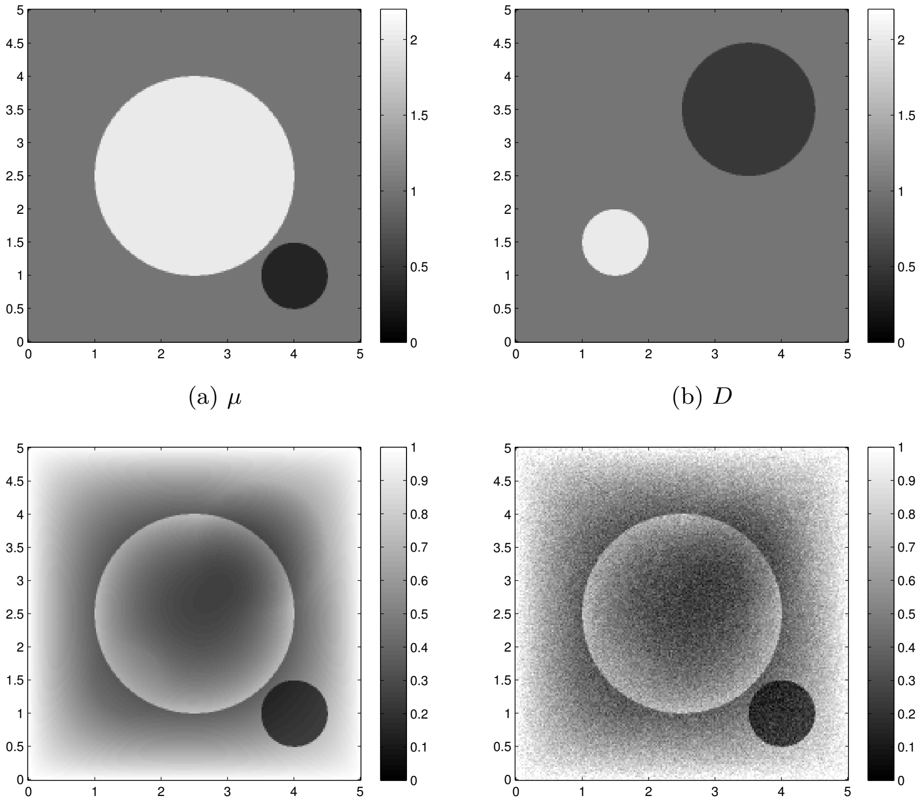

(a) μ (b) D

(c) $\mathcal{E}(\mu, D)$ (d) $\mathcal{E}(\mu, D)^\delta$ (10% noise)

Figure 3.1.: Example A. Parameters μ, D and FEM-generated data $\mathcal{E}(\mu, D)$.

the low-noise examples (i.e., jumps of derivatives up to first order) and f_0 in the high-noise examples (only jumps in the data $\mathcal{E}^\delta$ itself).

To obtain the parameters μ, D given an initial estimate of their combined edge set $J_0(\mu) \cup J_0(D)$, we used the Ambrosio-Tortorelli approximation (3.3.3) of the Mumford-Shah functional introduced in Section 3.3. To minimize the functional, we used Algorithm 1, iterating, for all examples, the outer alternating-directions loop until the functional changes by less than 0.01% and the inner Gauss-Newton loop until the functional value changes less than 1%. We directly implemented the systems (3.3.7) and (3.3.8) using (self-written) linear-basis finite element code. The implementation is not fully conforming, that is, where necessary we used conversions between piecewise linear and piecewise constant functions for simplicity. The discrete systems were solved using the standard *MATLAB* sparse equation solver *mldivide*.

For all examples, we chose $a = 0.01, b = 3$ and $\epsilon = 0.01$. The other reconstruction parameters used (which were selected by hand) are listed in Tables 3.1 and 3.2.

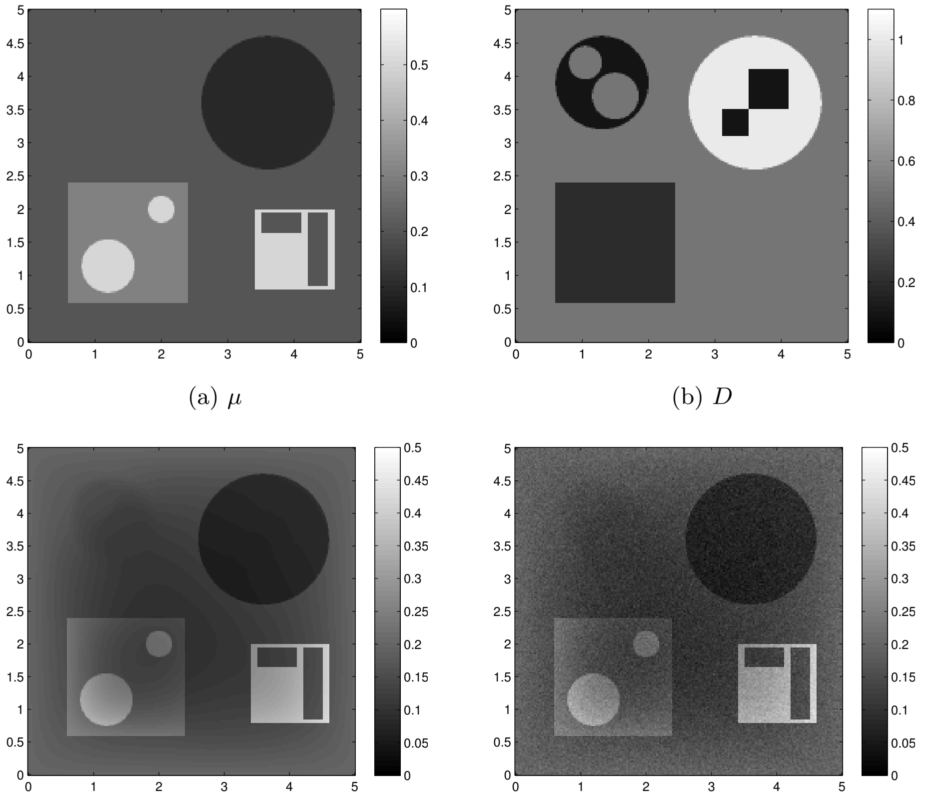

(a) μ

(b) D

(c) $\mathcal{E}(\mu, D)$

(d) $\mathcal{E}(\mu, D)^\delta$ (10% noise)

Figure 3.2.: Example B. Parameters μ, D and FEM-generated data $\mathcal{E}(\mu, D)$.

Reconstruction results and error profiles at different noise levels can be seen in Figures 3.3 and 3.4. In both examples, the noise-free reconstructions are very accurate and contain mostly smoothing error. In the low-noise reconstructions, due to the fact that more regularization is necessary, some of the parameter variation is underestimated. In the high-noise examples, most detail in D is lost since a lot of regularization is required to get reasonable results. The fine detail in μ can, however, still be recovered very accurately in both examples.

	$\boldsymbol{\alpha_\mu}$	$\boldsymbol{\alpha_D}$	$\boldsymbol{\beta_\mu}$	$\boldsymbol{\beta_D}$	$\boldsymbol{\zeta_\mu}$	$\boldsymbol{\zeta_D}$
Ex. A (0% noise)	10^{-2}	10^{-4}	10^{-6}	10^{-8}	10^{-6}	10^{-4}
Ex. A (0.1% noise)	10^{-2}	10^{-5}	10^{-6}	10^{-8}	10^{-6}	10^{-3}
Ex. A (10% noise)	1	$5 \cdot 10^{-3}$	10^{-5}	$5 \cdot 10^{-6}$	10^{-5}	10^{-3}
Ex. B (0% noise)	10^{-2}	10^{-4}	10^{-6}	10^{-8}	10^{-6}	10^{-5}
Ex. B (0.1% noise)	10^{-2}	10^{-5}	10^{-6}	10^{-8}	10^{-6}	10^{-3}
Ex. B (10% noise)	1	10^{-3}	10^{-5}	10^{-7}	10^{-5}	10^{-3}

Table 3.1.: Parameters used for Figures 3.3 and 3.4 (for the functional (3.3.3)).

	$\boldsymbol{\sigma_0}$	$\boldsymbol{\sigma_1}$	$\boldsymbol{\sigma_2}$	$\boldsymbol{\xi_0}$	$\boldsymbol{\xi_1}$	$\boldsymbol{\xi_2}$	$\boldsymbol{\gamma}$
Ex. A (0% noise)	0.5	0.5	0.5	0.1	0.1	0.1	10^{-4}
Ex. A (0.1% noise)	0.5	2		0.05	0.06		10^{-5}
Ex. A (10% noise)	1.5			0.05			
Ex. B (0% noise)	0.5	0.5	0.5	0.1	0.1	0.1	10^{-6}
Ex. B (0.1% noise)	0.5	2.4		0.05	0.06		10^{-7}
Ex. B (10% noise)	1.5			0.03			

Table 3.2.: Parameters used for Figures 3.3 and 3.4 (for edge detection).

Remark 6. In some of the examples, minimization of (3.3.1) using log-parameters, i.e., the mapping $\overline{\mathcal{E}}\colon (\log \mu, \log D) \mapsto \mathcal{E}(\mu, D)$ instead of $\mathcal{E}$, gave slightly better results. Note that this approach leads to a different linearization and therefore also a different system (3.3.7) to be solved in every step. However, to keep the presentation simple, we decided to use the functional as presented in Section 3.3 for our numerical experiments.

We also tried to incorporate the Grüneisen coefficient Γ as an additional unknown into the reconstruction process, that is, to solve the problem (P3). Unfortunately, this proved to be highly unstable, even if the initial edge set was detected perfectly.

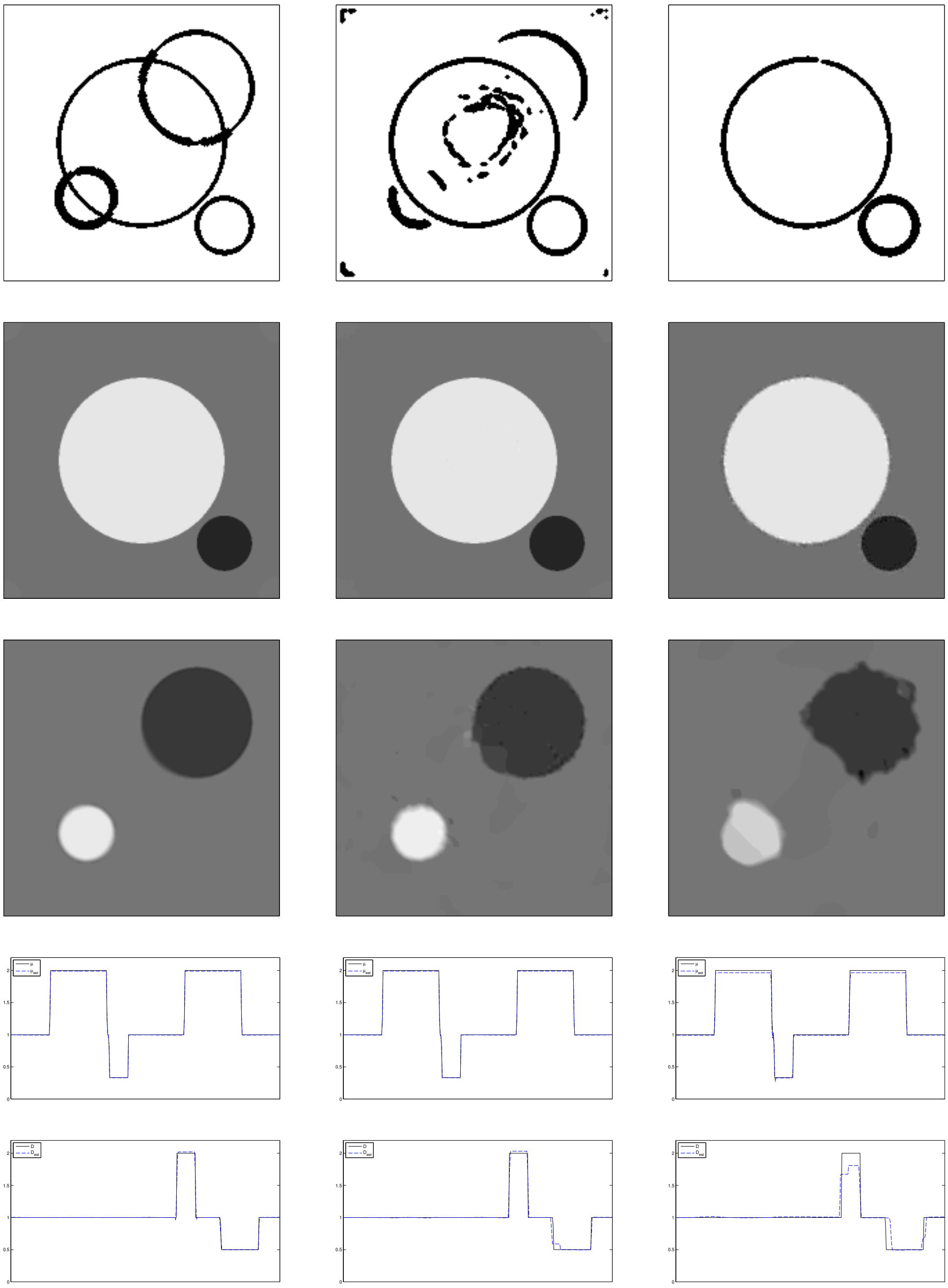

Figure 3.3.: Reconstructions A. Columns: 0%, 0.1% and 10% noise. Rows: Estimated edge set, reconstructed parameters μ_{est}, D_{est} and error profiles for $\mu_{\text{est}}, D_{\text{est}}$. The error profiles show values of the true and reconstructed parameters along the image diagonals. The color axis in the images of the reconstructed parameters was fixed to the same range as the true parameters shown in Figure 3.1.

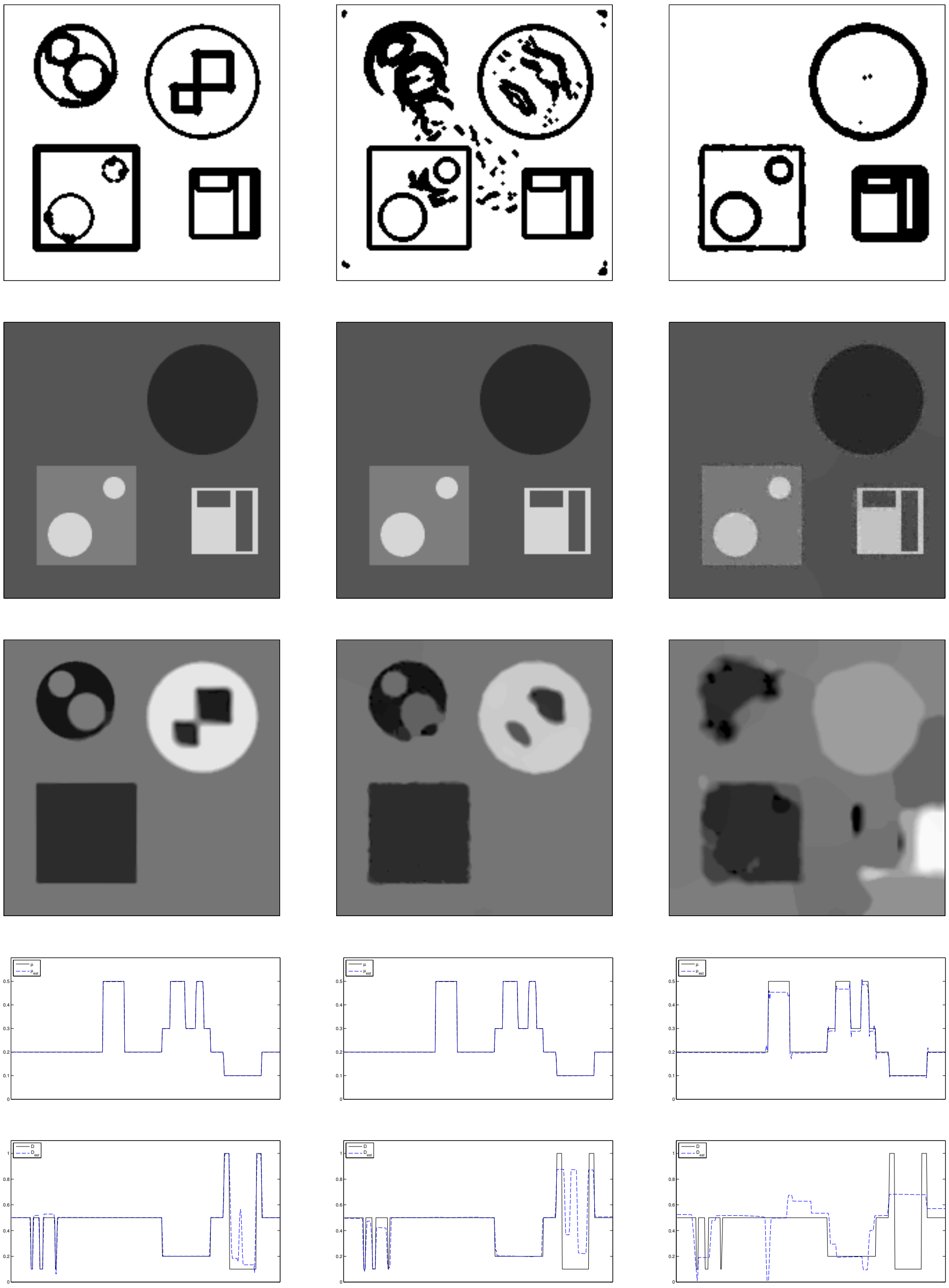

Figure 3.4.: Reconstructions B. Columns: 0%, 0.1% and 10% noise. Rows: Estimated edge set, reconstructed parameters μ_{est}, D_{est} and error profiles for $\mu_{\text{est}}, D_{\text{est}}$. The error profiles show valued of the true and reconstructed parameters along the image diagonals. The color axis in the images of the reconstructed parameters was fixed to the same range as the true parameters shown as in Figure 3.2.

3.5. Acknowledgements

This work has been supported by the Austrian Science Fund (FWF) within the project FSP P26687-"Interdisciplinary Coupled Physic Imaging" and by the IK I059-N funded by the University of Vienna.

3.6. Appendix

3.6.1. Special functions of bounded variation and the SBV-compactness theorem

This section briefly introduces the notion of $\mathcal{SBV}$-functions and their compactness theorem. For a more comprehensive presentation with proofs, see, e.g., [17].

For a function $f \in L^1(\Omega)$ with distributional gradient Df, we define its *total variation* by

$$|Df|_\Omega := \sup\{\langle Df, \varphi\rangle \mid \varphi \in C_c^1(\Omega; \mathbb{R}^N), \|\varphi\|_{L^\infty(\Omega;\mathbb{R}^N)} \leq 1\}$$

The space $\mathcal{BV}(\Omega)$, consisting of all $L^1(\Omega)$-functions with finite total variation (i.e., of bounded variation), is a Banach space with the norm

$$\|f\|_{\mathcal{BV}(\Omega)} := \|f\|_{L^1(\Omega)} + |Df|_\Omega.$$

Note that by the Riesz-Markov representation theorem, functions $f \in L^1(\Omega)$ are of bounded variation if and only if Df is a *finite vector Radon measure.* The measure Df can be decomposed into three parts

$$Df = D^a f + D^j f + D^c f.$$

$D^a f$ is the part of Df that is *absolutely continuous* with respect to the Lebesgue measure $\mathcal{L}^N$, i.e.,

$$D^a f = \nabla f\, \mathcal{L}^N$$

for some integrable density function ∇f. The *jump part* $D^j f$ is concentrated on the jump (or approximate discontinuity) set $S(f)$ defined by

$$S(f) := \{x \in \Omega \mid f^-(x) < f^+(x)\},$$

where, denoting with $B_\rho(x)$ the ball centered at x with radius ρ,

$$f^+(x) := \inf\left\{t \in \mathbb{R} \mid \lim_{\rho\to 0} \frac{\mathcal{L}^N(\{y \in B_\rho(x) \mid f(y) > t\})}{\mathcal{L}^N(B_\rho(x))} = 0\right\}$$
$$f^-(x) := \sup\left\{t \in \mathbb{R} \mid \lim_{\rho\to 0} \frac{\mathcal{L}^N(\{y \in B_\rho(x) \mid f(y) < t\})}{\mathcal{L}^N(B_\rho(x))} = 0\right\}.$$

Furthermore, for H^{N-1}-almost all $x \in S(f)$, there exists a *unit normal vector* $\nu(x)$ and we have

$$D^j f = (f^+ - f^-)\, \nu\, H^{N-1}|_{S(f)}.$$

The remaining *Cantor part* $D^c f$ is concentrated on a subset of $\Omega \setminus S(f)$ with intermediate Hausdorff dimension between $N-1$ and N.

A function $f \in \mathcal{BV}(\Omega)$ is a *special function of bounded variation* (or $f \in \mathcal{SBV}(\Omega)$) if $D^c f = 0$, that is,

$$Df = \nabla f\, \mathcal{L}^N + (f^+ - f^-)\, \nu\, H^{N-1}|_{S(f)}.$$

Furthermore, we have the following *compactness theorem* due to Ambrosio [6]:

Theorem 1. *Let f_n be a sequence in $\mathcal{SBV}(\Omega)$ with*

$$\|f_n\|_{L^\infty(\Omega)} + \int_\Omega |\nabla f_n|^p\, dx + H^{N-1}[S(f_n)] \leq M < \infty$$

for all $n \in \mathbb{N}$ and some $p > 1, M > 1$. Then there exist a subsequence $(f_{n_k})_{k\in\mathbb{N}}$ and $f \in \mathcal{SBV}(\Omega)$ with

$$\begin{aligned} f_{n_k} &\to f \ \textit{strongly in } L^1_{loc}(\Omega) \\ \nabla f_{n_k} &\rightharpoonup \nabla f \ \textit{weakly in } L^p(\Omega;\mathbb{R}^N) \\ H^{N-1}[f] &\leq \liminf_{k\to\infty} H^{N-1}[f_{n_k}]. \end{aligned}$$

4. The Levenberg-Marquardt iteration for numerical inversion of the power density operator

Authors and Contributions. The authors are Guillaume Bal, Wolf Naetar, Otmar Scherzer and John Schotland. The development of this article was a gradual, cooperative process. The author list is alphabetical, every author made significant contributions to the paper.

Publication Status. Published in [27]. Publication available for download at http://dx.doi.org/10.1515/jip-2012-0091. The version contained in this Chapter is a preprint available at http://arxiv.org/abs/1211.6034.

The Levenberg-Marquardt Iteration for Numerical Inversion of the Power Density Operator

G. Bal (gb2030@columbia.edu)[1]
W. Naetar (wolf.naetar@univie.ac.at)[2]
O. Scherzer (otmar.scherzer@univie.ac.at)[2,3]
J. Schotland (jcsch@umich.eu)[4]

[1]Department of Applied Physics and Applied Mathematics, Columbia University
New York, NY 10027, USA

[2]Computational Science Center, University of Vienna
Nordbergstr. 15, A-1090 Vienna, Austria

[3]Radon Institute of Computational and Applied Mathematics, Austrian Academy of Sciences
Altenbergerstr. 69, A-4040 Linz, Austria

[4]Department of Mathematics, University of Michigan
Ann Arbor, MI 48109, USA

November 27, 2012

In this paper we develop a convergence analysis in an *infinite* dimensional setting of the Levenberg-Marquardt iteration for the solution of a *hybrid conductivity imaging* problem. The problem consists in determining the spatially varying conductivity σ from a series of measurements of power densities for various voltage inductions. Although this problem has been very well studied in the literature, convergence and regularizing properties of iterative algorithms in an infinite dimensional setting are still rudimentary. We provide a partial result under the assumptions that the derivative of the operator, mapping conductivities to power densities, is injective and the data is noise-free. Moreover, we implemented the Levenberg-Marquardt algorithm and tested it on simulated data.

Keywords. Inverse problems, nonlinear ill-posed problems, iterative regularization, elliptic equations, hybrid imaging

AMS subject classifications. 35R30, 47J06, 35J47

4.1. Introduction

A common problem in *hybrid imaging* consists in the determination of the spatially varying conductivity $\sigma > 0$ in a domain $\Omega \subset \mathbb{R}^n$ from m measurements of power densities $\mathcal{E}_i(\sigma) = \sigma|\nabla u_i(\sigma)|^2$ $(i = 1, \dots, m)$ inside Ω (resulting from m different injected currents f_i). That is, the potentials u_i satisfy the elliptic equation

$$\begin{aligned} \operatorname{div}(\sigma \nabla u_i) &= 0 \text{ in } \Omega\,, \\ u_i &= f_i \text{ on } \partial\Omega. \end{aligned} \tag{4.1.1}$$

This problem is relevant, for example, in *Acousto-Electrical Tomography (AET)* [128, 9, 84] and *Impedance-Acoustic Tomography (IAT)* [62].

We investigate the solution of this nonlinear inverse problem in an infinite-dimensional setting. We apply the *Levenberg-Marquardt iteration* [67], a well-known iteration method which we recap in the next section. Using recent results about the linearized power density operator [18], we analyze local convergence conditions of the iteration method (for sufficiently smooth σ and noise-free data $\mathcal{E}_i$) and provide a partial result.

There are a number of theoretical results available on the problem of estimating σ from power densities (and some additional boundary information). In a paper by Capdeboscq et al. [40] it was shown that in $\mathbb{R}^2$, the conductivity σ is uniquely determined by measurements $\mathcal{F}(\sigma) = (\sigma|\nabla u_1|^2, \sigma|\nabla u_2|^2, \sigma\nabla u_1 \nabla u_2)$ if

$$\det(\nabla u_1, \nabla u_2) \geq c > 0 \quad \text{in } \Omega. \tag{4.1.2}$$

(certain Dirichlet boundary conditions are known to enforce this condition, see [5]). Note that $\sigma\nabla u_1 \nabla u_2$ can easily be obtained from a third measurement of the power density using the polarization identity. [20] extended this result to $\mathbb{R}^3$ and [25] to arbitrary dimension (where the above determinant condition (4.1.2) is much harder to fulfil) and additionally showed Lipschitz-stability of the reconstruction for sufficiently regular conductivities. Using the same interior measurements as above, Lipschitz-stability of the linearized problem $F'(\sigma)\colon L^2(\Omega) \to L^2(\Omega)$ (where $\sigma \in C^\infty(\Omega)$ and $\Omega \subset \mathbb{R}^2$) modulo the kernel of the linearized power density operator was shown by Kuchment and Steinhauer [86]. What may be reconstructed in the setting of only *one* measurement $\sigma|\nabla u|^2$ is analyzed in [19].

Numerically, the problem has been treated in [9, 62, 40, 85, 24].

The paper is organized as follows: First, we introduce the *Levenberg-Marquardt iteration* and its convergence conditions. Then, we linearize the power density operator $\mathcal{E}$ with Dirichlet boundary conditions in a suitable topology, analyse its stability and injectivity and discuss convergence of the iteration method. In the last two sections, we describe our numerical implementation of the Levenberg-Marquardt method and present numerical results.

4.2. Iterative solution scheme

4.2.1. The Levenberg-Marquardt iteration

Let us denote by $\boldsymbol{\mathcal{E}}^\delta = (\mathcal{E}_i^\delta)_{i=1,\dots,m}$ the (noisy) measurements according to m different initializations. We want find σ such that $\boldsymbol{\mathcal{E}}(\sigma) \approx \boldsymbol{\mathcal{E}}^\delta$. To solve, we use an iterative regularization method in a Hilbert space setting. In [76, 77, 75] several such methods for solving a general operator equation $F(\sigma) \approx y^\delta$, where $F\colon X \to Y$ and X, Y are Hilbert spaces, are given. We use a Newton-type method, since these methods are usually converging faster than pure gradient descent methods. Newton's method itself is defined by

$$\sigma_{k+1} = \sigma_k + F'(\sigma_k)^{-1}(y^\delta - F(\sigma_k)) \, .$$

If the operator $F'(\sigma_k)$ is not left-invertible (this can be the case for $\boldsymbol{\mathcal{E}}(\sigma)$ if there are not enough measurements, as we shall see in the next sections) one may use Tikhonov regularization:

$$\sigma_{k+1} = \arg\min_\sigma \left\{ \left\| y - F(\sigma_k) - F'(\sigma_k)(\sigma - \sigma_k) \right\|_Y^2 + \alpha_k \left\| \sigma - \sigma_k \right\|_X^2 \right\} .$$

The resulting iteration method

$$\sigma_{k+1} = \sigma_k + (F'(\sigma_k)^* F'(\sigma_k) + \alpha_k \,\mathrm{Id})^{-1} F'(\sigma_k)^* (y^\delta - F(\sigma_k)), \tag{4.2.1}$$

where $\alpha_k > 0$ are regularization parameters, is called the *Levenberg-Marquardt method.*

Hanke [67] suggests choosing α_k as the solutions of

$$\left\| y^\delta - F(\sigma_k) - F'(\sigma_k)(\sigma_{k+1}(\alpha_k) - \sigma_k) \right\|_Y = q \left\| y^\delta - F(\sigma_k)) \right\|_Y \tag{4.2.2}$$

for some $0 < q < 1$. He shows that with the above choice of parameters and the initial value σ_0 sufficiently close to the desired solution, the Levenberg-Marquardt method converges monotonically to a solution σ^δ of $F(\sigma^\delta) = y^\delta$, provided the Fréchet derivative F' is uniformly bounded in a ball $B_\rho(\sigma^\delta)$ containing the initial value σ_0 and

$$\left\| F(\sigma) - F(\tilde\sigma) - F'(\sigma)(\sigma - \tilde\sigma) \right\|_Y \le C \left\| \sigma - \tilde\sigma \right\|_X \left\| F(\sigma) - F(\tilde\sigma) \right\|_Y \tag{4.2.3}$$

for all $\sigma, \tilde\sigma \in B_\rho(\sigma^\delta)$.

4.2.2. Linearization

We now prove Fréchet differentiability of the power density operator $\mathcal{E}(\sigma) = \mathrm{div}(\sigma \nabla u)$ (where u solves (4.1.1) for some boundary condition $f = f_i$).

Let $\Omega \subset \mathbb{R}^n$. We assume that σ is positive and in the space $H^l(\Omega)$ for $l > \frac{n}{2}$, which implies that $H^l(\Omega)$ is a Banach algebra with respect to pointwise multiplication [1]. For $f \in H^{l+\frac{1}{2}}(\partial\Omega)$, (4.1.1) then has a unique solution $u(\sigma) \in H^{l+1}(\Omega)$ [107], so $\mathcal{E}\colon H^l(\Omega) \to H^l(\Omega)$.

Let $L_\sigma\colon H^l \to H^{l-2}, f \mapsto \operatorname{div}(\sigma\nabla f)$. By formal differentiation one can see that the directional derivative $u'(\sigma)\tau$ is given by

$$\begin{aligned} L_\sigma u'(\sigma)\tau &= -\operatorname{div}(\tau\nabla u) \quad \text{in } \Omega \\ u'(\sigma)\tau &= 0 \quad \text{on } \partial\Omega. \end{aligned} \tag{4.2.4}$$

Obviously, $u'(\sigma)\colon H^l(\Omega) \to H^{l+1}(\Omega)$ is linear with respect to τ. It is also bounded for the given norms considering

$$\|u'(\sigma)\tau\|_{H^{l+1}(\Omega)} \leq C\,\|\operatorname{div}(\tau\nabla u)\|_{H^{l-1}(\Omega)} \leq C\,\|\tau\|_{H^l(\Omega)}\,\|u\|_{H^{l+1}(\Omega)}\,. \tag{4.2.5}$$

Here we used the regularity estimates in [107] for the first and the Banach algebra property for the last inequality. Since the constant in the regularity estimates is a bounded function of σ if σ is bounded from below (e.g., in a sufficiently small ball around the solution), $u'(\sigma)$ is actually uniformly bounded there. Now, let $R_u(\sigma,\tau) = u(\sigma+\tau) - u(\sigma) - u'(\sigma)\tau$ be the first order Taylor remainder of u. For small τ we get

$$L_{\sigma+\tau}R_u(\sigma,\tau) = -L_\tau u'(\sigma)\tau \quad \text{in } \Omega.$$

As in (4.2.5) we obtain

$$\begin{aligned} \|R_u(\sigma,\tau)\|_{H^{l+1}(\Omega)} &\leq C\,\|L_\tau u'(\sigma)\tau\|_{H^{l-1}(\Omega)} \\ &\leq C\,\|\tau\|_{H^l(\Omega)}\,\|u'(\sigma)\tau\|_{H^{l+1}(\Omega)} \leq C\,\|\tau\|^2_{H^l(\Omega)} \end{aligned} \tag{4.2.6}$$

since $u'(\sigma)$ is bounded. This shows that $u'(\sigma)$ as defined in (4.2.4) is actually the Fréchet derivative of $u\colon H^l(\Omega) \to H^{l+1}(\Omega)$.

For the power density operator $\mathcal{E}\colon H^l(\Omega) \to H^l(\Omega),\ \sigma \mapsto \sigma|\nabla u(\sigma)|^2$, formal differentiation gives the directional derivative

$$\mathcal{E}'(\sigma)\tau = |\nabla u|^2\tau + 2\sigma\nabla u\nabla u'(\sigma)\tau,$$

Its uniform boundedness follows from the uniform boundedness of $u'(\sigma)$ and the Banach algebra property of $H^l(\Omega)$.

For the first order Taylor remainder $R_{\mathcal{E}}(\sigma,\tau)$, we get

$$\begin{aligned} R_{\mathcal{E}}(\sigma,\tau) &:= \mathcal{E}(\sigma+\tau) - \mathcal{E}(\sigma) - \mathcal{E}'(\sigma)\tau \\ &= (\sigma+\tau)|\nabla(u + u'(\sigma)\tau + R_u(\sigma,\tau))|^2 - \sigma|\nabla u|^2 \\ &- |\nabla u|^2\tau - 2\sigma\nabla u\nabla u'(\sigma)\tau \\ &= (\sigma+\tau)\nabla(2u + 2u'(\sigma)\tau + R_u(\sigma,\tau))\nabla R_u(\sigma,\tau) \\ &+ (\sigma+\tau)|\nabla u'(\sigma)\tau|^2 + 2\tau\nabla u\nabla u'(\sigma)\tau. \end{aligned}$$

Now, by (4.2.6) and (4.2.5)

$$\begin{aligned}\|R_{\mathcal{E}}(\sigma,\tau)\|_{H^l(\Omega)} &\le C(\|R_u(\sigma,\tau)\|_{H^{l+1}(\Omega)} + \|\tau\|^2_{H^l(\Omega)} + \|\tau\|^2_{H^l(\Omega)}) \\ &\le C\,\|\tau\|^2_{H^l(\Omega)}\end{aligned} \tag{4.2.7}$$

so $\|R_{\mathcal{E}}(\sigma,\tau)\|_{H^l(\Omega)} = o(\|\tau\|_{H^l(\Omega)})$, showing that $\mathcal{E}'(\sigma)$ is the Fréchet derivative of $\mathcal{E}\colon H^l(\Omega) \to H^l(\Omega)$ at σ.

4.2.3. Stability and injectivity

In this section, we recap stability and injectivity of the linearized operator, following the treatment in [18].

We may write the linearization of $\boldsymbol{\mathcal{E}}\colon H^l(\Omega) \to H^l(\Omega;\mathbb{R}^m), \sigma \mapsto (\mathcal{E}_i)_{i=1,\dots,m}$ as the following system:

$$\begin{aligned}\nabla\cdot\delta\sigma\nabla u_i + \nabla\cdot\sigma\nabla\delta u_i &= 0 \\ \delta\sigma|\nabla u_i|^2 + 2\sigma\nabla u_i\cdot\nabla\delta u_i &= \delta\mathcal{E}_i\end{aligned} \tag{4.2.8}$$

The last line provides the Fréchet derivative $\delta\mathcal{E}_i = d\mathcal{E}_i\cdot\delta\sigma$ seeing $\delta u_i = du_i\cdot\delta\sigma$ as a function of $\delta\sigma$ given by solving the first line with Dirichlet conditions.

Ellipticity. Let us assume as before that σ and ∇u_i are in the space $H^l(\Omega)$ for $l > \frac{n}{2}$. Then Dirichlet conditions for δu_i render the above system elliptic provided that $q_i(x,\xi) = 0$ for all $1 \le j \le m$ implies $\xi = 0$, where

$$q_i(x,\xi) = 2(\hat{F}_i\cdot\xi)^2 - |\xi|^2, \qquad \hat{F}_i = \frac{\nabla u_i}{|\nabla u_i|}.$$

This theory is independent of dimension and is based on the theory of elliptic redundant systems of equations with boundary conditions satisfying the Lopatinskii conditions; see [18, 107]. Similar ellipticity conditions are found in [86]. From such a theory, we obtain for $s = l$ with $l > \frac{n}{2}$, and coefficients $\sigma \in H^s(\Omega)$ and $u_i \in H^{s+1}(\Omega)$, the following stability estimate

$$\begin{aligned}&\|\delta\sigma - \delta\tilde{\sigma}\|_{H^s(\Omega)} + \|\delta\mathbf{u} - \delta\tilde{\mathbf{u}}\|_{H^{s+1}(\Omega;\mathbb{R}^m)} \\ &\qquad \le C\|\delta\boldsymbol{\mathcal{E}} - \delta\tilde{\boldsymbol{\mathcal{E}}}\|_{H^s(\Omega;\mathbb{R}^m)} + C_2\|\delta\mathbf{u} - \delta\tilde{\mathbf{u}}\|_{L^2(\Omega;\mathbb{R}^m)}.\end{aligned} \tag{4.2.9}$$

Here, $\delta\boldsymbol{\mathcal{E}}$ is the collection of terms $\delta\,\mathcal{E}_i$ and $\delta\mathbf{u}$ the collection of δu_i. The presence of the term with C_2 indicates the fact that the systems may not be invertible. Rather, it is Fredholm, and hence invertible up to a finite dimensional kernel of (smooth) functions. This is reminiscent of the behavior of $\Delta + q(x)$, which is invertible up to a finite dimensional kernel, although it is invertible (with Dirichlet conditions) for most values of $q(x)$.

Injectivity of modified systems. Whether we can choose $C_2 = 0$ above is not known in general. Injectivity results are known in the presence of more measurements than necessary for ellipticity; see, e.g., [85] in the linearized setting and [20, 25] in the nonlinear setting.

In the setting of two measurements in dimension $n = 2$ and three measurements in dimension $n = 3$, results of injectivity were obtained in [18] for modified systems of equations. Let denote by $v = (\delta\sigma, \{\delta u_i\})$ and recast the system (4.2.8) as

$$\mathcal{A}v = \mathcal{S}.$$

Then assuming that full Cauchy data are known for v on $\partial\Omega$, we may replace the above system by

$$\mathcal{A}^t\mathcal{A}v = \mathcal{A}^t\mathcal{S} \quad \text{in } \Omega, \qquad v = \partial_\nu v = 0 \text{ on } \partial\Omega. \tag{4.2.10}$$

This system was proved in [18] to admit a unique solution on sufficiently small domains; in other words, (4.2.9) holds with $C_2 = 0$.

A different modification of (4.2.8) also leading to a fourth-order system similar to (4.2.10) is also proved to be injective; see [18, Equation (35)].

These systems are difficult to implement numerically. We therefore wish to solve the system as written in (4.2.8). Knowing that very similar systems are indeed shown to be injective in the aforementioned work, it seems reasonable to assume that $C_2 = 0$ in (4.2.9) for m large enough, i.e., that the linearized operator $\mathcal{A}$ is left-invertible. With this assumption, we get that $d\boldsymbol{\mathcal{E}}$ is an operator from $H^s(\Omega)$ to $H^s(\Omega;\mathbb{R}^m)$ with a bounded left-inverse when $s > \frac{n}{2}$.

We then obtain an optimal stability estimate of the form

$$C_s^{-1}\|\delta\sigma - \delta\tilde{\sigma}\|_{H^s(\Omega)} \leq \|\delta\boldsymbol{\mathcal{E}} - \delta\tilde{\boldsymbol{\mathcal{E}}}\|_{H^s(\Omega;\mathbb{R}^m)} \leq C_s\|\delta\sigma - \delta\tilde{\sigma}\|_{H^s(\Omega)}. \tag{4.2.11}$$

4.2.4. Convergence analysis

In this section, we analyse whether the convergence conditions given in section 4.2.1 can be shown to hold for the power density operator $\boldsymbol{\mathcal{E}}\colon H^l(\Omega) \to H^l(\Omega;\mathbb{R}^m)$ with a suitable number of measurements m. Note that we require noise-free data here (the noise cannot be assumed to fulfil differentiability constraints).

To get local convergence of the Levenberg-Marquardt iteration, it suffices to show that (4.2.3) holds (we already saw that the operator is uniformly bounded close to a solution). Given Lipschitz-type stability, i.e.,

$$\|\sigma_1 - \sigma_2\|_{H^l(\Omega)} \leq C' \left\|\boldsymbol{\mathcal{E}}(\sigma_1) - \boldsymbol{\mathcal{E}}(\sigma_2)\right\|_{H^l(\Omega;\mathbb{R}^m)}, \tag{4.2.12}$$

the estimate (4.2.3) can easily be obtained from (4.2.7).

Using the stability estimates (4.2.11) for the linearized operator, we can get such an estimate locally, since for $\sigma_1, \sigma_2 \in B_\rho(\sigma^\delta)$ (a ball with sufficiently small diameter in the $H^l(\Omega)$-norm) we have

$$\begin{aligned} C' \left\|\sigma_2 - \sigma_1\right\|_{H^l(\Omega)} &\leq C_s^{-1} \left\|\sigma_2 - \sigma_1\right\|_{H^l(\Omega)} - C \left\|\sigma_2 - \sigma_1\right\|^2_{H^l(\Omega)} \\ &\leq \left\|\boldsymbol{\mathcal{E}}'(\sigma_1)(\sigma_1 - \sigma_2)\right\|_{H^l(\Omega;\mathbb{R}^m)} - C \left\|\sigma_2 - \sigma_1\right\|^2_{H^l(\Omega)} \\ &\leq \left\|\boldsymbol{\mathcal{E}}(\sigma_2) - \boldsymbol{\mathcal{E}}(\sigma_1)\right\|_{H^l(\Omega;\mathbb{R}^m)} \end{aligned}$$

by using norm equivalence for the second inequality and

$$\left\|\boldsymbol{\mathcal{E}}'(\sigma_1)(\sigma_2 - \sigma_1)\right\|_{H^l(\Omega;\mathbb{R}^m)} - \left\|\boldsymbol{\mathcal{E}}(\sigma_2) - \boldsymbol{\mathcal{E}}(\sigma_1)\right\|_{H^l(\Omega;\mathbb{R}^m)} \leq C \left\|\sigma_2 - \sigma_1\right\|^2_{H^l(\Omega)},$$

which is obtained by applying the reverse triangle inequality to (4.2.7), for the third estimate.

From (4.2.7) we finally get

$$\left\|R_{\boldsymbol{\mathcal{E}}}(\sigma, \tau)\right\|_{H^l(\Omega;\mathbb{R}^m)} \leq C \left\|\tau\right\|_{H^l(\Omega)} \left\|\boldsymbol{\mathcal{E}}(\sigma + \tau) - \boldsymbol{\mathcal{E}}(\sigma)\right\|_{H^l(\Omega;\mathbb{R}^m)}. \tag{4.2.13}$$

for sufficiently small τ. Applying the general results in [67] now gives us local convergence (in the noise-free case) of the Levenberg-Marquardt iteration applied to $\boldsymbol{\mathcal{E}} \colon H^l(\Omega) \to H^l(\Omega; \mathbb{R}^m)$.

Note that for the stability estimate (4.2.11) we assumed injectivity of (4.2.8) (and thus $\mathcal{E}'(\sigma)$). For one measurement, this may not hold, for example, it is easily seen that if Ω is the unit circle in $\mathbb{R}^2$, the boundary voltage $f(x, y) = ax + by$ (where $\binom{a}{b}$ is a unit vector) and $\sigma = 1$, the function f (with corresponding linearized potential $(u'(\sigma)f)(x, y) = -\frac{1}{4}(x^2 + y^2) + \frac{1}{4}$) is in $\operatorname{Ker} \mathcal{E}'(\sigma)$; see also [19].

Generically, one may however expect injectivity to hold if enough data are available.

4.3. Numerical solution

The following sections contain some numerical work to demonstrate the feasibility of our ideas. For simplicity, we work in two dimensions, so we take $\Omega \subset \mathbb{R}^2$. Furthermore, we now allow the presence of noise. As noise cannot be assumed to be differentiable, we have to consider (in contrast to the previous section) the power density operator to map into $L^2(\Omega)$. Since $l = 2$ is the smallest integer for which $H^l(\Omega)$ is a Banach algebra, we take $\mathcal{E} \colon H^2(\Omega) \to L^2(\Omega)$.

4.3.1. Calculation of the adjoint

For the iterative algorithm, we require an expression for the adjoint of $\mathcal{E}'(\sigma)$, which we now derive.

First, we consider the case $m = 1$ of a single measurement. Larger values of m are treated with an additional summation. Since $\mathcal{E}'(\sigma)\colon H^2(\Omega) \to L^2(\Omega)$ is a bounded operator, we know that $\mathcal{E}'(\sigma)^*\colon L^2(\Omega) \to H^2(\Omega)$ is bounded as well (see [118]).

First note that the adjoint operator of $\mathcal{E}'(\sigma)\colon H^2(\Omega) \to L^2(\Omega)$ can be written as

$$\begin{aligned}
&\mathcal{E}'(\sigma)^*\colon L^2(\Omega) \to H^2(\Omega) \\
&\mathcal{E}'(\sigma)^* z = i^* \tilde{\mathcal{E}}'(\sigma)^* z,
\end{aligned}$$

where $\tilde{\mathcal{E}}'(\sigma)^*$ is the $L^2(\Omega)$-adjoint of $\mathcal{E}(\sigma)$ and i^* the adjoint of the embedding $i\colon H^2(\Omega) \to L^2(\Omega)$.

We start by finding an expression for $\tilde{\mathcal{E}}'(\sigma)^*$ on $H^2(\Omega) \subset L^2(\Omega)$. Let $V = V(\sigma, u(\sigma))$ with $V\colon H^2(\Omega) \to H_0^2(\Omega)$ be the linear operator defined by

$$\begin{aligned}
L_\sigma V z &= -\operatorname{div}(z\sigma\nabla u(\sigma)) \quad \text{in } \Omega \\
V z &= 0 \quad \text{in } \partial\Omega.
\end{aligned}$$

Note that $z\sigma$ is also in $H^2(\Omega)$, so V is mapped into $L^2(\Omega)$.

For $z \in H^2$ we now get that for the second summand of $\mathcal{E}'(\sigma)$

$$\begin{aligned}
\langle \sigma\nabla u \nabla u'(\sigma)\tau, z\rangle_{L^2(\Omega)} &= -\langle \sigma\nabla u'(\sigma)\tau, \nabla V z\rangle_{L^2(\Omega;\mathbb{R}^2)} \\
&= \langle \tau, \nabla u \nabla V z\rangle_{L^2(\Omega)}
\end{aligned}$$

by partial integration and the definitions of V and $u'(\sigma)$. Since the first summand is self-adjoint, we conclude

$$\begin{aligned}
&\mathcal{E}'(\sigma)^*\colon H^2(\Omega) \to H^2(\Omega) \\
&\mathcal{E}'(\sigma)^* z = i^*(|\nabla u(\sigma)|^2 z + 2\nabla u(\sigma)\nabla V z)\ .
\end{aligned} \tag{4.3.1}$$

As $\mathcal{E}'(\sigma)^*$ is bounded on $L^2(\Omega)$, (4.3.1) can be continuously extended to $w \in L^2(\Omega)$, e.g., by taking $\mathcal{E}'(\sigma)^* w := \lim_{\epsilon\to 0} \mathcal{E}'(\sigma)^* \Phi_\epsilon w$ where $\Phi_\epsilon w = \phi_\epsilon * w$ is the mollification operator corresponding to some mollifier ϕ.

For $\boldsymbol{\mathcal{E}}\colon H^2(\Omega) \to L^2(\Omega;\mathbb{R}^m)$, $\sigma \mapsto (\mathcal{E}_i)_{i=1}^m$ we similarly get (with $V_j = V(\sigma, u_j(\sigma))$),

$$\begin{aligned}
&\boldsymbol{\mathcal{E}}'(\sigma)^*\colon H^2(\Omega;\mathbb{R}^2) \to H^2(\Omega) \\
&\boldsymbol{\mathcal{E}}'(\sigma)^* z = i^* \sum_{j=1}^m |\nabla u_j(\sigma)|^2 z_j + 2\nabla u_j(\sigma)\cdot\nabla V_j w_j\ .
\end{aligned} \tag{4.3.2}$$

$\boldsymbol{\mathcal{E}}'$ can also be continuously extended to $L^2(\Omega;\mathbb{R}^2)$ by mollifying and taking the limit.

To calculate $i^*\colon L^2(\Omega) \to H^2(\Omega)$ we make the additional assumption that $\sigma \in H_N^2(\Omega) = \{x \in H^2(\Omega) | \frac{\partial x}{\partial\nu} = 0\}$, a closed subspace of $H^2(\Omega)$ since $(\frac{\partial}{\partial\nu}\circ\text{trace})\colon H^2(\Omega) \to L^2(\partial\Omega)$ is bounded.

With the inner product

$$\langle x, y\rangle_{H^2_N(\Omega)} = \langle x, y\rangle_{L^2(\Omega)} + \beta^2 \langle \Delta x, \Delta y\rangle_{L^2(\Omega)}$$

for some $\beta > 0$, i^*y is the solution of the Neumann problem

$$\begin{aligned}(\mathrm{Id} + \beta^2\Delta\Delta)i^*y &= y\\ \frac{\partial \Delta i^* y}{\partial \nu} &= 0 \text{ on } \partial\Omega\\ \frac{\partial i^* y}{\partial \nu} &= 0 \text{ on } \partial\Omega.\end{aligned} \tag{4.3.3}$$

since for all $x \in H^2_N(\Omega)$, $y \in L^2(\Omega)$ we get that

$$\begin{aligned}\langle x, i^*y\rangle_{H^2_N(\Omega)} &= \langle x, i^*y\rangle_{L^2(\Omega)} + \beta^2 \langle \Delta x, \Delta i^* y\rangle_{L^2(\Omega)}\\ &= \left\langle x, (\mathrm{Id} + \beta^2\Delta\Delta)i^*y\right\rangle_{L^2(\Omega)} + \beta^2 \int_{\partial\Omega} \frac{\partial x}{\partial \nu}\Delta i^* y - \frac{\partial \Delta i^* y}{\partial \nu} x \; dS\\ &= \langle x, y\rangle_{L^2(\Omega)} = \langle ix, y\rangle_{L^2(\Omega)}.\end{aligned}$$

The fourth order PDE (4.3.3) is equivalent to the system of second order equations

$$\begin{aligned}i^*y + \beta^2\Delta z &= y\\ \Delta i^* y - z &= 0\\ \frac{\partial z}{\partial \nu} &= 0 \text{ on } \partial\Omega\\ \frac{\partial i^* y}{\partial \nu} &= 0 \text{ on } \partial\Omega.\end{aligned} \tag{4.3.4}$$

For a cruder approximation (which should give a faster solution), we could use H^1 or L^2 adjoints (where we have $i = i^* = \mathrm{Id}$). For the inner product $\langle x, y\rangle_{H^1(\Omega)} = \langle x, y\rangle_{L^2(\Omega)} + \beta \langle \nabla x, \nabla y\rangle_{L^2(\Omega)}$, the adjoint of $\tilde{i} \colon H^1(\Omega) \to L^2(\Omega; \mathbb{R}^2)$ (by a proof similar to the above) maps $y \in L^2(\Omega)$ to the solution of

$$\begin{aligned}(\mathrm{Id} - \beta^2\Delta)\tilde{i}^* y &= y\\ \frac{\partial \tilde{i}^* y}{\partial \nu} &= 0 \text{ on } \partial\Omega.\end{aligned} \tag{4.3.5}$$

4.3.2. Implementation

For $F = \mathcal{E}$ with a given (single) measurement $\mathcal{E}^\delta$, the equation (4.2.1) for the k-th Levenberg-Marquardt step τ_k reads

$$(\lim_{\epsilon\to 0} i^* M_\epsilon + \alpha_k \,\mathrm{Id})\tau_k = \mathcal{E}'(\sigma_k)^*(\mathcal{E}^\delta - \mathcal{E}(\sigma_k)) \tag{4.3.6}$$

where, with $u = u(\sigma_k)$, $\alpha_k = \alpha$, $\tau = \tau_k$ and $\sigma = \sigma_k$,

$$\begin{aligned} M_\epsilon \tau = |\nabla u|^2 \Phi_\epsilon(|\nabla u|^2 \tau + 2\sigma \nabla u \nabla u'(\sigma)\tau) \\ + 2\nabla u \nabla V \Phi_\epsilon(\tau |\nabla u|^2) + 4\nabla u \nabla V \Phi_\epsilon(\sigma \nabla u \nabla u'(\sigma)\tau). \end{aligned}$$

Now, let ϵ be fixed. By introducing auxiliary variables z^1, z^2, z^3 and y^1, y^2, y^3 (for expressions which are a solution of a PDE) and using (4.3.4), equation (4.3.6) can be written as

$$\begin{aligned}
& z^3 + \alpha\tau_\epsilon = \mathcal{E}'(\sigma)^*(\mathcal{E}^\delta - \mathcal{E}(\sigma)) \\
& \Delta z^3 - z^2 = 0, && \partial z^3/\partial\nu = 0 \text{ on } \partial\Omega \\
& \beta^2 \Delta z^2 + z^3 - z^1 = 0, && \partial z^2/\partial\nu = 0 \text{ on } \partial\Omega \\
& |\nabla u|^2 \Phi_\epsilon(|\nabla u|^2 \tau_\epsilon + 2\sigma \nabla u \nabla y^1) + 2\nabla u \nabla y^2 + 4\nabla u \nabla y^3 - z^1 = 0 \\
& \operatorname{div}(\Phi_\epsilon(\sigma \nabla u \nabla y^1)\sigma \nabla u) + L_\sigma y^3 = 0, && y^3 = 0 \text{ on } \partial\Omega \\
& \operatorname{div}(\Phi_\epsilon(\tau_\epsilon |\nabla u|^2)\sigma \nabla u) + L_\sigma y^2 = 0, && y^2 = 0 \text{ on } \partial\Omega \\
& \operatorname{div}(\tau_\epsilon \nabla u) + L_\sigma y^1 = 0, && y^1 = 0 \text{ on } \partial\Omega
\end{aligned} \tag{4.3.7}$$

We then obtain τ_k in (4.3.6) from τ_ϵ by letting $\epsilon \to 0$ (for numerical purposes the continuous extension, i.e., the mollification and the limit can be ignored, as it leaves the discretization unchanged in the limit $\epsilon \to 0$). Since its discretization does not contain inverse matrices (and thus can be solved using sparse matrix operations only), the system (4.3.7) is more amenable to numerical treatment than discretizing (4.3.6) directly. When using L^2 or H^1 adjoints, similar (smaller) systems can be generated.

For multiple measurements $\boldsymbol{\mathcal{E}}$, using the exact same approach leads to the system

$$\begin{aligned}
& z^3 + \alpha\tau_\epsilon = \boldsymbol{\mathcal{E}}'(\sigma)^*(\boldsymbol{\mathcal{E}}^\delta - \boldsymbol{\mathcal{E}}(\sigma)) \\
& \Delta z^3 - z^2 = 0, && \partial z^3/\partial\nu = 0 \text{ on } \partial\Omega \\
& \beta^2 \Delta z^2 + z^3 - z^1 = 0, && \partial z^2/\partial\nu = 0 \text{ on } \partial\Omega \\
& \sum_{j=1}^m |\nabla u_j|^2 \Phi_\epsilon(|\nabla u_j|^2 \tau_\epsilon + 2\sigma \nabla u_j \nabla y_j^1) + 2\nabla u_j \nabla y_j^2 + 4\nabla u_j \nabla y_j^3 - z^1 = 0 \\
& \operatorname{div}(\Phi_\epsilon(\sigma \nabla u_j \nabla y_j^1)\sigma \nabla u_j) + L_\sigma y_j^3 = 0, && y_j^3 = 0 \text{ on } \partial\Omega \\
& \operatorname{div}(\Phi_\epsilon(\tau_\epsilon |\nabla u_j|^2)\sigma \nabla u_j) + L_\sigma y_j^2 = 0, && y_j^2 = 0 \text{ on } \partial\Omega \\
& \operatorname{div}(\tau_\epsilon \nabla u_j) + L_\sigma y_j^1 = 0, && y_j^1 = 0 \text{ on } \partial\Omega
\end{aligned} \tag{4.3.8}$$

so 3 equations (and auxiliary variables) have to be added per additional measurement. We again obtain τ_k from τ_ϵ by letting $\epsilon \to 0$.

4.4. Results

In our numerical solution we directly implemented the systems (4.3.7) and (4.3.8) to obtain Levenberg-Marquardt steps. For discretization of the partial differential equations we used a self-written linear finite elements framework in *MATLAB*. The triangular mesh (with 42849 nodes and 85007 elements) was created using *DistMesh* [97]. All calculations were done on a workstation computer.

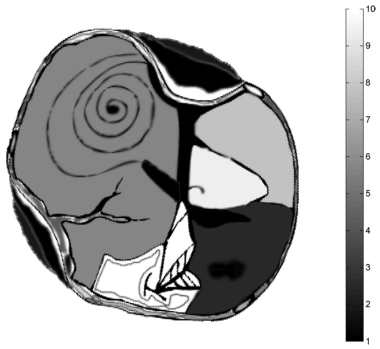

(a) Conductivity σ

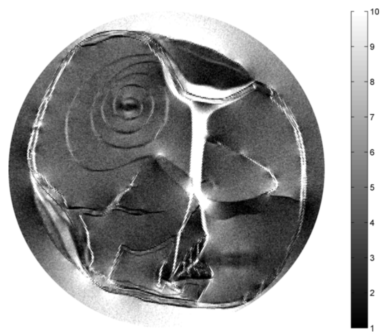

(b) Power density $\mathcal{E}_1^\delta$

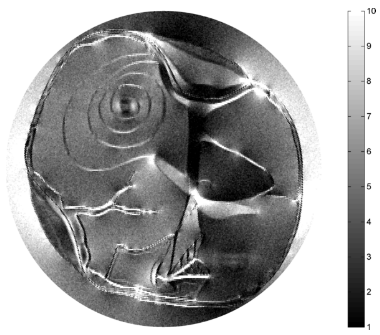

(c) Power density $\mathcal{E}_2^\delta$

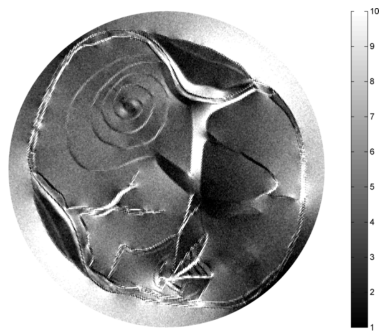

(d) Power density $\mathcal{E}_3^\delta$

Figure 4.1.: Conductivity and simulated measurements with boundary conditions $f_1(x,y) = x$, $f_2(x,y) = y$ and $f_3(x,y) = \frac{1}{\sqrt{2}}(x-y)$ and Gaussian noise. The color axis was manually set to 1-10, the range of σ.

To test the reconstruction algorithm, we generated simulated data $\boldsymbol{\mathcal{E}}^\delta = (\mathcal{E}_1^\delta, \mathcal{E}_2^\delta, \mathcal{E}_3^\delta)$ on the unit circle with the boundary conditions $f_1(x,y) = x$, $f_2(x,y) = y$ and $f_3(x,y) = \frac{1}{\sqrt{2}}(x-y)$ (and added Gaussian noise with standard deviation 1 to avoid an inverse crime).

For reconstruction, we set $\sigma_0 \equiv 1$, $\beta = 10^{-3}$ and chose $\alpha_k = \frac{1}{2^k}$ (with a minimum of 10^{-8}) a priori. Choosing α_k according to the criterion (4.2.2) would be possible (e.g., by reducing α_k until the condition is met), but numerically expensive.

Note that for two or more measurements, regularization is technically is not necessary since the operator can be assumed to be invertible (the linearized and discretized equations were solvable with $\alpha_k = 0$ in all instances we tested), but advantageous for the iteration scheme since it helps ensure that iterates remain in a trust region and thus feasible (i.e., positive). Additionally, we enforce a minimal conductivity of 10^{-12} on the iterates.

We used the standard *MATLAB* sparse solver *mldivide* to solve the linearized and discretized equations.

The results of our numerical experiments seen in Figures 4.2 and 4.3 show that from 2 measurements, even in the presence of significant noise, very good reconstructions are possible. The third measurement, which considerably increases the runtime, mostly serves to slightly reduce the noise. The H^1-approximation of the H^2 adjoint works well without loss of accuracy. The L^2-approximation, on the other hand, does not converge properly. From the difference images, we can see that in the main remaining error in the H^1 or H^2 reconstructions with 2 or more measurements is due to smoothing (which can be alleviated by running more iterations or lowering β).

While the given algorithms could in theory be directly translated to $\mathbb{R}^3$ (a higher degree of regularity would be necessary to get a Banach algebra and/or map into $L^2(\Omega)$), the drastically increased number of elements would make the computational effort for high-resolution reconstructions unreasonable. To reduce the effort, one could either switch to Landweber-like methods or use a combination of nested grids and iterative linear solvers as in [40].

(a) L^2 adjoints, data $\mathcal{E}_2^\delta$

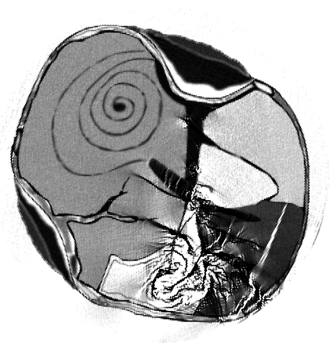

(b) L^2 adjoints, data $(\mathcal{E}_1^\delta, \mathcal{E}_3^\delta)$

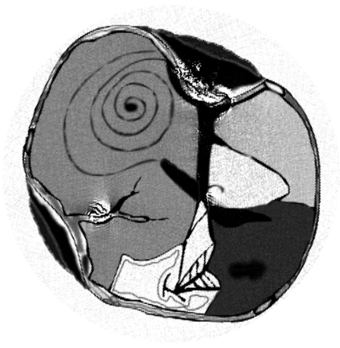

(c) L^2 adjoints, data $(\mathcal{E}_1^\delta, \mathcal{E}_2^\delta, \mathcal{E}_3^\delta)$

(d) H^1 adjoints, data $\mathcal{E}_2^\delta$

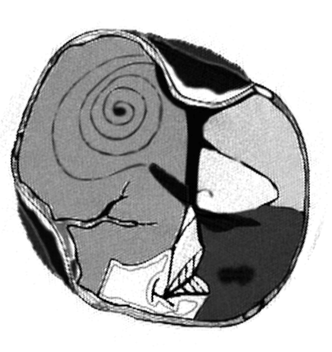

(e) H^1 adjoints, data $(\mathcal{E}_1^\delta, \mathcal{E}_3^\delta)$

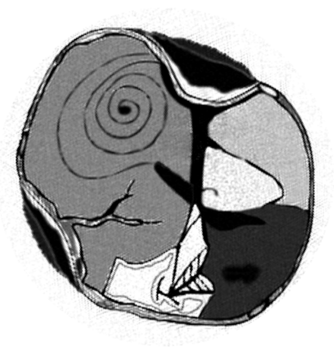

(f) H^1 adjoints, data $(\mathcal{E}_1^\delta, \mathcal{E}_2^\delta, \mathcal{E}_3^\delta)$

(g) H^2 adjoints, data $\mathcal{E}_2^\delta$

(h) H^2 adjoints, data $(\mathcal{E}_1^\delta, \mathcal{E}_3^\delta)$

(i) H^2 adjoints, data $(\mathcal{E}_1^\delta, \mathcal{E}_2^\delta, \mathcal{E}_3^\delta)$

Figure 4.2.: Reconstructed conductivities after 15 iterations of the Levenberg-Marquardt algorithm using different adjoints and one, two or three measurements. The color axis was manually set to 1-10, the range of the original conductivity to ease comparison.

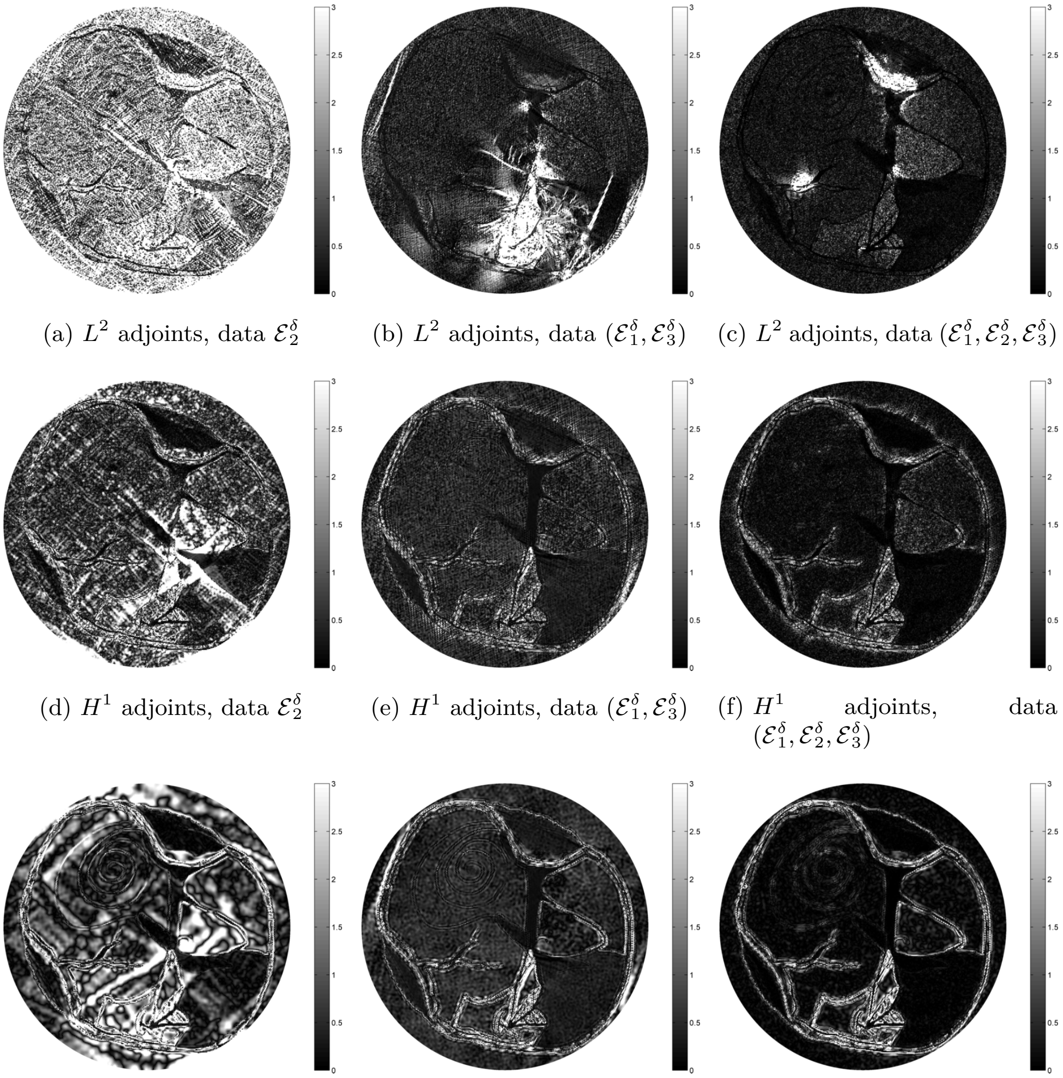

(a) L^2 adjoints, data $\mathcal{E}_2^\delta$ (b) L^2 adjoints, data $(\mathcal{E}_1^\delta, \mathcal{E}_3^\delta)$ (c) L^2 adjoints, data $(\mathcal{E}_1^\delta, \mathcal{E}_2^\delta, \mathcal{E}_3^\delta)$

(d) H^1 adjoints, data $\mathcal{E}_2^\delta$ (e) H^1 adjoints, data $(\mathcal{E}_1^\delta, \mathcal{E}_3^\delta)$ (f) H^1 adjoints, data $(\mathcal{E}_1^\delta, \mathcal{E}_2^\delta, \mathcal{E}_3^\delta)$

(g) H^2 adjoints, data $\mathcal{E}_2^\delta$ (h) H^2 adjoints, data $(\mathcal{E}_1^\delta, \mathcal{E}_3^\delta)$ (i) H^2 adjoints, data $(\mathcal{E}_1^\delta, \mathcal{E}_2^\delta, \mathcal{E}_3^\delta)$

Figure 4.3.: Difference images $|\sigma_{\text{est}} - \sigma|$ corresponding to the reconstructions in Figure 4.2. The color axis was manually set to 0-3.

4.5. Acknowledgements

This work has been supported by the Austrian Science Fund (FWF) within the national research networks Photoacoustic Imaging in Biology and Medicine (project S10505) and Geometry+Simulation (project S11704) and by the IK I059-N funded by the University of Vienna. GB acknowledges partial support from the National Science Foundation Grant DMS-1108608. John Schotland is supported by NSF grants DMS-1115574 and DMS-1108969.

Bibliography

[1] R. A. Adams. *Sobolev Spaces.* Academic Press, New York, 1975.

[2] M. Agranovsky and P. Kuchment. Uniqueness of reconstruction and an inversion procedure for thermoacoustic and photoacoustic tomography with variable sound speed. *Inverse Probl.*, 23(5):2089–2102, 2007.

[3] G. S. Alberti. On multiple frequency power density measurements. *Inverse Probl.*, 29(11):115007, 2013.

[4] G.S. Alberti and H. Ammari. Disjoint sparsity for signal separation and applications to hybrid inverse problems in medical imaging. preprint, ENS, 2015. http://arxiv.org/abs/1502.04540.

[5] G. Alessandrini and V. Nesi. Univalent σ-harmonic mappings. *Arch. Ration. Mech. Anal.*, 158(2):155–171, 2001.

[6] L. Ambrosio. A compactness theorem for a new class of functions of bounded variation. *Boll. Un. Mat. Ital. B*, 3:857–881, 1989.

[7] L. Ambrosio. Existence theory for a new class of variational problems. *Arch. Ration. Mech. Anal.*, 111:291–322, 1990.

[8] L. Ambrosio and V. M. Tortorelli. On the approximation of free discontinuity problems. *Boll. Un. Mat. Ital. B*, 6:105–123, 1992.

[9] H. Ammari, E. Bonnetier, Y. Capdeboscq, M. Tanter, and M. Fink. Electrical impedance tomography by elastic deformation. *SIAM J. Appl. Math.*, 68(6):1557–1573, 2008.

[10] H. Ammari, E. Bossy, V. Jugnon, and H. Kang. Reconstruction of the optical absorption coefficient of a small absorber from the absorbed energy density. *SIAM J. Appl. Math.*, 71(3):676–693, 2011.

[11] H. Ammari, J. Garnier, and W. Jing. Resolution and stability analysis in acousto-electric imaging. *Inverse Probl.*, 28(8):084005, 2012.

[12] H. Ammari, J. Garnier, W. Jing, and L.H. Nguyen. Quantitative thermoacoustic imaging: An exact reconstruction formula. *J. Differential Equations*, 254(3):1375–1395, 2013.

[13] R. Aronson. Boundary conditions for diffusion of light. *J. Opt. Soc. Amer. A*, 12(11):2532–2539, 1995.

[14] S. Arridge and O Scherzer. Imaging from coupled physics. *Inverse Probl.*, 28(8):080201, 2012.

[15] S. R. Arridge. Optical tomography in medical imaging. *Inverse Probl.*, 15(2):R41–R93, 1999.

[16] S. R. Arridge, O. Dorn, J. P. Kaipio, V. Kolehmainen, M. Schweiger, T. Tarvainen, M. Vauhkonen, and A. Zacharopoulos. Reconstruction of subdomain boundaries of piecewise constant coefficients of the radiative transfer equation from optical tomography data. *Inverse Probl.*, 22(6):2175–2196, 2006.

[17] H. Attouch, G. Buttazzo, and G. Michaille. *Variational Analysis in Sobolev and BV Spaces: Applications to PDEs and Optimization.* SIAM, Society for Industrial and Applied Mathematics, 2006.

[18] G. Bal. Hybrid inverse problems and systems of partial differential equations. *arXiv*, arXiv:1210.0265, 2012.

[19] G. Bal. Cauchy problem for ultrasound modulated EIT. *Anal. PDE*, 6(4):751–775, 2013.

[20] G. Bal, E. Bonnetier, F. Monard, and F. Triki. Inverse diffusion from knowledge of power densities. Preprint, Columbia University, 2011. http://arxiv.org/abs/1110.4577v1.

[21] G. Bal, E. Bonnetier, F. Monard, and F. Triki. Inverse diffusion from knowledge of power densities. *Inverse Probl. Imaging*, 7(2):353–375, 2013.

[22] G. Bal and M. Courdurier. Boundary control of elliptic solutions to enforce local constraints. *J. Differential Equations*, 255:1357–1381, 2013.

[23] G. Bal, A. Jollivet, and V. Jugnon. Inverse transport theory of photoacoustics. *Inverse Probl.*, 26(2):025011, 2010.

[24] G. Bal and F. Monard. Inverse anisotropic diffusion from power density measurements in two dimensions. *Inverse Probl.*, 28(8):084001, 2012.

[25] G. Bal and F. Monard. Inverse diffusion problem with redundant internal information. *Inverse Probl. Imaging*, 6(2):289–313, 2012.

[26] G. Bal and F. Monard. Inverse anisotropic conductivity from power densities in dimension n >= 3. *Comm. Partial Differential Equations*, 38(7):1183–1207, 2013.

[27] G. Bal, W. Naetar, O. Scherzer, and J. Schotland. The Levenberg-Marquardt iteration for numerical inversion of the power density operator. *J. Inverse Ill-Posed Probl.*, 21(2):265–280, February 2013. Funded by the Austrian Science Fund (FWF) within the FSP S105 - "Photoacoustic Imaging". Funded by the Austrian Science Fund (FWF) within the FSP S117 - "Geometry and Simulation". Funded by the University of Vienna within the Vienna Graduate School in Computational Science IK I059-N.

[28] G. Bal and K. Ren. Multi-source quantitative photoacoustic tomography in a diffusive regime. *Inverse Probl.*, 27(7):075003, 2011.

[29] G. Bal and K. Ren. Non-uniqueness result for a hybrid inverse problem. Preprint, Columbia University, 2011.

[30] G. Bal and K. Ren. On multi-spectral quantitative photoacoustic tomography in diffusive regime. *Inverse Probl.*, 28(2):025010, 2012.

[31] G. Bal, K. Ren, G. Uhlmann, and T. Zhou. Quantitative thermo-acoustics and related problems. *Inverse Probl.*, 27:055007, 2011.

[32] G. Bal and G. Uhlmann. Inverse diffusion theory of photoacoustics. *Inverse Probl.*, 26:085010, 2010.

[33] G. Bal and G. Uhlmann. Reconstructions for some coupled-physics inverse problems. *Appl. Math. Lett.*, 25(7):1030–1033, 2012.

[34] B. Banerjee, S. Bagchi, R.M. Vasu, and D. Roy. Quantitative photoacoustic tomography from boundary pressure measurements: noniterative recovery of optical absorption coefficient from the reconstructed absorbed energy map. *J. Opt. Soc. Amer. A*, 25(9):2347–2356, 2008.

[35] A. N. Bashkatov, E. A. Genina, and V. V. Tuchin. Optical properties of skin, subcutaneous, and muscle tissues: a review. *Journal of Innovative Optical Health Sciences*, 4(1):9–38, January 2011.

[36] E. Beretta and E. Francini. Lipschitz stability for the electrical impedance tomography problem: The complex case. *Comm. Partial Differential Equations*, 36(10):1723–1749, 2011.

[37] M. Bergounioux, X. Bonnefond, T. Haberkorn, and Y. Privat. An optimal control problem in photoacoustic tomography. *Math. Models Methods Appl. Sci.*, 24(12):2525, 2014.

[38] M. Burger and S. Osher. A survey on level set methods for inverse problems and optimal design. *European J. Appl. Math.*, 16(02):263–301, 2005.

[39] J.F. Canny. A computational approach to edge detection. *IEEE Trans. Pattern Anal. Mach. Intell.*, 8:679–697, 1986.

[40] Y. Capdeboscq, J. Fehrenbach, F. de Gournay, and O. Kavian. Imaging by modification: numerical reconstruction of local conductivities from corresponding power density measurements. *SIAM J. Imaging Sciences*, 2(4):1003–1030, 2009.

[41] T. Chan and L. Vese. Active contours without edges. *IEEE Trans. Image Process.*, 10(2):266–277, 2001.

[42] M. Cheney, D. Isaacson, and J. C. Newell. Electrical impedance tomography. *SIAM Rev.*, 41(1):85–101, 1999.

[43] B. T. Cox, S. R. Arridge, and P. C. Beard. Gradient-based quantitative photoacoustic image reconstruction for molecular imaging. *Proc. SPIE*, 6437:64371T, 2007.

[44] B. T. Cox, S. R. Arridge, and P. C. Beard. Estimating chromophore distributions from multiwavelength photoacoustic images. *J. Opt. Soc. Amer. A*, 26(2):443–455, 2009.

[45] B. T. Cox, S. R. Arridge, P. Köstli, and P. C. Beard. Two-dimensional quantitative photoacoustic image reconstruction of absorption distributions in scattering media by use of a simple iterative method. *App. Opt.*, 45(8):1866–1875, 2006.

[46] B. T. Cox, J. G. Laufer, S. R. Arridge, and P. C. Beard. Quantitative spectroscopic photoacoustic imaging: a review. *J. Biomed. Opt.*, 17(6):061202, 2012.

[47] B. T. Cox, J. G. Laufer, and P. C. Beard. The challenges for quantitative photoacoustic imaging. *Proc. SPIE*, 7177:717713, 2009.

[48] B. Dacorogna. *Direct methods in the calculus of variations*, volume 78 of *Applied Mathematical Sciences*. Springer, New York, 2 edition, 2008.

[49] A. De Cezaro, A. Leitao, and X. Tai. On multiple level-set regularization methods for inverse problems. *Inverse Probl.*, 25(3):035004, 2009.

[50] A. De Cezaro, F. Travessini De Cezaro, and J. Sejje Suarez. Regularization approaches for quantitative photoacoustic tomography using the radiative transfer equation. *J. Math. Anal. Appl.*, 429(1):415–438, 2015.

[51] E. De Giorgi, M. Carriero, and A. Leaci. Existence theorem for a minimum problem with free discontinuity set. *Arch. Ration. Mech. Anal.*, 108:195–218, 1989.

[52] V. Druskin. On the uniqueness of inverse problems from incomplete boundary data. *SIAM J. Appl. Math.*, 58(5):1591–1603, 1998.

[53] T. Durduran, R. Choe, W.B. Baker, and A.G. Yodh. Diffuse optics for tissue monitoring and tomography. *Rep. Prog. Phys.*, 73(7):076701, 2010.

[54] H. Egger and M. Schlottbom. Analysis and regularization of problems in diffuse optical tomography. *SIAM J. Math. Anal.*, 42(5):1934–âĂŞ1948, 2010.

[55] S. Esedoglu and J. Shen. Digital inpainting based on the Mumford–Shah–Euler image model. *European J. Appl. Math.*, 13:353–370, 2002.

[56] L. C. Evans. *Partial Differential Equations*, volume 19 of *Graduate Studies in Mathematics*. American Mathematical Society, Providence, RI, 1998.

[57] Q. Fang. Mesh-based monte carlo method using fast ray-tracing in plücker coordinates. *Biomed. Opt. Express*, 1(1):165–175, 2010.

[58] D. Finch, M. Haltmeier, and Rakesh. Inversion of spherical means and the wave equation in even dimensions. *SIAM J. Appl. Math.*, 68(2):392–412, 2007.

[59] D. Finch, S. Patch, and Rakesh. Determining a function from its mean values over a family of spheres. *SIAM J. Math. Anal.*, 35(5):1213–1240, 2004.

[60] S. Gabriel, R. W. Lau, and C. Gabriel. The dielectric properties of biological tissues: II. measurements in the frequency range 10 Hz to 20 GHz. *Phys. Med. Biol.*, 41:2251–69, 1996.

[61] H. Gao, S. Osher, and H. Zhao. Quantitative photoacoustic tomography. In *Mathematical Modeling in Biomedical Imaging II*, pages 131–158. Springer Berlin, Heidelberg, 2012.

[62] B. Gebauer and O. Scherzer. Impedance-acoustic tomography. *SIAM J. Appl. Math.*, 69(2):565–576, 2008.

[63] D. Gilbarg and N. Trudinger. *Elliptic Partial Differential Equations of Second Order*. Classics in Mathematics. Springer Verlag, Berlin, 2001. Reprint of the 1998 edition.

[64] D. Haemmerich, S. T. Stalin, J. Z. Tsai, S. Tungjitkusolmun, D. M. Mahvi, and J. G. Webster. In vivo electrical conductivitiy of hepatic tumours. *Physiol. Meas.*, 24:251–260, 2003.

[65] M. Haltmeier, L. Neumann, and S. Rabanser. Single-stage reconstruction algorithm for quantitative photoacoustic tomography. *Inverse Probl.*, 31(6):065005, 2015.

[66] M. Haltmeier, T. Schuster, and O. Scherzer. Filtered backprojection for thermoacoustic computed tomography in spherical geometry. *Math. Methods Appl. Sci.*, 28(16):1919–1937, 2005.

[67] M. Hanke. A regularizing Levenberg–Marquardt scheme, with applications to inverse groundwater filtration problems. *Inverse Probl.*, 13(1):79–95, 1997.

[68] B. Harrach. On uniqueness in diffuse optical tomography. *Inverse Probl.*, 28(5):055010, 2009.

[69] K. Hoffmann and K. Knudsen. Iterative reconstruction methods for hybrid inverse problems in impedance tomography. *Sens. Imaging*, 15(1), 2014.

[70] R. A. Horn and C. R. Johnson. *Matrix Analysis*. Cambridge University Press, Cambridge, 1990. Corrected reprint of the 1985 original.

[71] L. Huang, J. Rong, L. Yao, W. Qi, D. Wu, Xu J., and H. Jiang. Quantitative thermoacoustic tomography for ex vivo imaging conductivity of breast tissue. *Chinese Phys. Lett.*, 30(12):124301, 2013.

[72] L. Huang, L. Yao, L. Liu, J. Rong, and H. Jiang. Quantitative thermoacoustic tomography: Recovery of conductivity maps of heterogeneous media. *Appl. Phys. Lett.*, 101:244106, 2012.

[73] M. Jiang, P. Maass, and T. Page. Regularization properties of the Mumford–Shah functional for imaging applications. *Inverse Probl.*, 30(3):035007, 2014.

[74] W. Joines, Y. Zhang, C. Li, and Jirtle R. The measured electrical properties of normal and malignant human tissues from 50 to 900 MHz. *Med. Phys.*, 21:547–550, 1994.

[75] S. I. Kabanikhin. *Inverse and Ill-Posed Problems. Theory and Applications.* De Gruyter, Berlin, New York, 2012.

[76] B. Kaltenbacher, A. Neubauer, and O. Scherzer. *Iterative regularization methods for nonlinear ill-posed problems*, volume 6 of *Radon Series on Computational and Applied Mathematics*. Walter de Gruyter GmbH & Co. KG, Berlin, 2008.

[77] B. Kaltenbacher, F. Schöpfer, and T. Schuster. Iterative methods for nonlinear ill-posed problems in banach spaces: convergence and applications to parameter identification problems. *Inverse Probl.*, 25(6):065003 (19pp), 2009.

[78] A. Keshtkar, A. Keshtkar, and R. H. Smallwood. Electrical impedance spectroscopy and the diagnosis of bladder pathology. *Physiol. Meas.*, 27:585–596, 2006.

[79] S. Kim, O. Kwon, J. K. Seo, and J.-R. Yoon. On a nonlinear partial differential equation arising in magnetic resonance electrical impedance tomography. *SIAM J. Math. Anal.*, 34(3):511–526, 2002.

[80] E. Klann. A Mumford–Shah-like method for limited data tomography with an application to electron tomography. *SIAM J. Imaging Sciences*, 4(4):1029–1048, 2011.

[81] V. Kolehmainen, M. Vauhkonen, and Kaipio J. P. Recovery of piecewise constant coefficients in optical diffusion tomography. *Opt. Express*, 7(13):468–480, 2000.

[82] T. Kreutzmann and A. Rieder. Geometric reconstruction in bioluminescence tomography. *Inverse Probl. Imaging*, 8(1):173–197, 2014.

[83] P. Kuchment and L. Kunyansky. Mathematics of thermoacoustic tomography. *European J. Appl. Math.*, 19:191–224, 2008.

[84] P. Kuchment and L. Kunyansky. Synthetic focusing in ultrasound modulated tomography. *Inverse Probl. Imaging*, 4(4):665–673, 2010.

[85] P. Kuchment and L. Kunyansky. 2D and 3D reconstructions in acousto-electric tomography. *Inverse Probl.*, 27(5):055013, 2011.

[86] P. Kuchment and D. Steinhauer. Stabilizing inverse problems by internal data. *Inverse Probl.*, 28(8):084007, 2012.

[87] L. A. Kunyansky. Explicit inversion formulae for the spherical mean Radon transform. *Inverse Probl.*, 23(1):373–383, 2007.

[88] J. Laufer, B. Cox, E. Zhang, and P. Beard. Quantitative determination of chromophore concentrations from 2d photoacoustic images using a nonlinear model-based inversion scheme. *App. Opt.*, 49(8):1219–1233, 2010.

[89] C. Li, M. Pramanik, G. Ku, and L. V. Wang. Image distortion in thermoacoustic tomography caused by microwave diffraction. *Phys. Rev. E*, 77(3):031923, 2008.

[90] Y.Y. Li and L. Nirenberg. Estimates for elliptic systems from composite material. *Comm. Pure Appl. Math.*, 56(7):892–925, 2003.

[91] T. Lindeberg. Edge detection and ridge detection with automatic scale selection. *Int. J. Comput. Vision*, 30(1):117–154, 1998.

[92] A. Mamonov and K. Ren. Quantitative photoacoustic imaging in radiative transport regime. *Commun. Math. Sci.*, 12(2):201–234, 2014.

[93] D. Mumford and J. Shah. Optimal approximations by piecewise smooth functions and associated variational problems. *Comm. Pure Appl. Math.*, 42(5):577–685, 1989.

[94] W. Naetar and O. Scherzer. Quantitative photoacoustic tomography with piecewise constant material parameters. *SIAM J. Imaging Sciences*, 7(3):1755–1774, 2014. Funded by the Austrian Science Fund (FWF) within the FSP S105 - "Photoacoustic Imaging". Funded by the University of Vienna within the Vienna Graduate School in Computational Science IK I059-N.

[95] O. Ogunlade, B. Cox, and P. Beard. Quantitative thermoacoustic image reconstruction of conductivity profiles. *Proc. SPIE*, 8223:82230R, 2012.

[96] S. Osher and J. A. Sethian. Fronts propagating with curvature-dependent speed: Algorithms based on Hamilton-Jacobi formulations. *J. Comput. Phys.*, 79(1):12–49, 1988.

[97] P.-O. Persson and G. Strang. A simple mesh generator in MATLAB. *SIAM Rev.*, 46(2):329–345, 2004.

[98] A. Pulkkinen, B. Cox, S. Arridge, J.P. Kaipio, and T. Tarvainen. Quantitative photoacoustic tomography using illuminations from a single direction. *J. Biomed. Opt.*, 20(3):036015, 2015.

[99] R. Ramlau and W. Ring. A Mumford–Shah level-set approach for the inversion and segmentation of x-ray tomography data. *J. Comput. Phys.*, 221:539–57, 2007.

[100] R. Ramlau and W. Ring. Regularization of ill-posed Mumford–Shah models with perimeter penalization. *Inverse Probl.*, 26:115001, 2010.

[101] K. Ren, Gao H., and H. Zhao. A hybrid reconstruction method for quantitative pat. *SIAM J. Imaging Sciences*, 6(1):32–55, 2013.

[102] J. Ripoll and M. Nieto-Vesperinas. Index mismatch for diffuse photon density waves at both flat and rough diffuse-diffuse interfaces. *J. Opt. Soc. Amer. A*, 16(8):1947–1957, 1999.

[103] L. Rondi and F. Santosa. Enhanced electrical impedance tomography via the Mumford–Shah functional. *ESAIM Control Optim. Calc. Var.*, 6:517–538, 2001.

[104] T. Saratoon, T. Tarvainen, B. T. Cox, and S. R. Arridge. A gradient-based method for quantitative photoacoustic tomography using the radiative transfer equation. *Inverse Probl.*, 29(7):075006, 2013.

[105] O. Scherzer, M. Grasmair, H. Grossauer, M. Haltmeier, and F. Lenzen. *Variational methods in imaging*, volume 167 of *Applied Mathematical Sciences*. Springer, New York, 2009.

[106] P. Shao, B. Cox, and R.J. Zemp. Estimating optical absorption, scattering, and Grueneisen distributions with multiple-illumination photoacoustic tomography. *App. Opt.*, 50(19):3145–3154, 2011.

[107] V. A. Solonnikov. Overdetermined elliptic boundary-value problems. *J. Sov. Math.*, 1(4):477–512, 1973.

[108] N. K. Soni, K. D. Paulsen, H. Dehghani, and A. Hartov. Finite element implementation of Maxwell's equations for image reconstruction in electrical impedance tomography. *IEEE Trans. Med. Imag.*, 25(1):55–61, 2006.

[109] Y. Sun, E. Sobel, and H. Jiang. Quantitative three-dimensional photoacoustic tomography of the finger joints: an in vivo study. *J. Biomed. Opt.*, 14(6):064002, 2009.

[110] Y. Sun, E. Sobel, and H. Jiang. Noninvasive imaging of hemoglobin concentration and oxygen saturation for detection of osteoarthritis in the finger joints using multispectral three-dimensional quantitative photoacoustic tomography. *J. Opt.*, 15(5):055302, 2013.

[111] A. J. Surowiec, S. S. Stuchly, J. R. Barr, and A. Swarup. Dielectric properties of breast carcinoma and the surrounding tissues. *IEEE Trans. Biomed. Eng.*, 35:257–263, 1988.

[112] X. Tai and X.F. Chan. A survey on multiple level set methods with applications for identifying piecewise constant functions. *International Journal of Numerical Analysis and Modeling*, 1(1):25–47, 2004.

[113] X. Tai and H. Li. A piecewise constant level set method for elliptic inverse problems. *Appl. Num. Math.*, 57:686–696, 2006.

[114] A. Tamasan and A. Timonov. Coupled physics electrical conductivity imaging. *Eurasian J. Math. Comp. Appl.*, 2(2):5–29, 2014.

[115] T. Tarvainen, B. T. Cox, J. P. Kaipio, and S. R. Arridge. Reconstructing absorption and scattering distributions in quantitative photoacoustic tomography. *Inverse Probl.*, 28(8):084009, 2012.

[116] L. V. Wang, editor. *Photoacoustic Imaging and Spectroscopy.* Optical Science and Engineering. CRC Press, Boca Raton, 2009.

[117] L. V. Wang and H. Wu, editors. *Biomedical Optics: Principles and Imaging.* Wiley-Interscience, New York, 2007.

[118] J. Weidmann. *Linear Operators in Hilbert Spaces*, volume 68 of *Graduate Texts in Mathematics.* Springer, New York, 1980.

[119] A. J. Welch and M. J. C. Van Gemert. *Optical-Thermal Response of Laser-Irradiated Tissue.* Springer, Dordrecht-Heidelberg-London-New York, 2 edition, 2011.

[120] T. Widlak and O. Scherzer. Hybrid tomography for conductivity imaging. *Inverse Probl.*, 28(8):084008, 2012. Funded by the Austrian Science Fund (FWF) within the FSP S105 - "Photoacoustic Imaging".

[121] M. Xu and L. V. Wang. Universal back-projection algorithm for photoacoustic computed tomography. *Phys. Rev. E*, 71(1), 2005.

[122] L. Yao, G. Gaofeng, and H. Jiang. Quantitative microwave-induced thermoacoustic tomography. *Med. Phys.*, 37(7):3752, 2010.

[123] L. Yao, Y. Sun, and H. Jiang. Quantitative photoacoustic tomography based on the radiative transfer equation. *Opt. Letters*, 34(12):1765–1767, 2009.

[124] Z. Yuan and H. Jiang. Quantitative photoacoustic tomography: Recovery of optical absorption coefficient maps of heterogeneous media. *Appl. Phys. Lett.*, 88(23):231101, 2006.

[125] Z. Yuan, Q. Zhang, and H. Jiang. Simultaneous reconstruction of acoustic and optical properties of heterogeneous media by quantitative photoacoustic tomography. *Opt. Express*, 14:6749–6754, 2006.

[126] A. Zacharopoulos, M. Schweiger, V. Kolehmainen, and S. Arridge. 3d shape based reconstruction of experimental data in diffuse optical tomography. *Opt. Express*, 21(17):18940–18956, 2009.

[127] R. J. Zemp. Quantitative photoacoustic tomography with multiple optical sources. *App. Opt.*, 49(18):3566–3572, 2010.

[128] H. Zhang and L. Wang. Acousto-electric tomography. *Proc. SPIE*, 5320:145–149, 2004.

A. Deutsche Zusammenfassung

Hybride bildgebende Verfahren kombinieren verschiedene physikalische Modalitäten (wie z.B. elektromagnetische Wellen, Ultraschall oder elektrischen Strom) zur Produktion tomographischer Daten.

Quantitative hybride Verfahren verwenden derartige bildgebende Systeme um ortsabhängige physikalische Eigenschaften der Probe (wie *elektrische Leitfähigkeit*, *optische Absorptions-* oder *Streukoeffizienten*) zu berechnen. Diese liefern medizinisch relevante Information. Normalerweise muss dafür ein zweiteiliges Problem gelöst werden. Im ersten Schritt werden interne Daten (wie z.B. *Stromdichte*, *Leistungsdichte* oder *Initialdruck*) aus Messdaten berechnet. Daran anschließend können die Materialeigenschaften aus den internen Daten berechnet werden.

Dies ist eine kumulative Dissertation, welche drei Forschungsartikel zu unterschiedlichen Problemen im Themenbereich der quantitativen hybriden Verfahren enthält.

In den ersten beiden Artikeln wird das Rekonstruktionsproblem in *quantitativer photoakustischer Tomographie* behandelt. Dies ist ein bildgebendes Verfahren, welches durch Laserpulse erzeugte Ultraschallwellen misst und daraus optische Materialeigenschaften der Probe berechnet. Im ersten Artikel wird eine Einschränkung auf stückweise konstante Materialparameter vorgeschlagen. Dadurch wird es möglich, ein sonst schlecht gestelltes Problem, die Bestimmung von Absorptions-, Streu- und Grüneisenkoeffizienten der Probe aus mehreren photoakustischen Messdaten (mit unterschiedlichen Anregungsrichtungen), zu lösen. Die Rekonstruktion basiert auf einem analytischen Verfahren, welches numerisch an simulierten Daten getestet wird. Im zweiten Artikel wird, abermals unter der Annahme, dass die Koeffizienten stückweise konstant sind, gezeigt, dass wenn der Grüneisenkoeffizient der Probe bekannt ist, ihre Absorptions- und Streukoeffizienten durch eine *einzige* photoakustischen Messung bestimmt werden können. Weiters wird eine variationelle Rekonstruktionsmethode welche auf der *Ambrosio-Tortorelli-Approximation* eines *Mumford-Shah-artigen* Funktionals basiert vorgestellt.

Der dritte Artikel behandelt ein weiteres Problem aus dem Bereich der quantitativen hybriden Verfahren, die Bestimmung der *elektrischen Leitfähigkeit* aus Messungen der *Leistungsdichte*. Dieses Problem tritt bei *Akusto-Elektrischer* Tomographie und *Impedanz-Akustischer* Tomographie auf. Wir schlagen einen iterativen Regularisierungsansatz vor, untersuchen die Konvergenz und testen an simulierten Daten.

B. Curriculum vitae

Wolf Naetar

wolf.naetar@gmail.com
Albertgasse 50/14
1080 Wien

Personal Data

Date of Birth:	27/4/1982
Place of Birth:	Vienna, Austria
Nationality:	Austrian
Marital status:	Unmarried

Education

Since 2010:	PhD study of Mathematics at the University of Vienna
2001 - 2010:	Study of Mathematics at the University of Vienna
1996 - 2001:	HTL Spengergasse (EDV und Organisation), Vienna
1992 - 1996:	Bundesrealgymnasium Laaerbergstraße, Vienna

Career history

Since 10/2010:	Computational Science Center, University of Vienna (theoretical and numerical work on inverse problems)
8/2000:	debis Systemhaus (database development in Microsoft Access)
7/1999:	Wiener Wasserwerke (data typist)

Skills

Languages:	German (native), English (fluent), Spanish (basic)
Programming:	MATLAB (considerable experience), Python (small projects), PHP (small projects), C++ (rudimentary), Java (rudimentary)
Other skills:	LaTeX, HTML

Publications

[1] *The Levenberg-Marquardt iteration for numerical inversion of the power density operator*, with G. Bal, O. Scherzer and J. Schotland, in *Journal of Inverse and Ill-posed Problems*, 21(2):265–280 (2013)

[2] *Quantitative photoacoustic tomography with piecewise constant material parameters*, with O. Scherzer, in *SIAM Journal on Imaging Sciences*, 7(3):1755–1774 (2014)

[3] *A variational method for quantitative photoacoustic tomography with piecewise constant coefficients* with E. Beretta, M. Muszkieta and O. Scherzer, *submitted* (2015).

Conference talks

[1] *Quantitative hybrid electrical impedance tomography.*
GAMM 83rd Annual Scientific Conference.
Darmstadt, Germany, March 2012.

[2] *Quantitative hybrid electrical impedance tomography.*
Inverse Problems: Modeling and Simulation.
Antalya, Turkey, May 2012.

[3] *Quantitative photoacoustic imaging.*
Joint Mathematical Conference of the CSASC Mathematical Societies.
Koper, Slovenia, June 2013.

[4] *Quantitative photoacoustic tomography with piecewise constant material parameters.*
ESI Workshop on Theoretical and Applied Computational Inverse Problems.
Vienna, Austria, May 2014.

[5] *Quantitative photoacoustic tomography with piecewise constant material parameters.*
International Conference on Inverse Problems in Engineering.
Krakow, Poland, May 2014.